UNIVERSITY OF SOUTHAMPTON

FACULTY OF PHYSICAL AND APPLIED SCIENCES

Physics and Astronomy

Radar and Optical Studies of Small Scale Features in the Aurora: The Association of Optical Signatures with Naturally Enhanced Ion Acoustic Lines (NEIALs)

by

Brendan C. Goodbody

Thesis for the degree of Doctor of Philosophy

March 2014

UNIVERSITY OF SOUTHAMPTON

ABSTRACT

FACULTY OF PHYSICAL AND APPLIED SCIENCES
Physics and Astronomy

Doctor of Philosophy

RADAR AND OPTICAL STUDIES OF SMALL SCALE FEATURES IN THE AURORA: THE ASSOCIATION OF OPTICAL SIGNATURES WITH NATURALLY ENHANCED ION ACOUSTIC LINES (NEIALS)

by Brendan C. Goodbody

Naturally Enhanced Ion Acoustic Lines (NEIALs) are enhancements (often over an order of magnitude in power) observed in ion line spectra in incoherent scatter radar data. To date, there has been no conclusive evidence supporting a single production process which explains all observations of NEIALs. A specially designed interferometric radar system has been used to determine the field line height distribution and field line footpoint of observed NEIALs. This system is the EISCAT Svalbard Radar Aperture Synthesis Imaging experiment, known as EASI. Optical observations were taken with the co-located Auroral Structures and Kinetics facility to compare NEIAL positions to locations of optical phenomena.

Results show that the production theories of 'beam-driven Langmuir waves' and 'solitary kinetic Alfvén waves' (SKAW) outlined in this thesis, consistently describe observed phenomena during two separate intervals. During the first interval on the 24 January 2012, the 'non-resonant' regime of 'beam-driven Langmuir waves' dominated, with the 'resonant' regime occurring infrequently, throughout approximately half of the interval. The remaining enhancements were only possible through SKAW or other wave interactions. Observations from the second interval on the 27 March 2012 agree best with the 'resonant' regime of the Langmuir wave theory. However, a number of time steps may have been enhanced by other production mechanisms, most likely SKAW. Radar-derived parameter analysis of these and four other NEIAL intervals in past data was also undertaken. The results showed the existence of 'weak' NEIALs at times surrounding 'strong' NEIAL enhancements. Other than the two aforementioned theories, the majority of others were eliminated independently for all six time intervals using this method.

Contents

List of Figures

Declaration of Authorship

I, Brendan C. Goodbody , declare that the thesis entitled: Radar and Optical Studies of Small Scale Features in the Aurora: The Association of Optical Signatures with Naturally Enhanced Ion Acoustic Lines (NEIALs), and the work presented in the thesis are both my own, and have been generated by me as the result of my own original research. I confirm that:

- this work was done wholly or mainly while in candidature for a research degree at this University;
- where any part of this thesis has previously been submitted for a degree or any other qualification at this University or any other institution, this has been clearly stated;
- where I have consulted the published work of others, this is always clearly attributed;
- where I have quoted from the work of others, the source is always given. With the exception of such quotations, this thesis is entirely my own work;
- I have acknowledged all main sources of help;
- where the thesis is based on work done by myself jointly with others, I have made clear exactly what was done by others and what I have contributed myself;
- none of this work has been published before submission

Signed:.....

Date:.....

Acknowledgements

There are many people I wish to thank for their help and support throughout my PhD studies. Firstly, I owe the most to my supervisor Betty Lanchester, for her advice, support and direction throughout the project. Her gentle guidance skilfully aided me past the potential pitfalls of the PhD. I also thank her for her patience and diligence with me personally, particularly in the writing of this thesis.

Secondly, I would like to thank Tom Grydeland, who designed and piloted the EASI system on Svalbard. His advice and guidance were invaluable in helping me get to grips with the EASI system, particularly at the start of my PhD.

I also owe much to Bjorn Gustavesson, who helped advise on appropriate aperture synthesis imaging methods and debated on alternative hypotheses, as well as continuously questioning, guiding and pushing me to achieve more, even after moving to employment in a different country.

I wish to thank Sam Tuttle, Daniel Whitter, Vasyl Belyey, Nicola Schlatter, Hanna Dahlgren, Olli Jokiaho, John Spry, Tom Gwyn and Hannah Vickers, for their assistance and advice during campaigns on Svalbard, and in the office. I also thank Tromsø University and KTH in Stockholm, for their continued cooperation in the EASI project.

Lastly, but by no means least, I wish to thank my family, and my loving fiancée Cara, without whose support, understanding and patience, this work would not have been possible.

Acronyms

ACE Advanced Composition Explorer

ASI Aperture Synthesis Imaging

ASK Auroral Structure and Kinetics

BSP Boundary Polar Sheet

CME Coronal Mass Ejection

CPS Cusp Polar Sheet

EASI ESR Aperture Synthesis Imaging

EISCAT European Incoherent SCATter radar network

EM Electro Magnetic

ESR EISCAT Svalbard Radar

FMI Finnish Meteorological Institute

GGS Global Geospace Science (WIND)

GLORIA The GLObal auoRal Imaging Access

GOES Geostationary Operational Environmental Satellite

IMF Interplanetary Magnetic Field

IRI International Reference Ionosphere

IPP Inter Pulse Period

IS Incoherent Scatter

ITSVD Iteratively Truncated SVD

KAW Kinetic Alfvén Wave

LLBL Low-Latitude Boundary Layer

LOS Line of Sight

LPI Lag Profile Inversion

NASA National Aeronautics and Space Administration

NORSTAR NORthern Solar - Terrestrial ARray

MIRACLE Magnetometers - Ionospheric Radars - Allsky Cameras Large Experiment

MSISE Mass-Spectrometer - Incoherent-Scatter Extended

PSF Point Spread Function

SIF Spectrographic Imaging Facility

SKAW Solitary Kinetic Alfvén Wave

SOHO SOlar and Heliospheric Observatory

SuperDARN Super Dual Auroral Radar Network

SWAP Solar Wind and Atmohsperic Package

SVD Singular Value Decomposition

TV Total Variance

Chapter 1

Introduction

The main subject of this work is based on the first observations of Naturally Enhanced Ion Acoustic Lines (NEIALs) with the EISCAT Svalbard Radar Aperture Synthesis Imaging (EASI) facility, alongside co-located optical observations. NEIALs are microwave frequency, radar observed phenomena that occur in the upper atmosphere, and predominantly occur during strong auroral substorm conditions. Often coinciding with red auroral ray structures, they manifest themselves as large increases in radar backscattered power (up to 5 orders of magnitude above normal), over short time scales (less than one second), over large height ranges. They are observed with 'Incoherent Scatter' radar systems at high and low latitude regions, most often when aligned towards the magnetic zenith. A more detailed explanation of historical observations and a list of current production theories for these events can be found in Chapter 3.

This chapter first describes the processes under which auroral activity can develop, and its effects on the Earth's upper atmosphere. The processes behind Incoherent Scatter (IS) radar observations are described as well as the techniques of Aperture Synthesis Imaging (ASI) used with the Eiscat Svalbard Radar in this work.

1.1 Processes Leading to Aurora

1.1.1 The Earth's Magnetosphere and Reconnection

Charged electrons and protons are ejected into the solar wind via a variety of solar activities, for example through Coronal Mass Ejections (CME). These escaped solar particles form what is called the solar wind, and are transmitted in a radial Parker spiral pattern from the Sun. A proportion of this solar wind is directed towards the path of the Earth. In the inter-stellar medium, different regimes of particles (at different velocities and densities) within the solar wind interact, causing shock waves and large density pockets to form.

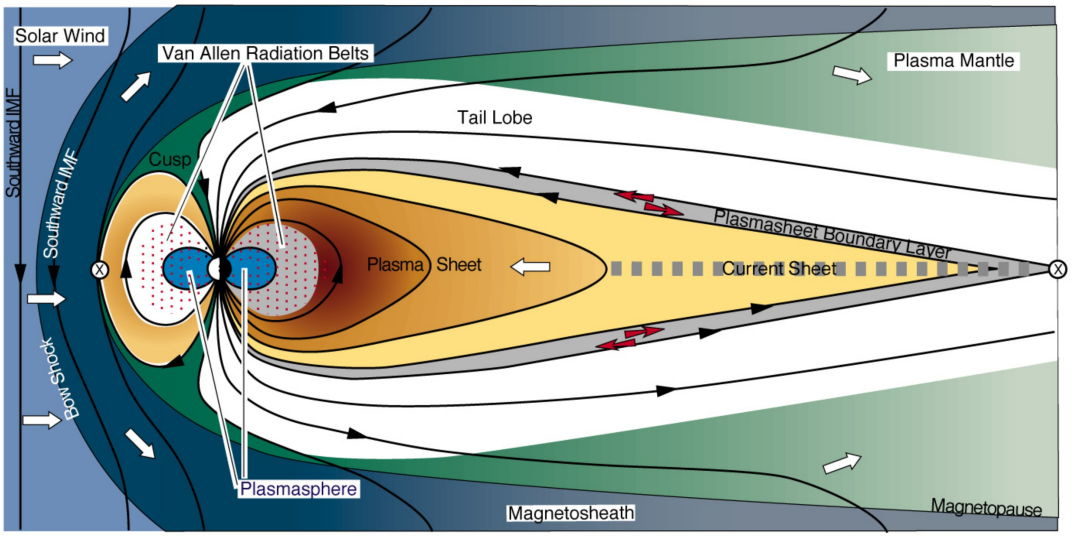

Figure 1.1: Earth's magnetosphere under strong solar wind conditions. *Courtesy of http://space.rice.edu*

The shape of Earth's dipole magnetic field is highly warped by constant collisions from the solar wind, and can vary in shape and size depending upon the conditions of the solar wind. In general, the magnetic field has a shape much like a windsock under strong wind speeds. Under these strong solar wind conditions it extends on average ~ 15 $\mathrm{R_E}$ into the direction of the solar wind (decreasing in size with increased solar wind), and stretches up to 200 $\mathrm{R_E}$ behind the Earth away from the solar wind. Figure 1.1 illustrates this stretched magnetosphere due to the solar wind and labels the different regions within. The space within the Earth's magnetic field barrier (the magnetopause) is known as the magnetosphere. The majority of the solar wind is deflected by the Earth's magnetic field ($> 99\%$) around the Earth, shielding the atmosphere from a large proportion of the solar wind particles. However, under specific conditions, a process known as 'reconnection' can occur and solar wind particles enter the Earth's magnetosphere. Reconnection events also cause numerous wave interactions to occur, many of which have the potential to transport energy along magnetic field lines into the Earth's atmosphere. The z component of the Earth's magnetic field (B_z) is orientated from the south pole towards the north pole. The magnetic field solar wind or interplanetary magnetic field (IMF), however, varies greatly with time. Depending upon its orientation, different types of reconnection can occur. The optical signatures produced in the Earth's upper atmosphere (or ionosphere) by such events contain much information about the nature of these processes.

1.1.1.1 Day-side Reconnection

If the magnetic field of the solar wind is aligned southward (B_z negative), then it can reconnect directly to the sun-facing portion of the Earth's magnetic field. Due to this reconnection, a

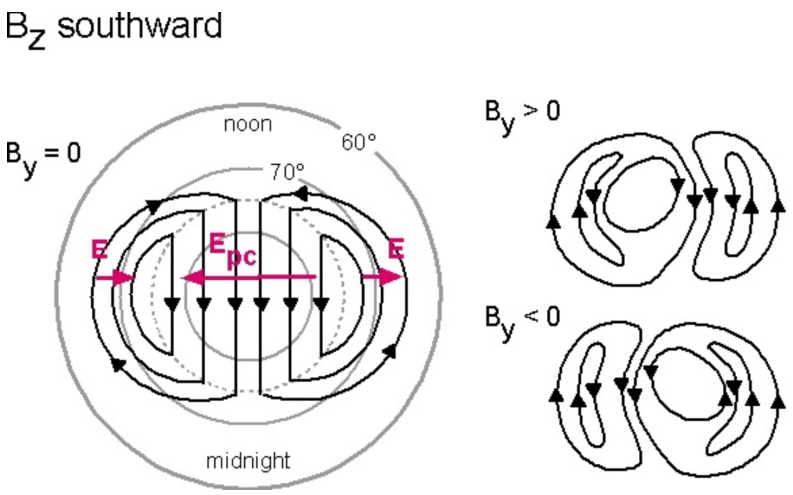

Figure 1.2: Two cell charge particle convection under B_z negative day-side reconnection conditions. Perturbations in other magnetic parameters such as By can alter the shape of this system. *Courtesy of Oulu University*

proportion of the particles from the solar wind can be trapped in the Earth's magnetic field. This process is known as 'day-side' reconnection, as it couples down to the day side of the Earth.

Particles entering magnetic field lines with reconnection events undergo a number of acceleration processes, the exact methods behind and full extent of which are still under debate in the scientific community. Despite the methods being under debate, the acceleration of magnetospheric particles caused by reconnection has been well documented in past literature [Goldstein et al., 1986]. Accelerated charged particles and reconnection produced waves travel along the Earth's magnetic field lines and enter the atmosphere at polar latitudes on the day side of the Earth. The location at which these waves and particles interact with atmospheric particles in the ionosphere depends upon the velocity and density of this precipitation, caused by the reconnection. The auroral emissions produced by excitation of ionospheric particles from charged particle collisions and wave energy transfers depend upon the initial condition of the Earth's atmosphere and the energy and density of the precipitating charged particles and waves.

Newly opened field lines are dragged, via the solar wind pressure, over the Earth's poles towards the magnetotail. These open-ended field lines can subsequently reconnect with other solar wind fields if correctly aligned and contract back towards the Earth, dumping more solar wind particles into the atmosphere, at higher latitudes and at other longitudes than the initial reconnection. Day-side reconnection increases the amount of open flux in the magnetosphere. Charged particles trapped in reconnected, open magnetic field-lines are dragged along with the field lines, across the Earth's poles. Convection patterns of charged atmospheric particles arise, as the ionospheric system attempts to move back into an equilibrium position. Electron precipitation on Svalbard during day-side reconnection is predominately low energy in nature ($<$ 200 eV) with large electric currents observed at times (as first described by Winningham et al. [1975]).

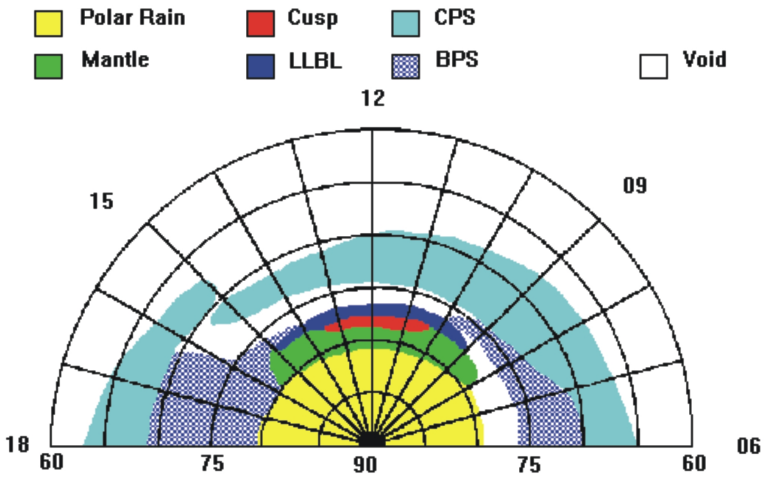

Figure 1.3: Polar cap regions in the northern anti-sunward hemisphere of the earth in coordinates of latitude (x axis) and local time (radial axis). Outlining the region where Polar Rain (yellow), the Mantle (green), Cusp, Lower Latitude Boundary Layer (dark blue), Central Plasma Sheet (light blue), and Boundary Plasma Sheet (patterned blue) occur. *Courtesy of NASA*

1.1.1.2 Night-side Reconnection

Perhaps an even greater consequence of this reconnection occurs in the magnetotail of the magntosphere. As unanchored magnetic field lines are dragged across the poles a concentration of magnetic field lines appears in the magnetotail. This reconnection is known as 'night-side' reconnection, as it couples down to the night-side of the Earth. In night-side reconnection, particles and waves along connected field lines become highly accelerated through a number of processes. This acceleration is much greater than that observed during day-side reconnection. Again, the exact processes behind these accelerations are still under scientific debate, but numerous observations of this acceleration exist in past literature [Axford, 1984]. Night-side reconnections predominantly cause 'substorm' events, which typically last between $\sim$1 and 3 hours, involving rapidly varying high energy or 'hard' precipitating particles, evolving in a systematic way.

During B_z negative reconnection events, a distinct two-cell system of ionospheric plasma regularly develops. Figure 1.2 shows the typical orientation of this system and how it is affected by IMF magnetic field parameters. The two cells are located to the west and east of the Sun facing surface of the Earth. The cells circulate plasma towards the day side of the Earth, to replace charged particle content dragged across the pole, towards the night-side of the Earth. The exact shape of this two-cell structure is dependent upon the parameters of the solar wind magnetic field that is reconnecting. Differences in B_y and B_x components have the largest effect upon the

shape, for example, by enlarging one of the two cells. Alternatively, the orientation of the poleward flow to the night-side can be misaligned, no longer directing particles towards magnetic midnight.

Reconnection in the Earth's magnetotail re-closes field lines opened through reconnection on the day-side. Day-side auroral precipitation usually consists of low energy (<500 eV) or 'soft' electrons. These events usually produce auroral signatures in the 'cusp' and 'plasma mantle', and can indirectly cause emissions from the 'Low-Latitude Boundary Layer' (LLBL) regions of the poles. Figure 1.3 shows the different regions that develop surrounding the poles, during a substorm event. The axes for this figure are latitude and local time.

The optical measurements used in this work are predominantly produced in the cusp and LLBL regions, under reconnection conditions. Due to the soft nature of precipitation, day-side reconnection events often contain strong amounts of the red 732.0 nm oxygen emission observed in this study. Conversely, night-side reconnection events more often contain greater levels of emission from high energy electron precipitation. The 637.0 nm emission from $N_2$1P observed in this study is produced by these higher energies and can be used to estimate the total energy flux. Additionally, other emissions, such as 777.4 nm emission also used in this study, are sensitive to a broad range of energies, and so can be used in estimating the energy of precipitation, combined with modelling. Therefore, the accurate measurement of these and other wavelengths is vital for analysis of reconnection driven events.

1.1.2 Auroral Substorms

As with all high energy precipitation events, substorm events cause bright optical auroral signatures which have been extensively studied from the ground. Svalbard is geographically located within the quiet auroral oval and so is therefore in a good position to observe the evolution of auroral substorms. Past substorm optical observations have shown that they undergo three main phases, named the 'growth', 'expansion' and 'recovery' phases, most recently summarised by Akasofu [2013].

The magnetosphere accumulates energy released during the 'growth' phase. However, the auroral changes that occur during the growth phase and its duration have not yet been well established, and are a cause of discussion in current literature [Akasofu, 2013]. What is known is that the equatorward half of the auroral oval appears to contract just prior to substorm onset [Akasofu et al., 2010]. It is theorized that this phenomenon may be related to the thinning at the near-Earth end of the current sheet that separates the northern and southern 'tail lobes' of the magnetopshere [Kan et al., 1998]. However, the current in the current sheet must be increased during the growth phase regardless of this effect, so that magnetic energy seen in the expansion phase can be accumulated. This feature is often expressed by stating that the dipole field lines in the night-side are 'stretched' during the growth phase.

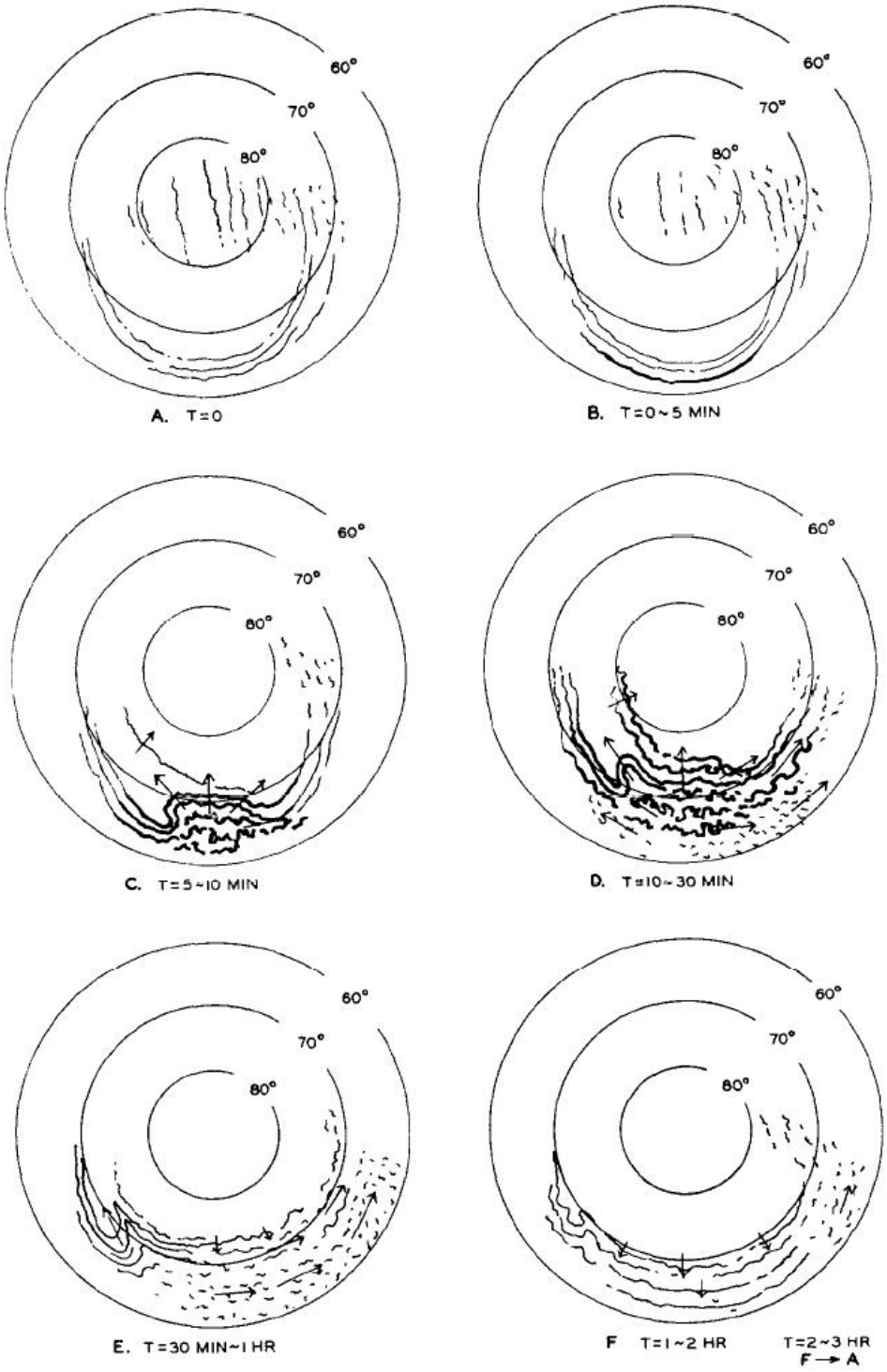

Figure 1.4: Polar substorm development with time. Shows the transition from undisturbed conditions (A) through the substorm onset (B-D), and into the recovery stage (E-F). *Courtesy of Berkeley University*

As first described by Akasofu [1964], the 'expansion' phase is rapid, usually lasting between 10 and 30 minutes. Figure 1.4 shows an example of the extent of auroral activity surrounding the poles throughout a typical substorm event. In undisturbed conditions a weak auroral uniform oval is expected at higher latitudes towards the day-side, descending to lower latitudes on the night-side (Figure 1.4 A). The onset of the storm usually manifests itself by a sudden brightening of auroral arcs close to the midnight meridian. These brightened arcs then move polewards, accompanied by highly-defined ray structures. Due to the poleward motion, a 'bulge' in the auroral oval starts to appear in the midnight sector (Figure 1.4 C). This bulge expands in a poleward direction. In the evening direction, following the bulge, folds begin to form. These folds move rapidly westward due to the bulge's expansion in what are known as 'westward travelling surges'. These surges can disrupt or break up the arcs as they pass, particularly in the midnight sector, depending on the strength of the substorm (Figure 1.4 D).

The 'recovery' phase usually starts with the expanded auroral oval remaining in its enlarged size for between 10 and 30 minutes. It then slowly recedes back to the unexcited auroral oval shape, with the bulge reducing in size (Figure 1.4 E), and the optical arcs moving slowly equatorward. This reduction is usually much slower than the speed of expansion. The speed of the westward surge also reduces at this time. This surge may degrade into multiple smaller irregular folds or become well defined loops. The brightness of arcs in the evening sector reduces, with folds and ray structures starting to disappear at this time. In the morning sector most of the arcs and band structures disappear, and the remaining structures drift towards the north.

1.2 Upper Atmosphere

This section summarizes the composition of the upper atmosphere and the most important thermal and chemical reactions that occur within it. The upper atmosphere describes the Earth's atmosphere above 60 km, extending up to 1000 km, depending upon the magnetospheric and solar wind conditions. The ionosphere is the charged population of the atmosphere. At different regions in altitude different species and reactions dominate, and the thermal processes that govern them change. The upper atmosphere has three main regions, the D, E and F regions; the latter two regions are of most importance in the present work.

The E region of the atmosphere ranges between $\sim$95 and 160 km. The E region is extensively used for communications as it is a strong reflector of radio signals between 2 and 50 MHz. This is due to its high proportion of ions, the densities of which are highly dependent upon the level of solar excitation. One of the main sources of ionization is EUV radiation of 80.0 - 102.7 nm, which is absorbed by oxygen molecules (O_2) to form molecular oxygen ions (O_2^+). X-ray radiation of 1.0 - 10.0 nm is also absorbed in this region, which ionizes all atmospheric constitutes. This emission is also highly dependent on solar activity. The state of the region differs greatly between day and night conditions. Reactions such as radiative recombination

and dissociative recombination can reduce the ion populations and dominate reactions in the E region. The main recombination reactions that occur in the E region are:

$$e + O_2^+ \rightarrow O + O \tag{1.1}$$
$$e + N_2^+ \rightarrow N + N \tag{1.2}$$
$$e + NO^+ \rightarrow N + O \tag{1.3}$$

The F region is the top-most region in the ionosphere, stretching from above the E region out to the magnetosphere. When viewed by radar, the region is seen to contain two distinctive layers, known as the F1 and F2 layers. The F1 layer typically ranges from about 150 to 200 km with a peak of between 160 and 180 km. The primary ion population in the F1 region is O^+, and this is where the majority of atmospheric O^+ ions are produced. This region has an average free electron density of $\sim 5 \times 10^{-1}$ e/cm^3, which can vary by an order of magnitude between noon and midnight conditions. The oxygen ionisation occurs in the F1 region due to heavy absorption of 20.0 - 90.0 nm solar radiation; this ion charge subsequently exchanges with the following ions: O_2^+, N_2^+, O^+, He^+, and N^+. The O^+ population in this region can charge exchange in the following reactions:

$$O^+ + O_2 \rightarrow O_2^+ + O \tag{1.4}$$
$$\text{or} \qquad O^+ + N_2 \rightarrow NO^+ + N \tag{1.5}$$

$$e + O^+ + O_2 \rightarrow O + O + O \tag{1.6}$$
$$\text{or} \qquad e + O^+ + N_2 \rightarrow O + N + N \tag{1.7}$$

thus leaving NO^+ and O_2^+ the most abundant ions with little radiation in this region.

The F2 layer extends from beyond 200 km to about 800 km with a density peak at 300 - 400 km. The F2 layer differs from the regions below it, in that the loss rates for ionisation become sufficiently low that transportation becomes important, enabling the region it to remain after sunset. Although it is technically an upwards extension of the F1 region, as most of the region's ions are produced in the F1 region and are transported vertically to the F2 region, it is deemed as separate due to its unique features. The major ion species of the region is O^+ and the reaction that dominates this ion in the F2 region is the loss through recombination, which takes place in two stages:

$$O^+ + N_2 \rightarrow NO^+ + N \tag{1.8}$$

$$NO^+ + e \rightarrow N + O \tag{1.9}$$

During night time, due to the absence of solar heating, the F2 region cools and shrinks, merging with the F1 layer below.

1.3 Monitoring and Observing the Aurora

Auroral substorm activity has been actively monitored since the beginning of the 20th century, starting with the use of magnetometers. Since these early days, our understanding has greatly expanded, incorporating multiple methods of detection and observation. Magnetometers were followed by the first radar observations of the ionosphere by Gordon [1958]. This method quickly expanded to include Incoherent Scatter (IS) methods which could derive ionospheric parameters (electron and ion temperatures, densities and velocities) from the shape of the received signal (see Section 1.4). These new radar results were soon followed by the first full scale optical study of the aurora using multiple all sky imagers, which was conducted by Akasofu [1964]. It is only since radar observations have been used in conjunction with optical data that the full scope of ionospheric interactions has been realized. These range from magnetospheric altitudes of above 2000 km down to the stratospheric altitudes of $\sim$90 km, and are likely to couple to processes even further down into the atmosphere. The scale and variety of interactions requires that multiple instruments are used for a full analysis of any auroral event.

1.3.1 Radar Measurements

Auroral radar measurements are made by transmitting and receiving reflected electromagnetic radiation from precipitating electrons and excited ions in the atmosphere (see Section 1.4). Results come typically from a range between 90 and 2000 km in altitude, depending on the wavelength and transmission technique used.

Historically, ionospheric 'Incoherent Scatter' (IS) radar measurements have been made using large steerable parabolic dishes. These have a number of advantages as well as drawbacks. These systems have large gain and so can produce accurate measurements for multiple ranges at short time integrations. However, only a single measurement is produced at each range over the area coverage of the radar beam. Additionally, to move the position of this radar beam takes time due to the mechanics of rotating a large dish. The main advantage that all radar measurements have over optical measurements is their high altitude resolution, and the large ranges possible. New radar technologies have solved a number of these limitations by using phased arrays instead

of parabolic dishes. Although each element in a phased array has much lower gain than a single dish, many thousands of elements can be combined to produce a comparably high gain signal. Phase offsets can be applied between elements, so that the radar beam is 'steered' almost instantaneously. Additionally, the elements can be combined into smaller groups so that simultaneous observations can be made in multiple directions, albeit with lower gain power. This allows for the possibility of forming three dimensional radar images, and accurately positioning reflective objects within the radar beam. The methods used to form three dimensional radar images are described in Section 1.5.

'Coherent' radars are used in auroral studies by reflecting signals from atmospheric charged particle density irregularities in the ionosphere. These irregularities are invariably observed to occur along magnetic field lines. The large ion density increases caused by auroral reconnection events and the subsequent convection of these ion densities is particularly visible using this method. Each radar gives the reflection position and the density irregularity line of sight velocity data, in a single point direction. The SuperDARN network, which is used in this work, uses multiple stations around the world. Each station includes multiple radars, each with a FOV within a small angle of each other, usually transmitting on two different frequencies. The data from the different antennas are combined to give readings over a large spatial area. The stations are positioned such that their FOV overlap and cover the majority northern, and a large proportion of the southern hemisphere. From this coverage, a model of how the plasma in the ionosphere is moving on a global scale can be made. Such global convection maps have been used in this work to give background flows. A large limitation of these radars is that, although range can be estimated from the time of signal transmission to reception, the altitude at which the reflection occurred cannot be extracted.

1.3.2 Optical Measurements

Emissions from electron collisions in the upper atmosphere span the entire optical wavelength range. Different wavelength emissions arise from collisions of electrons with varying energy with different atmospheric species and particles. As the composition of the atmosphere varies greatly with altitude, the wavelength emissions produced also vary in a similar way. The altitudes from which optical emissions are produced depends upon the energy of electrons. Low energy emissions typically come from $\sim$400 km, whereas high energy emissions typically come from 120 km (see Section 1.2). These emissions can be viewed over a large spatial area using an all-sky camera system, or if greater detail is needed, using high definition telescoped camera systems. A significant limitation of optical imaging is that it is impossible to measure the altitude of emission for a given observation from a single camera. If emissions that require low energies and high energies are viewed independently, an understanding of the electron energy spectrum and flux of these energies can be made using the nature of the emissions, as first suggested be Rees [1963] and discussed in detail by Lanchester and Gustavsson [2012]. This method is

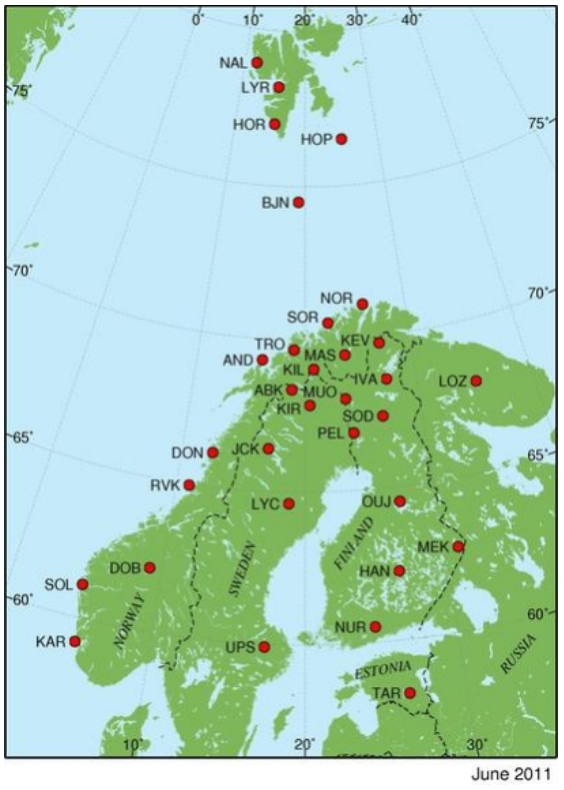

Figure 1.5: Map of magnetometer station positions in the Scandinavian Arctic. *Courtesy of FMI*

complicated by the wide variety of atmospheric species and produced emissions, which often overlap similar wavelengths, making it difficult to isolate emissions from a single species.

1.3.3 Magnetometers

The first detailed and large scale monitoring of the magnetosphere and auroral oval came through magnetometers, which were devised by Gauss in 1832, but not used to monitor magnetospheric activity until Julius Bartels developed the geomagnetic K_p index in 1938 [Bartels and Fanselau, 1938]. The K_p index is a measurement of horizontal magnetic disturbance within the auroral oval with a range between 0 and 9, where 5 or greater indicates a geomagnetic storm.

Since their inception, the number and function of magnetometer stations has been greatly expanded to include vector magnetometers, so that changes in activity can be monitored in three dimensions, and polar magnetic vector data can be recorded. Figure 1.5 shows the current extent of magnetometer coverage over Scandinavia. To give an understanding of what is happening to the magnetosphere over an auroral event, the data from multiple sites throughout the event needs to be examined. Even with data from multiple locations, the results can provide only limited understanding. However, due to their low maintenance costs and high reliability, magnetometer

data and the K_p index as well as many other magnetic indices are still used to this day as a measurement of geomagnetic activity.

1.4 Incoherent Scatter Radar Theory

Radar scattering from electrons in metallic materials was first discovered by Heinrich Hertz in the late 19th century. In 1958 it was realized that a similar technique could be used to probe free electrons in the upper atmosphere [Gordon, 1958], and the first Incoherent Scatter (IS) radar observatory was completed in Arecibo in 1962. The radar dish measures 300 m in diameter and is capable of directly probing electron oscillation in the ionosphere, something even today few IS radars are capable of. Although it was later proved to be much larger than needed for IS purposes, it still remains the largest and one of the most powerful IS and radio telescopes in the world.

1.4.1 Incoherent Scatter

As opposed to conventional radar, which scatters electromagnetic (EM) waves from coherent structures, say a satellite or a plane (with spatial volumes many times smaller than the radar beam, and dense electron concentration), incoherent scatter deals with weak signal scattering from beam-filling structures. The original premise of IS was to scatter electromagnetic waves off free electrons in the ionosphere through a process called Thomson scattering [Thomson, 1906]. In this process the electric field of the incident EM wave puts electrons it encounters in an oscillatory motion. A small fraction of this incident energy is then emitted as dipole radiation, which can then be detected by a receiving antenna. A similar process can occur with ions as well. However, due to their much larger mass, the energy scattered is negligible in comparison, and at very different frequencies. This process of IS, described by Farley [1966], is widely used as most ionospheric features consist of large scale low density charged plasmas.

1.4.1.1 Thompson Scattering

How much an EM wave is Thomson scattered by the plasma depends on the refractive index (ε) and density of the plasma. The refractive index of an electromagnetic wave in a plasma can be given by the equation:

$$n = \sqrt{1 - \frac{n_e e^2}{\varepsilon m_e \omega_0^2}} \tag{1.10}$$

where n_e is the electron density, e the electron energy, ε_0 the permittivity of free space, m_e the mass of an electron and ω_0 the critical frequency of the plasma.

In comparison to coherent structures, IS structures are usually extremely transparent (weak scatterers), with over 99% of the EM waves passing through the medium. The exact amount passing through the observed volume depends upon the permittivity of the plasma making up the ionosphere at the time of experiment. The permittivity of a plasma is given by:

$$\varepsilon = \varepsilon_0 n^2 = \varepsilon_0 - \frac{n_e e^2}{m_e \omega_0^2} \tag{1.11}$$

Therefore, the permittivity changes with electron density perturbations within the plasma so that:

$$\Delta\varepsilon = -\frac{e^2}{m_e \omega_0^2} \cdot \Delta n_e \tag{1.12}$$

This describes how small density and charge irregularities can largely affect the permittivity and reflective power of a plasma and therefore the behaviour of the large scale ionosphere.

1.4.1.2 Electron Motion

Electrons in a plasma are non stationary, and exhibit both bulk and thermal motions. Just as with sound waves, an electromagnetic wave scattered by an object (electron) moving with a velocity in the direction of the origin of the wave will be scattered with a Doppler shift, dependent on the velocity of the electron. The frequency of a reflected EM wave will be at a different frequency to the incident EM wave due to the Doppler shift [Doppler, 1906], if the scattering electron is moving. The frequency of this scattered wave can be calculated by:

$$\nu' = \nu_0 \sqrt{\frac{c+v}{c-v}} \tag{1.13}$$

where the Doppler shift is:

$$\delta\nu = \nu - \nu_0 = 2\nu\frac{v}{c} = 2\frac{v}{\lambda_0} \tag{1.14}$$

where λ_0 is the wavelength of the original EM wave.

Depending on the direction and velocity the electron travels relative to the radar, the shift can be positive (up-shifted) or negative (down-shifted).

1.4.1.3 Bulk Plasma Calculations

Radar transmitted EM waves travel in a narrow band and illuminate scattering volumes of plasma in the ionosphere as they propagate through. A scattering volume of plasma contains a large number of moving electrons. In the absence of a plasma bulk motion (i.e. if the plasma is stationary), the density of electrons with velocity along the radar beam v_x follows a Maxwellian velocity distribution:

$$\frac{dn_e}{dv_x} \propto e^{-v_x^2/v_m^2} \tag{1.15}$$

where $v_m = \sqrt{2k\mathrm{T}_e/m_e}$ is the most probable speed and T_e is the electron temperature.

Each electron will emit scattered radiation at a frequency determined by its velocity along the radar beam direction, and therefore, the spectrum of the radiation will be non monochromatic (i.e. will come at multiple frequencies). The spectrum will be centred on the radar transmission frequency and should exhibit a Maxwellian shape similar to the velocity distribution. The velocity corresponding to the half-width of the spectrum is obtained by:

$$\Delta v = 2. \cdot 2\frac{v_x}{\lambda_0} = 4\frac{v_x}{\lambda_0} = \frac{4}{\lambda_0}\sqrt{ln2} \cdot \sqrt{2} \cdot \sqrt{\frac{k\mathrm{T}_e}{m_e}} \sim \frac{4}{\lambda_0}\sqrt{\frac{k\mathrm{T}_e}{m_e}} \tag{1.16}$$

1.4.2 Ion Acoustic Measurements

The spectrum of IS should have a Gaussian shape with a spectral line width of the order of 1 MHz. It was to determine these spectra that the Arecibo antenna was made to be 300 m. However, after first observations were made, the width of the dominant scattered signal proved much smaller than expected. In fact the spectrum was more in accordance with the motions of ions than of electrons. The explanation for this was soon discovered.

In the electron component of a plasma, the fluctuations with wave lengths longer than the Debye length of the plasma are mainly controlled by the motion of the ions. This is due to the electrons following the ions in order to preserve charge neutrality. Therefore, although the microscopic scattering mechanism is Thomson scattering by electrons, the shape of the IS spectrum at wavelengths longer than the Debye length will be determined by the ion motion. Therefore, all modern IS radars are of the order of 32 m in diameter as this size can accurately sample these frequencies. The Debye length of an ion surrounded by electrons can be calculated by:

$$\lambda_D = \sqrt{\frac{\varepsilon_0 k\mathrm{T}_e}{n_e e^2}} \tag{1.17}$$

where T_e is the electron temperature, and n_e the number of electrons.

Due to the limited freedom of the ions in the plasma, when an IS spectrum is viewed there are two main wave modes which contribute to the thermal fluctuation; these are the ion and electron-acoustic waves. The phase velocity of the ion-acoustic wave is given by:

$$\upsilon_+ = \sqrt{\frac{k\mathrm{T}_i}{m_i}\left(1 + \frac{\mathrm{T}_e}{\mathrm{T}_i}\right)} \tag{1.18}$$

where m_i and T_i are the ion mass and temperature.

The dispersion equation for the electron-acoustic wave is given by:

$$\omega_e = \mathrm{f}_p\sqrt{\lambda_e^2 + 12\pi^2\lambda_D^2} \tag{1.19}$$

where ω_e and λ_e are the phase velocity and wavelength and f_p the plasma frequency:

$$\mathrm{f}_p = \frac{1}{2\pi}\sqrt{\frac{n_e e^2}{\varepsilon_0 m_e}} \tag{1.20}$$

The electron-acoustic wave is dispersive because its phase velocity depends on the wavelength of the incident electromagnetic radiation, whereas the ion-acoustic wave is not.

The density fluctuation contains Fourier components propagating in opposite directions, and therefore the scattering spectrum will contain both up-shifted and down-shifted lines. Thus the scattering spectrum should contain four lines (two down-shifted and two up-shifted ion and electron lines). However, in the plasma, new waves are thermally generated on extremely short time scales and are attenuated by Landau damping. The result is that the spectral lines will be broadened by this Landau damping. The broadening of the spectral line is sufficient to make the spectral lines merge into a single line. Therefore, the typical spectrum seen from IS radar in the E and F region is a double humped shape around the central frequency.

1.4.3 Spectral Shape

Other characteristics of the ionospheric plasma can be determined from the shape of this double humped and broadened spectrum, [Nielsen and Schlegel, 1985].

For example, the width of the ion line spectra is roughly twice the Doppler shift of the ion-acoustic waves i.e $4\upsilon/\lambda_0$. If the ion and electron temperatures are approximately equal, then $\nu_+ \sim \sqrt{2k\mathrm{T}_i/m_i}$, and so the width of the ion line will correspond to the thermal speed of the ions as opposed to the electrons. Figure 1.6 shows how the spectral shape changes under different plasma conditions. Other plasma parameters that determine the spectral shape are the ion mass, ion/electron temperatures and ratios, and collision frequencies.

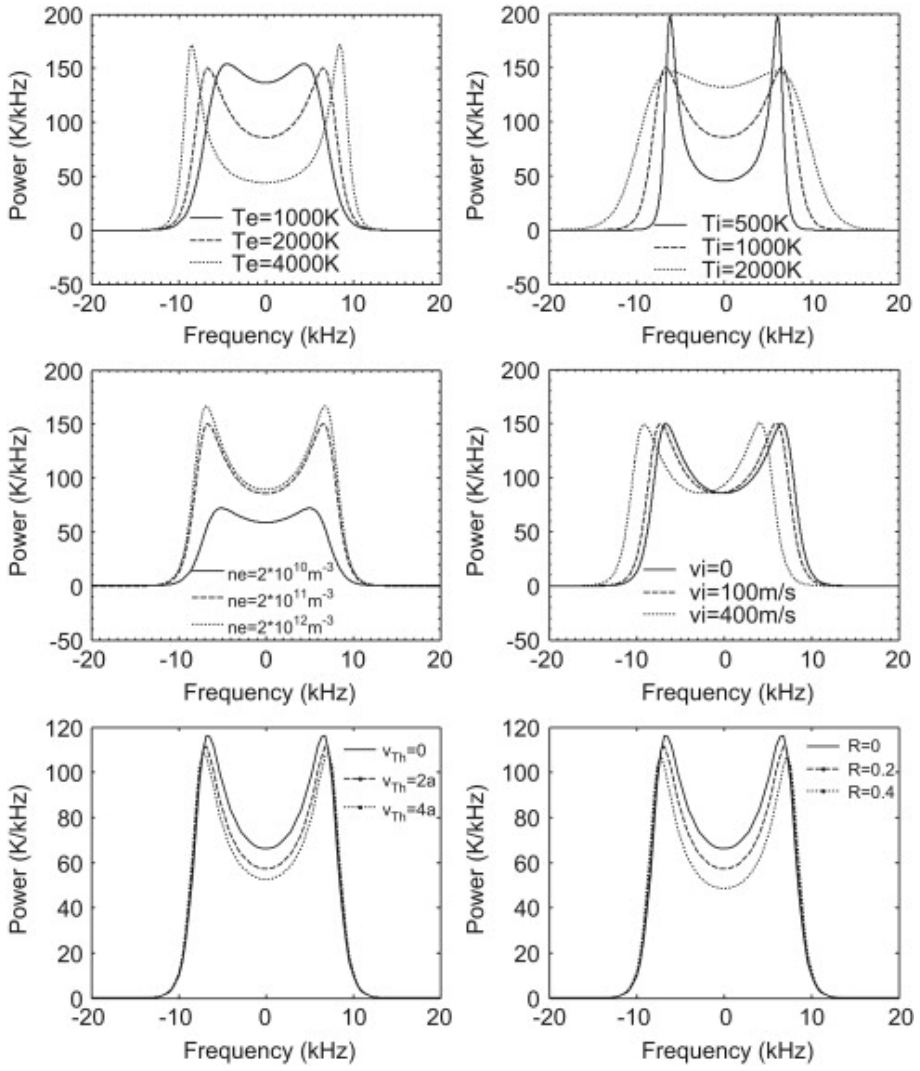

Figure 1.6: Ion line spectral shape under different conditions. *Courtesy of Lehtinen and Asko [1996]*

By using a variety of fitting methods, these primary physical parameters can be determined from the ion line shape. Secondary parameters can then be calculated from these. Secondary parameters include electric field strengths, conductivity, electric current, Joule heating, neutral wind velocities. Electron acoustic plasma lines are not substantially damped and consist of two narrow peaks which can be used to determine the density of electrons from the frequency at which they occur.

1.5 Aperture Synthesis Imaging Theory

Aperture Synthesis Imaging (ASI) is the process of creating 2D or 3D brightness images of emitting or scattering objects. This is done by combining the signal received from multiple

spatially separated radars.

The process of combining one or more pairs of radar data known as interferometry is used for a wide range of purposes. The first use of interferometry with IS was by Woodman [1971], at equatorial latitudes using the Jicamarca array. Most recently, it has been implemented at polar latitudes with the PFISR system [Dahlgren et al., 2012] in Poker Flats, Alaska, and the RISR system [Sparks et al., 2010] in Resolute Bay, Canada. All these systems contain multiple phased array antennas that are arranged to combine signals from each other to create high power results. Additionally, as all the above radar systems use antennas that are identical to each other, a simple expression for coherence can be used to produce interferometric results. However, when the two receiving antennas have different gains or the width of scatter is not negligible compared to the antenna beam width, then a more careful examination and calculation of coherence is needed.

Interferometric radar systems are capable of locating and imaging high power objects within the radar beam. The exact method used for imaging depends upon the limitations of the individual radar systems, and the objects that are being observed. The methods used in this work are described in Section A.1.

1.6 Thesis Summary

The principle subject of this work involves determining the production processes behind Naturally Enhanced Ion Acoustic Lines (NEIAL), which manifest themselves as backscatter power increases by many orders of magnitude above thermal levels, in incoherent scatter data. This is done using preliminary observation data from the EASI radar system, which was calibrated as part of this work, alongside co-located optical observations from the ASK facility. Using the data, and putting it into context of the surrounding global auroral activity, a greater understanding of how NEIAL structures relate to optical emission features is gained. These observations have large implications on current NEIAL production theories, many of which can be dismissed as they cannot explain observed phenomena.

Chapter 2 gives a description of the instruments and atmospheric models used in this thesis, including all of the instruments and satellites used to examine the background conditions surrounding EASI NEIAL observations.

Chapter 3 gives a summary of all the current NEIAL production theories in the literature and lists common features found in past NEIAL observations.

Chapter 4 describes the different radar experiment codes used with the ESR and EASI in this work. It elaborates on the calibration techniques employed on the radar system using incoherent scatter and satellite passes through the radar beam. The most accurate phase calibration results were produced via satellite tracking. The initial method presented in this work has been further improved by Schlatter et al. [2012], using optical camera data to constrain results.

As no enhancement observations were made during the first year of EASI operation, it was decided that a reanalysis of past radar data sets containing NEIAL events should be undertaken, to examine whether low level enhancements occurred surrounding strong NEIAL events. Such 'weak' enhancements are predicted by a number of NEIAL production theories. Chapter 5 describes the method used to detect non-thermal enhancements from ion line spectral parameters. Using this method, radar data from past results are analysed alongside new data sets containing NEIALs, and an analysis of non-thermal weak NEIAL enhancements is presented. Results show that non-thermal weak NEIAL enhancements do regularly occur surrounding 'strong' NEIAL events. The number of weak NEIALs detected is significantly increased if shorter integration times are used, indicating sub-second lifetimes for the events. Weak NEIAL enhancements consistently coincide with electron and or ion temperature and density enhancements, and appear to be largely unrelated to ion outflow events, bringing into doubt a number of possible production mechanisms.

Chapter 6 outlines the method by which NEIAL positions can be determined within the beam width of the EASI system, using the measured phase variation with altitude. During the winter of 2011-2012 observations of NEIALs were made with the EASI system. The event on 24 January 2012 was co-located with optical observations made with the ASK cameras. Two NEIAL observations are analysed using this method, with co-located ASK data used in one of the analyses. It shows that the derived NEIAL foot-point positions consistently match that of observed ASK 732.0 nm and 673.0 nm brightness enhancements. During both events, up and down-shifted shoulder enhancements are calculated to have spatially similar foot-point positions, but at times emanate from different altitudes.

Chapter 7 sets out the conclusion that only two of the currently proposed theories of NEIAL production can explain all observations. Results from the two events, one observed during day-side reconnection and the other during night-side reconnection, seem to favour different regimes of the 'beam-driven Langmuir wave' production theory. However, the night-side driven event most likely produces high altitude 'solitary kinetic Alfvén waves', to convert the initial high energy electron precipitation into lower energy electron beams, to drive Langmuir wave turbulence at lower altitudes. The chapter finishes suggesting future works that could improve observations and make a more statistically sound proof of production mechanisms.

Appendix A.1 describes the interferometric technique employed with EASI in detail along with the limitations and assumptions used. Appendix B explains the thermal loss mechanisms that were employed in Chapter 5 in detail and all the assumptions used in this process.

Chapter 2

Instrumentation

2.1 ESR

The European Incoherent SCATter network (EISCAT) Svalbard Radar [Andersen, 1995] consists of two incoherent scatter (IS) radars, a steerable 32 m and a fixed 42 m parabolic dish pointing with a line of sight along local magnetic zenith (181.0° Az, 81.6° El). The dishes have a beam width of 0.8° and 1.6° respectively, and utilise four separate channels each for ion line observations and six channels for observing different plasma line frequencies. The channels can be used to perform multi-frequency experiments where the frequency of transmission can be varied from pulse to pulse to maximize the possible transmission and recording rate. The facility is located close to Longyearbyen ($\sim$9 km away), on the Spitzbergan island of the Svalbard archipelago (78.15° N,16.02° E).

The two radars are centred 128 m apart and run at a central frequency of $\approx$500 MHz, having an optimal transmitting power of 1 MW. They are capable of transmitting pulses of $<$0.001 to 2.0 ms in length. These pulses can be coded using signal phase variation of $\pm\pi$. The facility is capable of recording data samples down to 11.25 MHz resolution, allowing for range separation of less than 1 km, if coded pulses are used. Whether the pulses are coded or not depends upon the radar experiment program used. These experiments are software created pulse schemes, usually with a specific aim in mind, although general purpose codes do exist. There are two main types of codes used, 'long pulse' and 'coded' experiments.

Long pulse experiments are mostly used for large extending objects in the ionosphere, at high time resolutions ($<$5 s) and at higher ranges ($>$500 km). The latter implies low height resolution ($\sim$20 km), i.e. the signal is integrated over the entire length of the pulse, so that higher signal to noise is achieved with fewer time integrations. These experiments are less computationally intensive to analyse than coded experiments.

Coded pulse experiments (in the case of ESR) use phase flips of π radians to break the pulse into smaller 'bits'. The technique of pulse coding has progressed greatly over the last 30 years, starting with the initial 'multi pulse' [Zamlutti, 1974] and 'Barker code' [Barker, 1953] schemes, which were replaced by 'random codes' [Lehtinen et al., 1997], to the current international standard of 'alternating codes' [Sulzer, 1989]. New techniques and refinements are continuously being developed, such as the use of power modulated 'perfect codes' described by Virtanen et al. [2009], and coding by orthogonal polarization, developed by Gustavsson and Grydeland [2009], which are not currently possible with the ESR. The advantage of coded pulse experiments is much greater range resolution than long pulse experiments ($<$1 km), as by coding the pulse the power can be approximated to be artificially contained within the length of a single bit in the code. However, to accomplish this the time resolution of the data is invariably sacrificed. In 'random' and 'alternating' code sets, integration times of 4 to 10 seconds are recommended or required, depending upon the experiment used.

In this work, data have been used from four different experiments (both long pulse and phase coded): Beata, LT4, LT1 and gup0, which are discussed in more detail in Section 1.5. Under usual running conditions, Level 1 'raw' data from the ESR is discarded to reduce the data storage burden, and Level 2 'fitted' data from both the ion line and plasma line channels is stored as atmospheric profiles for electron density, electron and ion temperatures, and line-of-sight ion velocities. These atmospheric profile data sets usually have a time resolution of 1 - 10 s.

Recent upgrades to the ESR facility have given it the capability to record raw voltage data, simultaneously on both the ion line and the plasma line channels, from both the 32 and 42 m antennas. This development and the existence of the two closely located radars has allowed for the possibility of limited interferometric experiments to be made, as discussed in Section 1.5, and described by Grydeland et al. [2004].

2.1.1 EASI

The ESR Aperture Synthesis Interferometry experiment (EASI) consists of three amplified 4×4 panel light 'antenna' installations. It is designed to complement the two existing ESR dishes to conduct more detailed interferometric experiments.

These installations combine the signal from each panel in a cluster, to work as three passive receive-only quadrapole antennas, with peak wavelengths around 500 MHz. Each antenna has a physical collecting size of $\sim 3 \times 3$ m, with the combined signals being pre-amplified by 20 dB before down sampling. The frequency range and gain pattern of the panels are such that they cover the entire frequency range of the ESR ion line channels, and have a much greater beam width than the ESR dishes. This limits any errors caused by side lobe detections and ensures that objects illuminated by either the 32 or 42 m dishes can be detected. The radars are capable of recording data at a sample rate down to 11.25 MHz (similar to that of the ESR), with recordings

being directed by a trigger pulse, connected to the ESR system. Only raw voltage is recordable in this system, with only a single channel available for each antenna.

Owing to their much smaller collecting area, the gain of the EASI antennas is much less than the two ESR dishes, and so they are not suitable for incoherent scatter ionospheric parameter analysis. The aim of the antennas is to detect highly reflective objects and auroral phenomena, such as NEIALs, and to use aperture synthesis imaging to find their position with great accuracy. NEIALs have been previous observed by the ESR and typically occur at altitudes between 200 km and 1000 km. EASI data can be combined with that from the ESR facility to provide raw quadrapole data from all five antennas / dishes and so allow interferometric imaging and positioning. In its raw form, the data produced are typically over 100 GB per hour.

2.2 Auroral Structure and Kinetics

Optical auroral observations were made using the Auroral Structure and Kinetics (ASK) platform co-located at the ESR facility on Svalbard, Norway (78.15° north, 16.02° east).

The platform was built by the University of Southampton in 2005, and is jointly run with KTH, Stockholm. The ASK platform contains three narrow field high resolution cameras, each one with an Electron Multiplying CCD (EMCCD) detector. The temporal resolution of the cameras is 20 - 32 Hz and each employs a changeable spectral filter. Each camera has a total of 512 $\times$ 512 pixels, but at resolutions above 5 Hz, a 2 $\times$ 2 binning process is used to produce an effective 256 $\times$ 256 resolution, to increase the detection rate above that of the noise. During the work, the ASK 1 filter was centred on high energy N_2 1P band emissions at 673.0 nm, with a Full Width Half Maximum (FWHM) of 3.0 nm. The ASK 2 filter was centred on low energy precipitation at 732.0 nm, particularly chosen for observation of the metastable O^+ doublet emissions, with a FWHM of 1.0 nm. The ASK 3 filter was centred on 777.4 nm with a FWHM of 1.5 nm. The cameras have a field of view of 3° $\times$ 3° when the telescopes were applied, and a 6° $\times$ 6° field of view without. All three cameras were aligned with the line of sight along the geomagnetic zenith, and the position of this centred in the FOV. The instrument is described in detail by Dahlgren et al. [2008].

Under usual conditions, the instrument is run continuously throughout the winter season, with images being processed and stored on a master computer system in the ESR facility and saved to magnetic tape. At 20 Hz resolution, the ASK instrument produces approximately 40 GB per hour. Therefore, 32 Hz resolution is typically reserved for when radar campaigns are being run.

2.3 Spectrographic Imaging Facility

The Spectrographic Imaging Facility (SIF) platform consist of several instruments, including an Echelle spectrograph with a meridian slit of 8°. It was equipped with a mosaic filter with four panels [Chakrabarti et al., 2001]. Panel O^+ (731.9 nm) allows spectra in the region of 728.0 - 740.0 nm to be recorded. The integration time of the spectrograph in this study was 30 s.

2.4 Multi-Instrument, Large Scale Analysis

Multiple international monitoring instruments and spacecrafts are used worldwide to track solar wind / auroral activity as it develops. Below are a list of those used in this analysis.

2.4.1 SOHO

The Solar and Heliospheric Observatory (SOHO) described by Domingo et al. [1995] is a spacecraft jointly built between ESA and NASA to study the Sun from its deep core to the outer corona and the solar wind. SOHO was launched in 1995 and includes twelve instruments to observe at multiple wavelengths from the solar core out to the heliosphere, as well as containing solar wind plasma instruments.

2.4.2 ACE

The Advanced Composition Explorer (ACE) spacecraft as outlined in Stone et al. [1998] is located at the L1 Lagrange point between the Earth and the Sun. It is equipped with magnetometers and a plasma analysis package. It acts as an early warning and analysis system to monitor solar wind material emitted from the sun that will collide with the Earth.

2.4.3 WIND

The Global Geospace Science (GGS) spacecraft also know as WIND was launched by NASA in 1994. its mission was to provide: complete plasma, energetic particle, and magnetic field readings for magnetospheric and ionospheric studies; to determine the magnetospheric output to interplanetary space in the up-stream region; and to investigate basic plasma processes occurring in the near-Earth solar wind [NASA, 1994].

2.4.4 IMAGE Magnetometer Network

The IMAGE network Viljanen and Häkkinen [1997] consists of a large number of magnetometer stations strategically placed throughout Scandinavia (Finland, Sweden and Norway). The data parameters given by these are D_b, H_b and Z_b, which are magnetic vector components in the incident magnetic field surrounding the sites. As reconnection and magnetospheric disturbances develop, these vectors will change. By using multiple sites in conjunction, any systematic changes to the magnetic field over Scandinavia can be tracked and monitored as they develop.

2.4.5 All Sky Camera Networks

The GLObal Robotic-telescopes Intelligent Array (GLORIA) [Mankiewicz, 2013], Magnetometers - Ionospheric Radars- All sky Cameras Large Experiment (MIRACLE) [Whiter and Partamies], and NORthern Solar-Terrestrial ARray (NORSTAR) [Donovan et al., 1998] networks consist of multiple all sky camera systems of differing wavelengths stationed in multiple locations throughout Scandinavia. Camera image and summary keogram data are freely available and can be used to track auroral activity or combined to produce pseudo images of total activity spanning from southern Finland to the Svalbard archipelago.

2.4.6 SuperDARN network

The Super Dual Auroral Radar Network (SuperDARN) is an international radar network built to study the Earth's upper atmosphere discussed in detail in Greenwald et al. [1995]. It consists of multiple radar stations throughout the northern and southern hemispheres. SuperDARN uses coherently scattered radar signals at 8 - 20 MHz over a number of scan directions (usually 16) creating a field of view that extends $\sim 52^\circ$ in azimuth. The range of the radars is from $\sim$200 km to more than 3000 km. The range resolution of the measurements is determined by the transmitted pulse length, which is 300 ms (45 km) in the common modes of operation. The temporal resolution of complete scans of the field of view is either 1 or 2 minutes in these common modes.

2.5 Atmospheric Models

2.5.1 MSIS-E-90

The Mass-Spectrometer-Incoherent-Scatter Extended (MSISE) model describes the neutral temperature and densities in Earth's atmosphere from the ground to thermospheric heights. Above 72.5 km MSISE-90 is based on the extensive data compilation and analysis work of A. E. Hedin

and his colleagues [Hedin, 1991]. Data sources include measurements from several rockets, satellites (OGO 6, San Marco 3, AEROS-A, AE-C, AE-D, AE-E, ESRO 4, and DE 2), and incoherent scatter radars (Millstone Hill, St. Santin, Arecibo, Jicamarca, and Malvern).

2.5.2 International Reference Ionosphere

The International Reference Ionosphere (IRI) model described electron density, electron temperature, ion temperature, ion composition (O^+, H^+, He^+, NO^+, O_2^+), ion drift, ionospheric electron content (TEC), F1 and spread-F probability of the atmosphere at multiple altitudes for a given time. For given location, time and date, IRI provides monthly averages of the parameters in an altitude range from 50 km to 2000 km. The major data sources are the worldwide network of ionosondes, the powerful incoherent scatter radars (Jicamarca, Arecibo, Millstone Hill, Malvern, St. Santin), the ISIS and Alouette topside sounders, and in situ instruments on several satellites and rockets. The IRI build-up and formulas are described in detail by Rawer and Bilitza [1990].

Chapter 3

NEIAL Theory

Naturally Enhanced Ion Acoustic Lines (NEIALs) have been found in Incoherent Scatter (IS) radar data since first documented by Foster and Aarons [1988]. NEAILs are large enhancements (over an order of magnitude in power above usual readings) in both the ion-acoustic lines and / or plasma lines, in the Incoherent Scatter (IS) radar spectra. They have been observed by all three EISCAT radars in Norway and Svalbard (VHF (224 MHz), UHF (931 MHz) and ESR (500 MHz)), as well as the Millstone Hill radar (440 MHz), PFISR and RISR-N (both 450 Mhz) systems in the US. However, with other IS radar systems, such as the Sondrestrom Radar (1290 MHz) in Greenland, NEIALs have never been observed.

Below are a number of theories that have been developed to explain NEIAL phenomena. The majority of these theories are described in an extensive review of the subject conducted by Sedgemore-Schulthess and St-Maurice [2001]. However, since its publication, a number of new results and theories have emerged. Due to these results, the majority of theories have been refined such that they involve particle (predominantly electrons) precipitation to some degree in their production process. The most currently accepted theory is that provided by Forme et al. [1995], but this topic is far from resolved and still widely debated in the scientific community.

3.0.3 Field Aligned Currents

The first recorded observation and theory of NEIAL production was from Foster and Aarons [1988], using the Millstone Hill Radar in the United States. The theory initially proposed by Foster and Aarons [1988] suggests that the enhancements in the down-shifted ion line are caused by a large field-aligned current, which would increase with altitude along a given magnetic field line. It is stated that this field-aligned current could be created by upward-streaming thermal electrons. Conversely, an enhancement in the up-shifted shoulder can be explained by oppositely orientated currents, caused by downward-flowing thermal electrons. This theory seemed to be backed up by incoherent scatter data, showing that the electron temperature was over four times

greater than the ion temperature during NEIAL observation ($T_e/ T_i > 4$). However, this theory assumed that a Maxwellian plasma distribution and thermal conditions were present, which have not been observed to be the case in more recent data.

Collis et al. [1991] also interpreted NEIAL enhancement observations as being caused by intense field-aligned currents, induced by streaming thermal electrons. In this event, the enhancements were highly correlated with red optical aurora. This theory is highly conditional and has been contested in that it cannot explain how simultaneous enhancements in both ion-acoustic lines occur, unless they are artefacts of temporal or spatial averaging. Additionally, the particle velocities required to account for the observed spectral enhancements require current densities of the order of several milliamps per square meter, which is much higher than any observed by satellites. However, Collis et al. [1991] claimed that due to the possible short-lived time of these currents, they may also be missed due to longer instrument integration times.

3.0.4 Parallel Electric Fields

Rietveld et al. [1991] made observations which seemed to show simultaneous large enhancements in both ion line shoulders. In addition, enhancements were seen at two distinct height regions, each exhibiting very different behaviour. These enhancements were also observed in conjunction with geomagnetic disturbances, high electron temperatures, red optical auroral arcs and in some cases ion outflow and inflow events. Measurements were made mainly along the geomagnetic zenith. Enhancements were interpreted in terms of field-aligned drifts of thermal electrons destabilizing ion-acoustic waves; i.e. a current-driven instability model. The ion-acoustic wave destabilization comes about due to the reduced Landau damping caused by the displacement of the thermal electron population relative to the ion population. As a consequence of this displacement an asymmetry in the ion acoustic spectrum can occur. Rietveld et al. [1991] argued that the electric fields producing the thermal electron motion were the result of field-aligned flows of soft auroral electrons depositing their energy in the F-region at horizontally poor conducting altitudes. This accumulation of energy and charge in turn creates intense parallel electric currents.

Using tristatic measurements with the EISCAT system, Rietveld et al. [1991] showed that perpendicular electric fields (like those proposed by Foster and Aarons [1988]) were not unusually large compared to non-enhanced conditions. Rietveld et al. [1991] cited rocket observations by Maynard et al. [1982] as showing evidence of strong electric fields as they experienced thermal electron fluxes 50 to 100 times greater than normally expected accompanied by soft electron precipitation of less than 1 keV. However, Boehm et al. [1990] came to an alternative conclusion, that what was witnessed was not due to the passage through strong electric fields, but the transit of a kinetic Alfvén wave of large amplitude ($>$100 mV m^{-1}).

3.0.5 Two Stream Instability

Large field aligned bulk ion outflow events were observed and presented by Wahlund et al. [1992]. It was calculated that ions reached field aligned velocities of up to 1500 ms^{-1}, and fluxes of over 2×10^{14} $m^{-2}s^{-1}$. These outflow events were separated into two different classes.

'Type 1' ion outflows, also known as ion-ion instabilities, are associated with strong perpendicular electric fields, enhanced ion temperatures and low plasma densities below 300 km. It is thought that they are caused by friction heating of ions as they travel through the neutral atmosphere, when strong electric fields are present. This increased ion temperature leads to strong pressure gradients that force ions up the magnetic field lines, resulting in ion outflow. In this regime, NEIALs are caused by the change in velocity, as this causes a drift to occur between two or more ion species in neighbouring field lines. The large relative drift velocities between the ions can cause an enhancement in either or both ion-acoustic lines. Which shoulder is enhanced depends upon the direction of flow of the ions relative to the receiving radar. The large electric fields involved would cause large electron densities to arise and so greatly enhance the power of the observed spectra.

Alternatively, 'type 2' outflow events or ion electron instabilities are connected with auroral precipitation and enhanced electron temperatures. It was stipulated that these are the result of strong or enhanced parallel electric fields, caused by the same process described by Rietveld et al. [1991], involving resistivity due to low-frequency plasma turbulence first theorized by Papadopoulos [1977]. As only one ion population is present in this method, only a single enhancement of either the up or down-shifted ion line can be produced. Simultaneous enhancements in both shoulders can only be explained if they are produced from different ion groups from different spatially separated regions within the radar beam integrated FOV.

3.0.6 Beam-Driven Langmuir Waves

Forme et al. [1995] observed enhancements which coincided with both high electron temperatures and strong ion outflows at altitudes between 300 and 700 km. These enhancements seemed to fill the criteria for an ion-ion instability process. In addition, lower altitude enhancements (100 - 200 km) were also observed where no ion outflows were present. These coincided with only slight electron temperature increases, and purely 'hard' electron precipitation (>1 keV). In this event, both ion lines were simultaneously enhanced, and a central frequency peak repeatedly occurred. These enhancements could not be described by either of the two-steam instability theories. Groves [1991] initially suggests that high level enhanced ion acoustic waves could be produced via the parametric decay of a beam-driven Langmuir wave. Forme [1993] furthered this theory by suggesting the driver for the Langmuir wave was an electron beam consisting of 'soft' electron precipitation (5 - 500 eV). This beam combines with atmospheric thermal electrons and creates a bump-on-tail electron energy distribution. This electron beam-driven

distribution in turn generates unstable growth of Langmuir waves via Landau damping. Once above a certain instability threshold this wave decays into a secondary Langmuir wave and an ion acoustic wave. This and subsequent decays couple non-linearly with ion-acoustic fluctuations through wave-wave interaction and result in enhanced ion acoustic lines and radar spectra.

Forme [1999] showed that these downward cascading waves from precipitating electrons could produce secondary up-going waves from wave-wave interactions with large fluxes of backscattered and secondary electrons, and produce ion-acoustic waves propagating in either direction along magnetic field lines. This method presented the possibility of simultaneously enhanced up and / or down-shifted ion lines emanating from within the same volume. The theory requires neither large current densities, nor differential ion drifts, but can account for mild electric field enhancements of up to 100 mV/m, and so connects best with 'type 2' ion outflow events. A caveat of this theory is that it cannot explain NEIALs under purely high energy precipitation (>500 eV), as it requires soft electrons to occur. It was further developed by Kuo and Lee [2005], backed by observations from the HAARP observatory, which proposed that this Langmuir decay occurs under two different regimes, one with a resonant and the other with a non resonant component. The processes behind these two regimes are explained in more detail in Section 3.1.3.

Kuo and Lee [2005] argued that 'resonant' Langmuir wave decay would be the dominant process and hence it is known as 'strong' turbulence. The process can be described by the formation of coherent wave packets via phase coherent plane wave (resonance) interactions between ion-acoustic and Langmuir waves, due to a much lower energy threshold being needed for the decay. The resultant secondary waves fully satisfy the dispersion relation for the system. In this process, the produced daughter waves would propagate downward, but produce limited frequency mismatching between each other and low levels of ion Landau damping, due to the frequency resonance.

Under the 'non-resonant' or 'weak' regime, waves produced from decaying Langmuir waves do not satisfy the dispersion relation for the system, and so are not matched to frequencies of the original wave. In this regime the cascade collapses into density wells, where phase is unimportant (non resonant), and is determined by intensity only. The Weak Turbulence Approximation (WTA) is a statistical theory describing the time evolution of these waves via wave kinetic equations, which assumes random phase. However, this approach is constrained in that it implies that the driving electron-beam energy density is relatively small, which may not necessarily be the case. As a consequence, the secondary waves can travel in any direction, but this decay is severely hampered by frequency mismatching and large levels of Landau damping.

3.0.7 Beam-Filling Solitary Waves

Ekeberg et al. [2010] observed NEIAL events exhibiting spectrally uniform enhancements over

the entire ion line. Additionally, no increased T_e/T_i ratios were associated with the events. Ekeberg et al. [2010] proposed a theory where beam-filling trains of solitary waves were a potential driving force for observed enhancements. The solitary waves are produced by large density perturbations (similar to Langmuir waves), caused by electron precipitation in the upper atmosphere, which disrupt the magnetic field. From these magnetic field perturbations, compressive solitary structures are generated. These structures propagate transverse to the magnetic field, at speeds similar to the ion acoustic velocity, and produce spectrally uniform power enhancements of approximately an order of magnitude above thermal levels. The magnitude and orientation of the magnetic field perturbations dictate the strength of the produced enhancements. This theory requires many specific conditions to hold, and would exhibit event lifetimes of the order of 5 -10 s. Therefore, it cannot explain the majority of NEIAL observations to date.

3.1 Current Evidence and Recent Results

Enhanced ion line spectra have been observed in association with a number of specific conditions. Understanding conditions and linked phenomena surrounding NEIAL events is vital to determine the processes which produce them. A summary of all NEIAL observations up until 2005 with associated phenomena was made by Blixt et al. [2005]. Findings included:

- All enhancements occurring with concurrent large geomagnetic disturbances, first described by Rietveld et al. [1991].
- When optical data has been present, events often occurred during soft precipitation events ($<$1 keV), or events containing high flux of electrons [Collis et al., 1991].
- Incoherent Scatter data surrounding enhancements often exhibits unusually high electron temperature readings, as noted by Foster and Aarons [1988] and Wahlund et al. [1993].
- Enhancements coincided with electron density enhancements in the E region, and gradual heating in the F region, as observed by Rietveld et al. [1991] and Forme et al. [1995].
- Intense ion outflows were recorded to coincide with enhancements by Wahlund et al. [1992] and Forme [1999].
- Strong optical red emission appeared spatially alongside enhanced spectra (Collis et al. [1991] and Sedgemore-Schulthess et al. [1999]).

A statistical analysis of all past NEIAL spectra was conducted by Ogawa et al. [2006]. This study seemed to show that consistently:

- Simultaneous enhancements have been observed in both ion-acoustic lines and both plasma lines.

- Enhancements can occur in one or other of the ion acoustic shoulders independently, with or without plasma line enhancements, which can also occur up-shifted or down-shifted independently.
- NEIALs are observed typically between 300 and 700 km. However, enhancements have been observed intermittently as low as 138 km [Rietveld et al., 1991] and as high as 1600 km [Ogawa et al., 2006].
- Down-shifted ion line enhancements dominate at $>$1000 km where they are approximately eight times stronger than up-shifted spectra.
- Enhancements in the up-shifted ion line appear less frequently, are usually weaker in power and vary more with altitude, apart from at $<$600 km, where they can be more powerful than the down-shifted spectra.
- Separation in frequency between the up and down-shifted frequencies increases with altitude up to $\sim$500 km, where the separation no longer alters and plateaus.
- The centre frequency of the enhanced spectra shifts towards lower frequencies with increasing altitude.
- A small proportion of enhancement events countered all previous results and showed stronger down-shifted enhancements than up-shifted at all altitudes.

An earlier statistical analysis by Forme et al. [1995] showed that enhancements appeared to occur more frequently with the EISCAT VHF (224 MHz) radar than with the UHF (931 MHz) system. It was suggested that this was due to a wavelength dependence of the enhancements. Cabrit [1995] tested model generation methods for the observed enhancements, and concluded that the irregularities observed must have widths much smaller than that of the radar beam.

3.1.1 Recent High Resolution Results

All of the above enhancement observations were severely limited by the time resolution of the radar data of $\sim$6 - 10 s, and most by a lack of high spatial resolution co-located camera data. A number of recent observations have since been made using the ESR and PFISR radar systems, which can record raw data from multiple antennas. In addition, higher resolution cameras have also been added in situ with these radar systems.

A number of campaigns by Grydeland et al. [2003], Grydeland et al. [2004] and Stromme et al. [2005] were undertaken using the ESR to perform rudimentary one-dimensional interferometry experiments on NEIAL events, with magnetic field-aligned, using the 32 m and 42 m dishes. Initial interferometric results showed that for at least one event, the source of NEIALs came from a very localized area constrained to $\sim$300 m perpendicular to the magnetic field, at an

altitude of 500 km, calculated using a time integration of ∼0.2 s. All NEIAL events observed with the ESR occurred in conjunction with dynamic rayed or flamed aurora with strong red auroral background emissions. However, previous observations made from the EISCAT UHF and VHF radars in Tromsø with high resolution optical data seemed to show NEIALs occurring around the edges of stable red arcs [Collis et al., 1991].

In addition to auroral enhancements, results from a number of ionospheric heating experiments exist, which seem to show consistent results. Heating experiments involve exciting the ionosphere with high energy RF radiation (∼2 - 12 MHz), which is altered in frequency and periodically turned on and off. It has been observed that these transmitted RF waves can decay ion-acoustic waves and Langmuir waves, at auroral altitudes (90 - 250 km).

3.1.2 Implications and Limitations

The above observations have often in the past been used to dispute or back up different enhancement production theories. So far, no one theory can explain all historically observed enhancements. The conclusions derived from historical observations can be summarised:

Enhancements observed in conjunction with high levels of dynamic red aurora support the theories of 'beam-filling solitary waves', 'Alfvénic wave driven' and 'electron beam-driven Langmuir turbulence' as production mechanisms, as these depend upon high flux soft electron precipitation. Alternatively, enhancements connected with the edge of strong auroral arcs support the 'current-driven' and 'two-stream instability' theories.

Events that exhibit up-shifted plasma wave enhancements cannot be explained by theories that use 'Landau damping' mechanisms to enhance ion line spectra. In the reduced 'non-resonant Landau damping' regime, low frequency waves grow unstable as shown by Kindel and Kennel [1971], and in turn decay into increasingly lower frequency waves. Therefore, generation of high frequency plasma waves cannot be explained by this theory. Observations of high frequency waves would exclude both the 'two-stream' and 'Langmuir turbulent' theories.

The wavelength-limited nature of observations (no observations with radars at 1290 MHz and above) seems to show a resonant factor to the production process, further indicating that a wave or particle-driven process is a likely cause of enhancement, as opposed to current-driven theories, that cannot explain this cut-off.

Observations taken by the ESR were conducted field-aligned. Therefore, theories that produce only or a large proportion of wave modes propagating at angles perpendicular to the magnetic field line (such as the theory of 'perpendicular electric field currents') cannot be used to explain these enhancements.

Proposed observations of 'beam-filling solitary waves' are based solely on a single event using IPY data with a time resolution of 6 s. Therefore, more observations at higher time resolutions

are needed to determine if the viewed spectra were artefacts caused by using long integration lines. This seems to be the only event to date to which this theory can be attributed, severely limiting its validity.

3.1.3 Simulations of Langmuir Turbulence

The currently most widely accepted theory of Langmuir turbulence is explained below. This synopsis includes a number of recently improved simulations of the Forme [1993] model done by Guio and Forme [2006]. To produce ion-acoustic line enhancements, the regime requires coupling of the high-frequency Langmuir waves with low frequency ion-acoustic waves. This coupling is described by the Zakahrov system of equation (ZSE), describing a three wave process, resulting in the cascade of Langmuir waves to lower wavenumbers. This results in one of two regimes being produced, strong or weak turbulence.

The Zakharov model showed that the cascade and cavitation regimes of Langmuir turbulence exhibit very different spectra, and so produce different results if seen by an IS radar. For the test run by Guio and Forme [2006], the model parameters were given for an altitude of ∼300 km at auroral latitudes 5×10^{11} m$^{-}3$, T$_e$ = 3000 K , T$_i$ = 1000 K, $\upsilon_{ec} = 100$ s^{-1} and $\upsilon_{ic} = 1$ s^{-1}, beam velocity $\upsilon_b = 4.5 \times 10^6$ ms^{-1} and a beam energy of 58 eV. The beam was assumed to be propagating downward. However, this may not always be the case, as Langmuir waves can be triggered by either up or downward-going electron beams.

The cascading resonant enhancement turns out to be highly dependent upon wavenumber, with a maximum power gain of 60 - 70 dB at 1.5 - 2 times the radar wavenumber (k). At wavelengths above or below these wavenumbers enhancements are calculated to be 10 dB or less. Large spectral enhancements are predicted to be accompanied by highly asymmetric spectra. At wavenubers $<1.75\times$k$_{\mathrm{radar}}$, the down-shifted shoulder is enhanced, while with wavenumbers $>1.75\times$k$_{\mathrm{radar}}$ the up-shifted shoulder is enhanced. It is predicted that large enhancements will have much smaller statistical variability than small enhancements.

Cavitating non-resonant turbulence presents relatively constant and strong enhancements of 90 - 100 dB over the entire wavenumber range sampled, with maximum gain at $k \sim 2k_{radar}$. Less than k $< k_{\mathrm{radar}} \times 1.5$, the spectra are slightly asymmetric, such that the lower shoulder is enhanced slightly more than the upper shoulder. Conversely, at k $> k_{\mathrm{radar}} \times 2$ the upper shoulder is slightly enhanced. Between these ranges the spectra are rather symmetric. In stronger cavitating cases, the central peak is seen at zero-frequency at small wave numbers. In the weaker case, this central peak can also appear, but not so strongly. The magnitude of this peak in the weak case decreases with increasing wave number. In order to observe large wave numbers, the energy of the electron beam would have to be very low, of a few eV. Such beams are scattered via collisional quenching before reaching the ionosphere. Therefore, very high wavenumber radars such as the Søndre Strømfjord ($k_s \sim 54$ m^{-1}) cannot detect these phenomena.

3.2 Implications and Unanswered Questions

The previous sections have shown that although much work has been done on the theory and classification of NEIALs, there are still many unanswered questions. Many past observations (particularly those before 1995) have used radar integration times much larger than the time scales of the enhancement events and so data can be misleading. Additionally, past camera systems used have been at low resolutions and not exactly co-located with the radar systems, meaning data could be easily misinterpreted.

The common consensus is that Langmuir waves can explain a large majority of events and so likely play an important role in NEIAL production. However, a number of predicted outcomes from this theory have not been observed, for example the Zakharov model suggests that given plausible conditions, NEIAL power enhancements should vary from 70 to 95 dB above normal thermal levels. To date, they have only been recorded up to 50 dB above this thermal level. These discrepancies do not necessarily discredit the theories and could be due to many other factors, such the limitations of the equipment, or currently not understood atmospheric interactions hindering these enhancement levels.

Recent models show that complex wave interactions are likely to occur in the upper atmosphere and that Langmuir waves, kinetic Alfvén waves and whistler waves can couple and decay into one another. Results also show high levels of solitary kinetic Alfvén waves at higher latitudes. Large electric currents have also been observed via rocket and satellite direct measurements, showing that these too may contribute to the enhancement of ion spectral lines in radar results. Exactly how many of these factors take part in individual events needs to be examined to work out fully what processes are occurring in the upper atmosphere. With the addition of radar signal positioning and high resolution co-located cameras, this work aims to give an accurate examination of NEIAL events. Results from these follow in Chapters 5 and 6, and their implication on the above theories discussed in Chapter 7.

Chapter 4

EASI Codes, Error Calculations and Satellite Tracking Methods

This chapter describes the different radar experiment codes used with the ESR and EASI in this and previous work. It also describes the calibration techniques employed on the radar system and their verification using satellite passes through the radar beam.

4.1 ESR Radar Programmes

The ESR and EASI can run a number of different radar experiments where the phase and frequency of the transmissions can be altered. The most basic experiments involve single frequency long pulses which are easy to process. Developments over the last 40 years have shown that coding these pulses in phase throughout the pulse length and employing multiple frequencies can greatly increase the height resolution and signal power of the results. However, processing of these coded experiments is greatly complicated depending on which techniques are used and how the data are used. Listed below are the experiments used in this work with a brief description of their strengths and limitations.

4.1.1 LT4

The two main NEIAL observations analysed in this work were recorded with the LT4 experiment. LT4 is a long pulse experiment designed for high temporal resolution, which uses two Inter Pulse Periods (IPPs) per cycle, each IPP in turn transmitting at two frequencies. This experiment has been specifically set up to record raw data products of high power spectral objects over a large range of altitudes. The experiment has been improved throughout a number of versions ranging from A to F. The two IPPs have lengths of 320 μs with frequencies of 499.35

and 499.55 MHz for IPP 1, and frequencies of 499.45 and 499.65 MHz for IPP 2. The experiment has an effective range up to 1250 km in altitude, limited by the pulse transmission rate to produce the greatest signal strength.

This experiment has been used for the majority of the present work, as the data are much easier to process than more complex experiments. The long-pulsed nature means that only very broad height resolution (28 km) is possible with this experiment, which is not a large problem for NEIAL studies where the structures are vertically extended by typically greater ranges than this. Figure 4.1 shows an example of LT4-F products of a satellite observation. It shows the individual radar power spectra (top), the cross-correlation of the spectra (row 2) and the cross-coherence between the spectra (bottom). From these data, 'aperture synthesis imaging' (ASI) images can be performed.

4.1.2 Beata

Beata is a complex alternating coded experiment. It incorporates 30 bit (50 μs each) codes, over 64 pulses (IPPs) to complete a cycle. The code sequences are designed to cancel out any range ambiguities over a full cycle, which takes 0.4 s. The experiment has been designed for high spatial resolution (2.8 km) data of aurora between 120 and 550 km, and can record raw data products. It is hoped that by continuing to run EASI with the newly updated Beata experiment, the five antenna data sources can produce higher altitude resolution NEIAL observations in the future. Unfortunately, the coded nature of Beata presents numerous problems. As a time integration of 0.4 s is needed to remove range ambiguities, for NEIAL variations ($\sim$0.1 - 0.2 s), incomplete code sets will need to be analysed. Range ambiguities lead to height ambiguities of the signal when computed via a lag profile matrix. Figure 4.2 shows the range ambiguities that arise from analysing individual quarters of a full code set (0.1 s). If integration times of less than half a code set are needed, the ambiguity becomes too great to be used with this method. One solution is to use lag profile inversion. Another problem encountered during this work was that initially, only 1 in 64 of the codes were recorded by the EASI system, leading to completely erroneous data during the first two seasons of operation.

If analysis shorter than a full code cycle is needed, then the commonly used lag profile matrix method cannot be used without producing serious data ambiguities, and so should be avoided. An alternative analysis technique called lag profile inversion (LPI) has been developed by Virtanen et al. [2008]. This technique produces radar autocorrelation functions for partial sets of coded pulses, given transmission profiles are also provided. As Beata records transmission and received profiles, this method can be applied. Unfortunately, as LT4 does not record transmission profiles, this technique cannot be applied for analysis of that experiment.

Initial tests have shown that the LPI technique works well with past Beata experiments, and can analyse data products from both the ESR dishes down to 0.2 s with good accuracy, and to 0.1 s

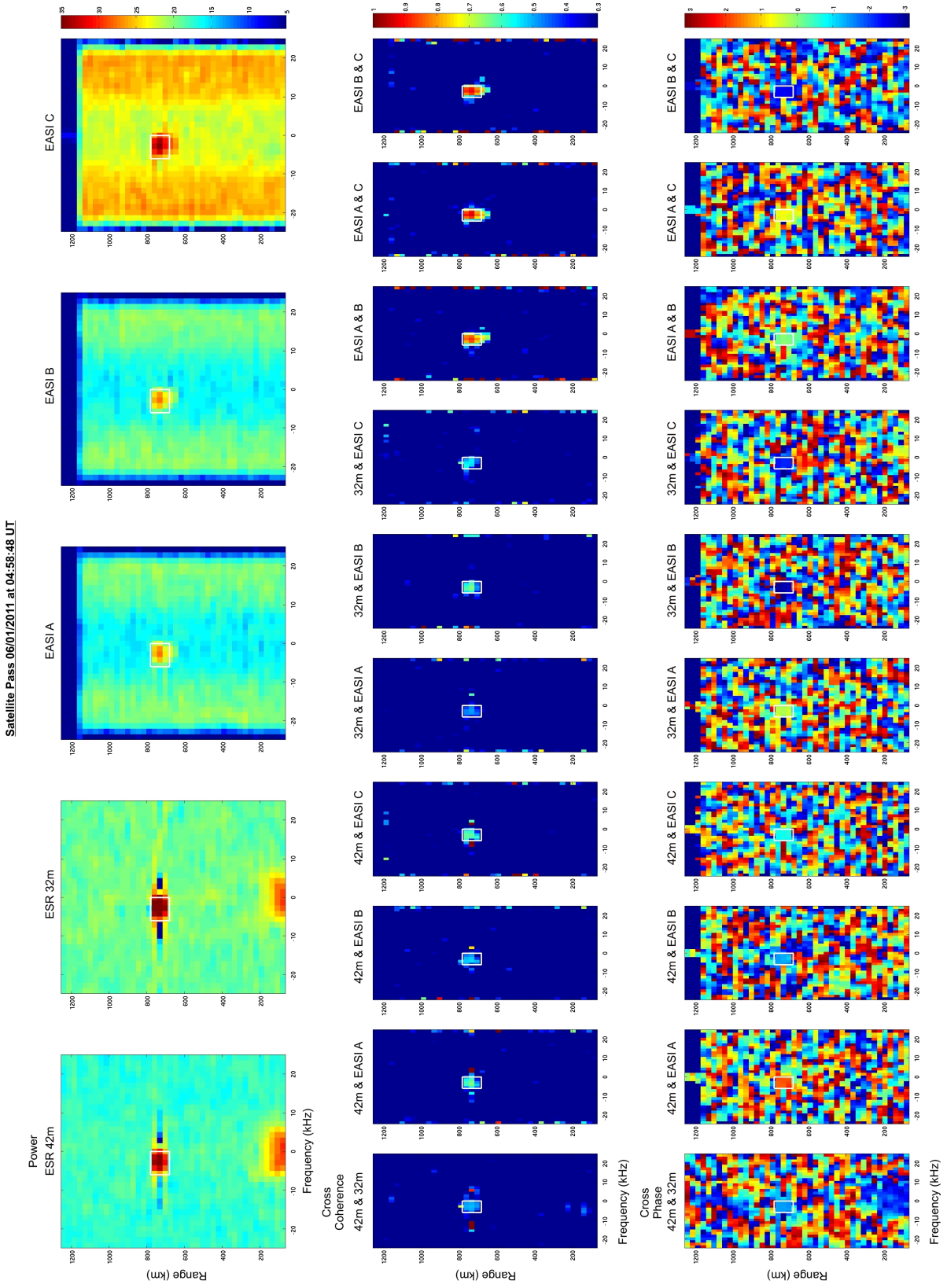

Figure 4.1: Plot of satellite signature seen in all 5 antennas 04:49:58 UT 06/01/2011 running LT4, (left to right: 42 m, 32 m, EASI A,B,C), power profiles (top row), cross-correlation (second row) and cross phase (third row).

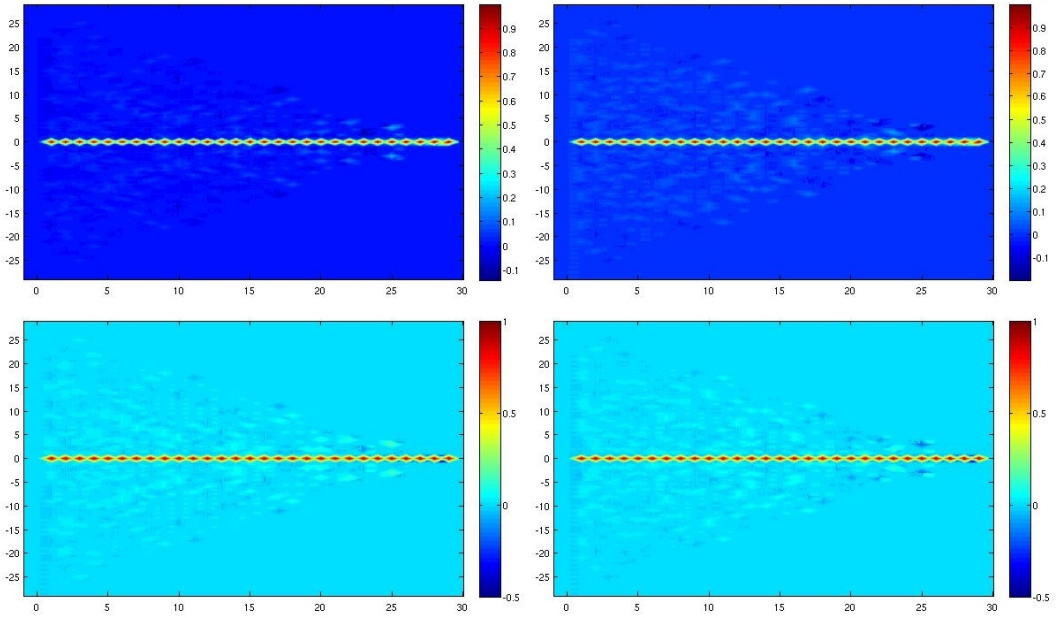

Figure 4.2: Diagram of Range Ambiguity Function (RAF) per lag product for quartile portions incomplete code sets, with lag number (x axis) and range gates (y axis) relative to the processed range gate. Top left: codes 1-16 RAF, top right: codes 17-32 RAF, bottom left:codes 33-48 RAF, bottom right: codes 49-64 RAF.

with some minor artefacts. Figure 4.3 shows the reflected power detected from all ranges and lags available from 0.2 s of integrated data. It shows that no range ambiguities are present if the LPI method is used. Cross-correlation of spectra between the 32 m and 42 m dishes has also been shown to be successful at this time resolution. Figure 4.4 shows the cross-correlation values recorded by the 32 and 42 m ESR dishes before (top) and during (bottom) a satellite pass.

4.1.3 LT1H

LT1 is a simple long pulse experiment with a single pulse at one frequency (499.85 MHz) per IPP. The data can be recorded as raw voltage samples as well as fitted parameter products. The latest version of this experiment (H) is used in this work. It was initially used to test the interferometric capabilities of the two ESR dishes, and to view NEIAL events. It has since been superseded by the LT4 experiment, which produces similar results with much higher signal power.

4.1.4 gup0

Gup0 is a long pulse experiment with four IPPs per cycle. The experiment transmits and records different pulse lengths alternately for two sets of four frequencies per IPP. The highest achievable

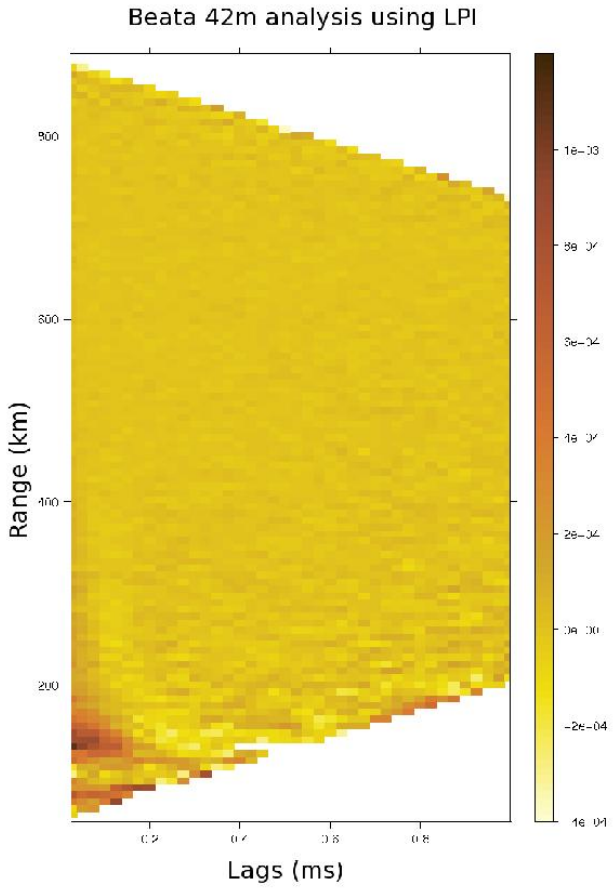

Figure 4.3: 0.2 s integrated power spectra of the ESR 42 m antenna Beata experiment using LPI. Small scale auroral structures can be clearly determined which are many orders of magnitude in power below that of NEIALs. *Courtesy of Virtanen et al. [2008]*

height resolution is 58 km, and it ranges between heights of 200 and 900 km. Only integrated parameter products are available, at time steps of 10.0 s. This experiment has been used for NEIAL analysis in the past [Ogawa et al., 2006] due to its high altitude range, and use of multiple frequencies. However, owing to its limited temporal and spatial resolution, it has now been replaced by more recently developed codes which record raw data.

4.1.5 IPY

During the International Polar Year (IPY) between 1 March 2007 and 29 February 2008, the ESR was run continuously with a specialised radar. This experiment consisted of a 30 μs $\times$ 30 bit alternating code, ranging between 43 and 507 km, with peak power between 200 and 400 km. The altitude resolution of the experiment was between 2.2 and 4.5 km depending on the altitude being sampled, with lower altitudes having the best resolution. The raw data was integrated to 6.0 s samples to reduce the amount of data [Ogawa et al., 2011] over the year of

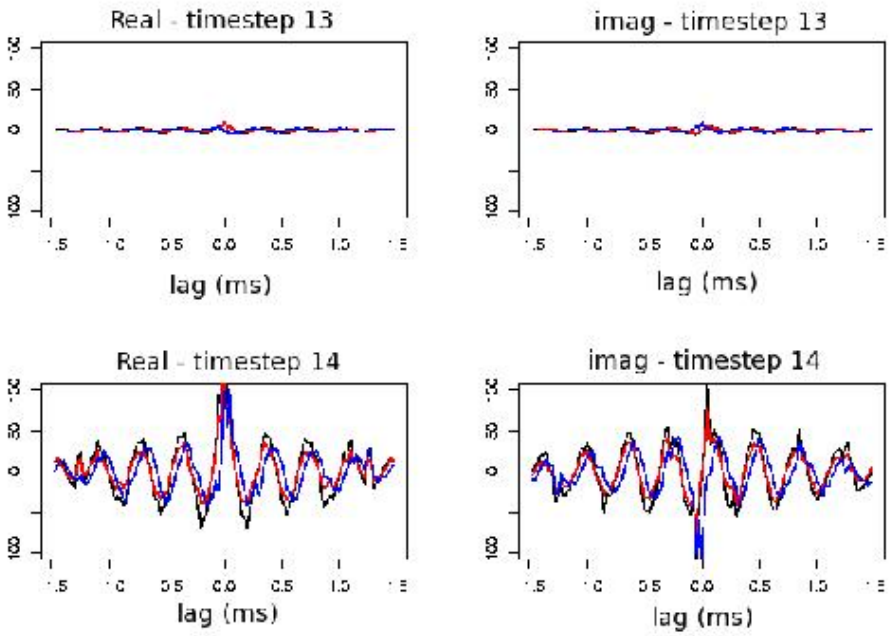

Figure 4.4: Cross-correlation of ESR antennas using Beata and LP1 with 42 m antenna ACF (black), 32 m antenna ACF (red), and cross correlation function (blue), with 0.1 s time resolution. Top row is during normal auroral activity and lower row with a satellite pass. Left panels contain real parts of the ACFs, and those on the right contain the imaginary parts.

operation. Data containing NEIAL events from this period have been studied statistically by Ogawa et al. [2011], with particular attention paid to ion up-flows.

4.2 Satellite Tracking and Trajectory Determination

The tracking of satellite passes can be used to test the accuracy of ASI modelling, as well as to calibrate individual radars in phase (see Section 1.5). However, before the satellite passes can be used, their trajectory and velocity (and so position with time) must be known. This positioning can be done optically using co-located cameras (Sullivan et al. [2006]; Schlatter et al. [2012]) or calculated using the radar data. The following methods in this chapter were applied using radar data, without the use of optical data.

4.2.1 Initial Satellite Velocity Estimation

From the altitude range where the satellite signature is detected, and given the radar elevation, the altitude of the satellite can be estimated as:

$$\mathrm{Alt} = \mathrm{Range} \times \cos(90 - \mathrm{El}_{\mathrm{radar}}) \tag{4.1}$$

where Alt is the altitude of the satellite in m, Range is the apparent range of the signal in m and $\mathrm{El}_{\mathrm{radar}}$ the radar elevation. By assuming a geosynchronous orbit a velocity can then be calculated by:

$$\mathrm{V}_{\mathrm{SatGeo}} = \sqrt{\mathrm{g}_{(e,\mathrm{alt})} \times \mathrm{R}_e^2/(\mathrm{R}_e + \mathrm{Alt})} \tag{4.2}$$

where $\mathrm{V}_{\mathrm{SatGeo}}$ is the geostationary velocity of the satellite, $\mathrm{g}_{e,\mathrm{alt}}$ the gravitational force of the Earth at the satellite altitude, and R_e the radius of the Earth.

Due to the polar nature of the observed satellites, these assumptions may not be entirely accurate. However, any error in velocity will manifest itself as a constant offset when the trajectory is calculated, and so not affect the final calibration results, as discussed in Section 1.5. These calculated velocities are used as initial estimates, which can be improved after subsequent calculation if needed.

4.2.2 Power Interference Fringes

The trajectory of satellite passes relative to the ESR 32/42 m baseline can be calculated directly from power profiles of data containing a satellite pass. Raw radar data are needed to view these over the time scales of satellite passes. Figure 4.5 shows an example of data from the LT4 experiment. It contains many peaks and troughs in power, in all baselines, during satellite passes. The peaks are highlighted in green, and seen to occur regularly with time.

The LT4 experiment is meant to have transmission on the 42 m antenna only so that the smallest beam width is used, with the signal received on all five EASI antennas. It was discovered by Schlatter et al. [2012] that the fringe pattern was due to an imperfect separation of wave-guides to the 32 m and 42 m ESR antennas, meaning a small proportion of transmission occurs on the 32 m ($\sim 25\%$) and the rest is transmitted on the 42 m antenna. When these transmissions from both antennas combine they interfer constructively and destructively depending upon the position above the radars. Figure 4.6 shows a computed model of the interference pattern at 500 km in altitude above the ESR. The nature of this intensity fringe pattern is the same as Young's double slit experiment, such that:

$$\mathrm{X}_{\mathrm{sep}} = \lambda \times \mathrm{Z}/w \tag{4.3}$$

where $\mathrm{X}_{\mathrm{sep}}$ is the peak separation, λ is the wavelength, Z is the distance from the centre of the sources, and w the source separation.

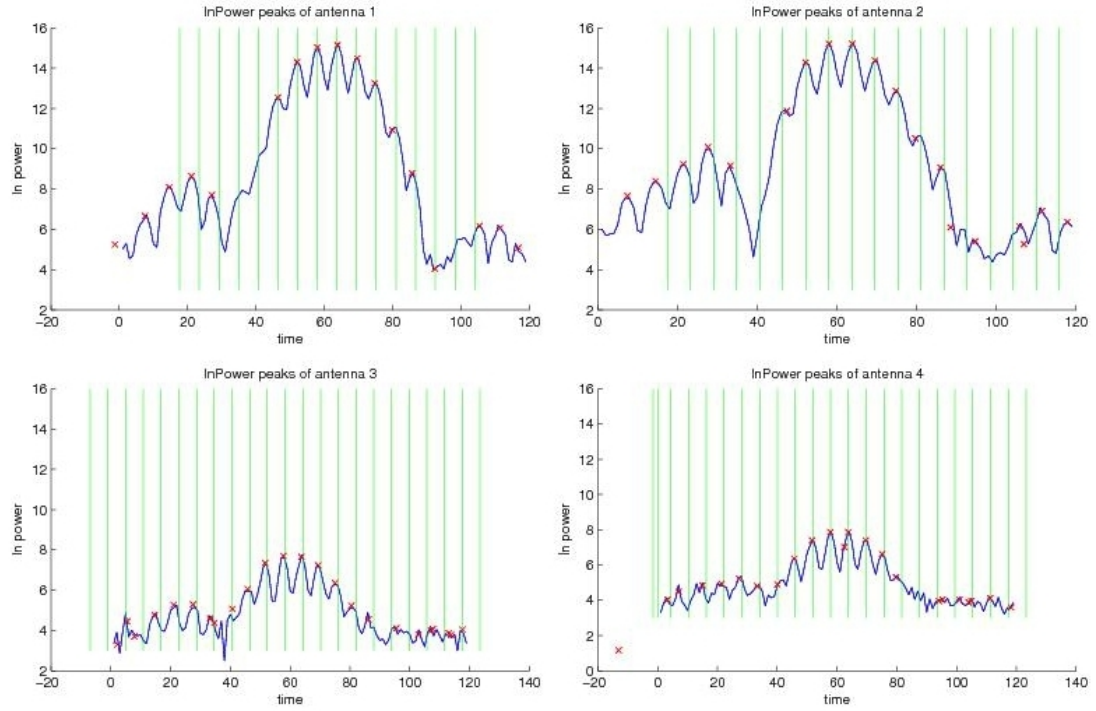

Figure 4.5: Ln Power Plots (blue) of 32/42 m, EASI A/EASI B, EASI A/EASI C, EASI B/EASI C baselines, power peaks (red x), peak separations (green).

The exact position of the constructive fringes is dependent on the phase and delays of the transmission sources. For the purposes of this diagram, the source is assumed to be at zero delay and phase offset. Although these are unknowns for the calibration and trajectory analysis, these added factors should not affect the end results, as this method uses only the peak separation and not the peak position along the 32 m and 42 m baseline to calculate the satellite trajectory.

A program was written to calculate the peak separation in the power fringes for all of the different baselines in terms of time (s). To convert this time scale into distance (m) travelled by the satellite, this was divided by the sample rate and multiplied by the calculated satellite velocity. As the positions of all the antennas are known, the positions of the fringes for a given range/altitude are known relative to the 32/42 m baseline (line between the antennas). By assuming that the satellite is travelling in a set direction at a given angle θ to this 32/42 m baseline, the separation of power peaks can be estimated relative to the 32/42 m separation, such that:

$$\text{Error} = \sum (dx_{\text{bl}} - (dx_{32/42\text{m}} \times \cos(\theta_{sat} + \theta_{\text{bl}}))) \tag{4.4}$$

where Error is the error in the data, dx_{bl} is the power separation in m of the baseline , $dx_{32/42\text{m}}$ is the calculated power of the separation of the 32/42 m baseline, θ_{sat} is the angle of the satellite trajectory and θ_{bl} the baseline angle relative to the 32/42 m baseline. By entering this θ as a

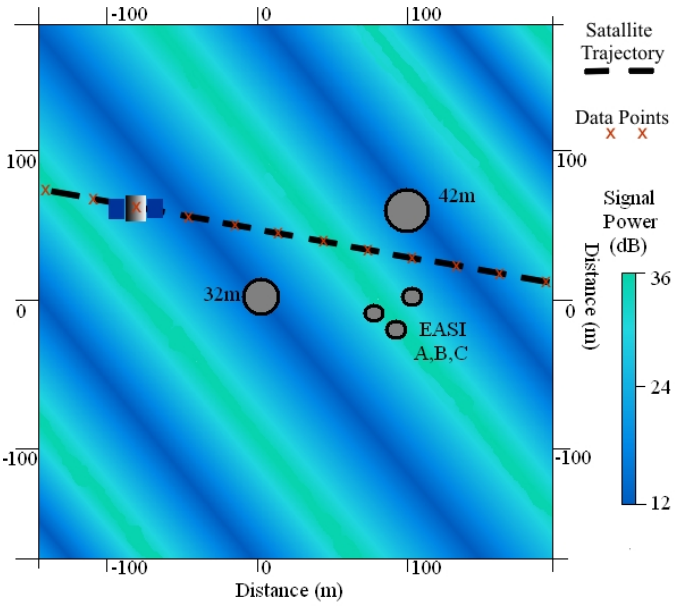

Figure 4.6: Plot of estimated satellite trajectory for a satellite pass with predicted fringes (blue), radar positions (gray) and estimated trajectory and data positions (red and black).

variable into a least square error fitting program, the angle θ which satisfies all the recorded data with the lowest error values can be found (see Figure 4.6). Any error in initial velocity calculations will appear as a constant offset and so should not affect fitting process. After the best angle of satellite trajectory is found, the velocity can be entered as a variable and under the same LSF method a velocity that best fits the data can be found.

4.2.3 Trajectory Tracking via Phase Variation

An alternative and potentially more robust method for determining the trajectory of a satellite from radar data is by viewing the gradient in change of phase, over a satellite pass. Depending upon the positions of the antennas, the range of the target plane and the wavelength of the transmission, the phase of a received signal from a uniformly scattering object (such as a satellite) will alter as its position changes through time. Assuming a uniform scatterer in a plain at a set altitude above the radars, the phase of an object can be summarized by:

$$\Theta(\mathrm{x},\mathrm{y},\mathrm{Z}) = \mathrm{G}(\mathrm{x},\mathrm{y},\mathrm{Z}) \times \exp^{i(2\pi/\lambda \times dl)} \tag{4.5}$$

where Θ(x,y,Z) is the phase at position x, y at altitude Z, $\mathrm{G}(\mathrm{x},\mathrm{y},\mathrm{Z})$ is the gain power at position x, y, Z (assuming a non symmetrical distribution), λ is the wavelength of the radar and dl is the distance from the radar to the target.

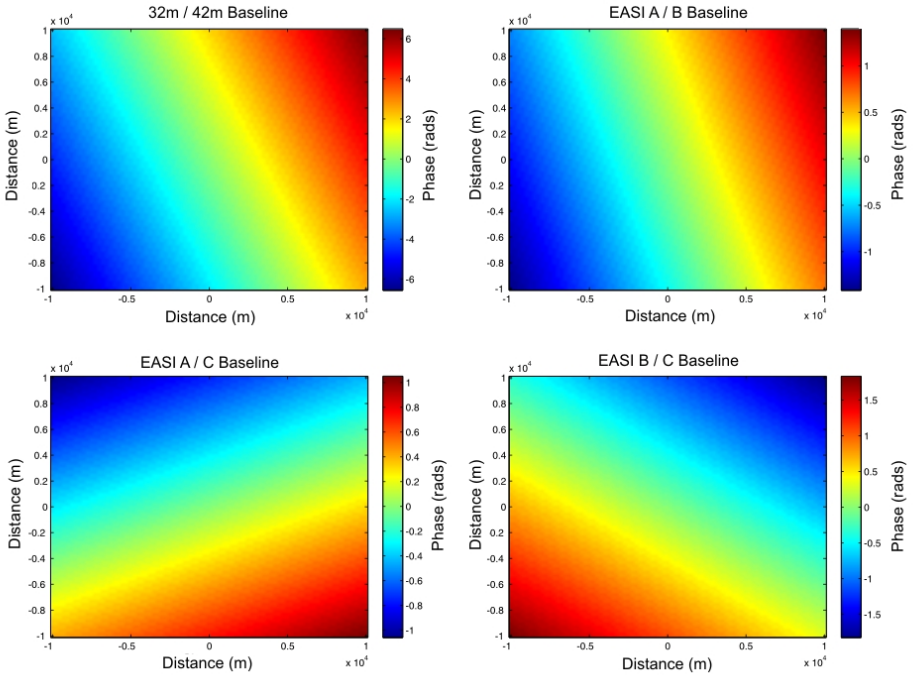

Figure 4.7: Map of phase gradients for EASI baselines at a range of 500 km above the radars.

For a given baseline (a combination of two antennas), the phase offset caused by this distance dl can be calculated as the difference between the individual dl values for each of the radars:

$$dl_{a,b} = dl(a) - dl(b) \tag{4.6}$$

By plotting these values to a fixed grid at a plane vertically above the radars, a map of where phase values wrap from - 2π to +2π for each baseline can be created.

A phase gradient can be calculated by the inverse of the distance along the baseline in m from one phase wrap to the next. With the knowledge of the antenna positions this can be calculated to give the gradient in x and y. Figure 4.7 models the phase variation with area for four baselines at an altitude of 5000 km above the EASI system. The change in phase in the area above the radars is dependent on the orientation and separation of the two radars, with different baselines producing different phase maps.

Relatively uniform changes in phases and points when phase wraps occur can be clearly viewed in satellite pass data for all antenna baselines. Figure 4.8 shows the phase values recorded by all baselines during a satellite pass, with the majority of baselines observing systematic phase variation during the event. Therefore, these data seem to validate the assumption that satellites behave as a uniform coherent scatterer.

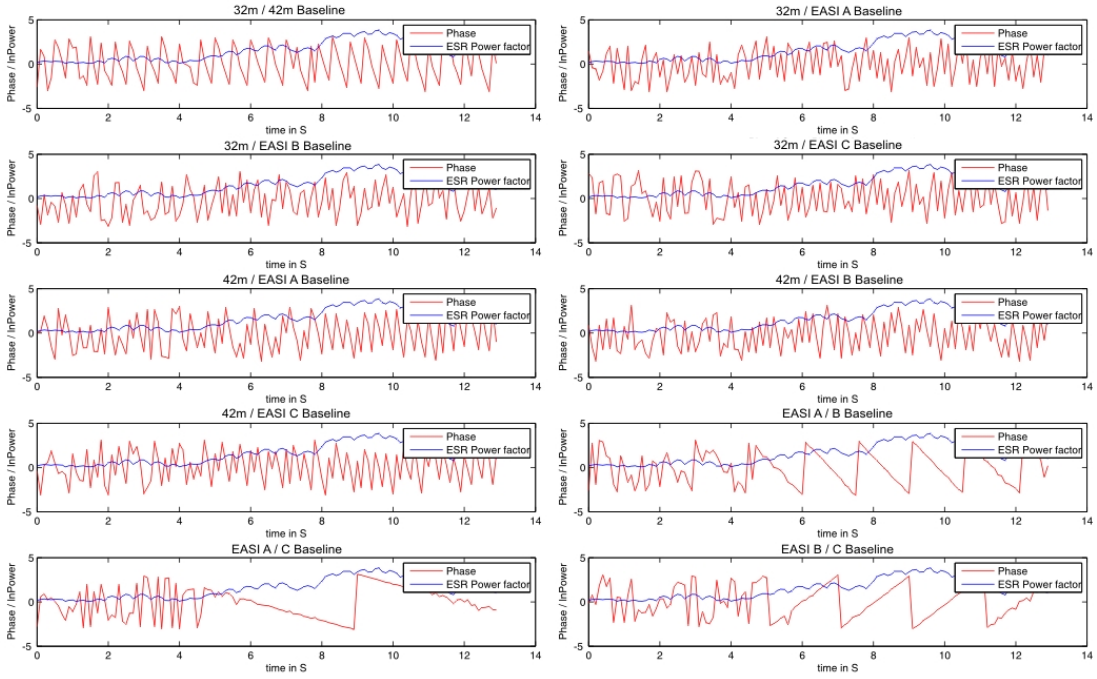

Figure 4.8: Phase plots for each EASI baseline over a satellite pass. Phase gradient is coherent when the satellite is within main lobe of the radar beam.

The change in gradient along each baseline with time was found by initially applying a median filter to remove noise and taking account of the data sample rate. Phase change over time was then converted into distance (m) by estimating the satellite velocity as described in Section 4.2.1. These data were used to compute an initial angle for the satellite trajectory for each baseline such that:

$$\triangle \phi = \frac{d\phi}{ds_{\mathrm{sam}}} / dt_{\mathrm{sam}} / v_{\mathrm{sat}} \tag{4.7}$$

where $\triangle\phi$ is the gradient of ϕ in m for a given baseline, $d\phi/ds_{\mathrm{sam}}$ is the gradient in phase with sample, dt_{sam} is the sample rate of the data and v_{sat} is the velocity of the satellite.

If a satellite travels at a trajectory angle ϕ relative to a reference direction in x and y, for example the 32/42 m baseline (as used in this case), then the gradient of phase change can be estimated in time for each baseline given the satellite velocity and sample rate.

$$\triangle \phi_{\mathrm{bl},\phi} = \triangle\phi \times \cos(\phi_{\mathrm{sat}} + \phi_{\mathrm{bl}}) \tag{4.8}$$

where $\triangle\phi_{bl,\phi}$ is the gradient in ϕ for the given baseline and angle theta, ϕ_{sat} is the angle of the satellite trajectory, and ϕ_{bl} the baseline angle relative to the reference frame.

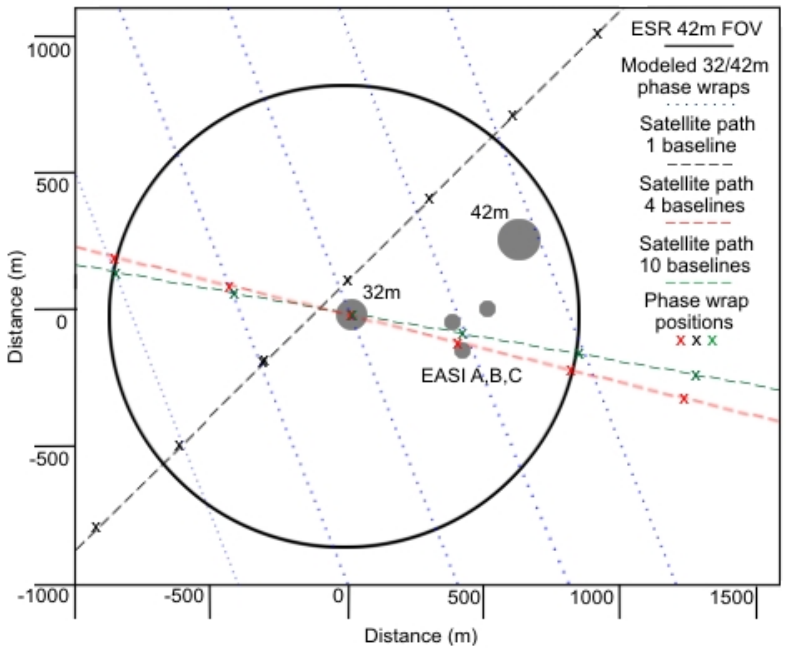

Figure 4.9: Map of ESR 42 m FOV at 500 km with calculated satellite trajectories using the phase gradient method with 1, 4 and 10 baseline data sets. (Note that antenna positions are not to scale and are purely for orientation purposes).

The difference between this phase gradient and the one produced from radar data can be put into a least square error fitting program to find which trajectory angle ϕ satisfies the data best. The equation for error in this case was calculated by:

$$\text{Error}_{\phi} = \varepsilon(\bigtriangledown\phi_{bl,\phi,\text{Real}} - \bigtriangledown\phi_{bl,\phi,\text{Calc}})^2 \tag{4.9}$$

The resultant angle is dependent on the number of baselines and the accuracy of these data sets. If the data used for an analysis have low noise and there is no constant phase then the result will deteriorate rather than improve by adding more data. However, with the majority of satellite passes all five EASI antennas have good signal and ten of the resulting baselines show consistent phase change through time after processing. In these conditions adding more baselines improves the accuracy of the results, as can be seen in Figure 4.9, plotting the calculated trajectories using different numbers of baselines. It shows that adding more baselines removes the 2π ambiguities of using a single baseline and decreases errors due to noise, with the predicted peak positions matching the modelled best when the most baselines are used.

As with the power peak method, any errors in the initial satellite velocity values will manifest themselves as a constant error and so should not affect the error fitting process. Again, once an

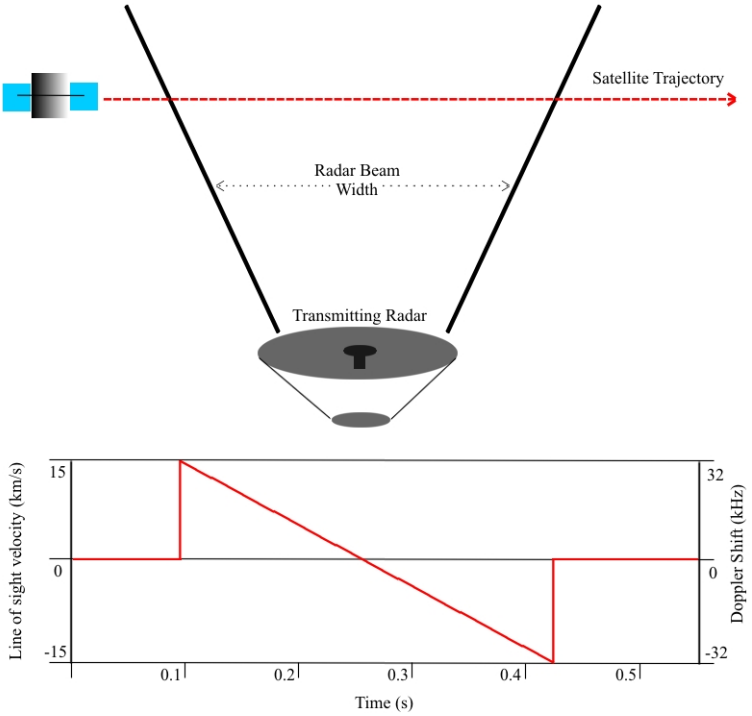

Figure 4.10: Diagram of frequency shift in coherent data for an object passing over a vertically aligned radar.

ideal trajectory angle has been found which fits all baseline data best, the LSF program can be run again with the velocity as a variable to calculate this value for a given satellite pass.

4.2.4 Frequency Tracking of the Satellite

Although the ESR radar system can only transmit at one frequency at a time, the reflected signals received back from an object are usually spread over a wide frequency range. Satellites and other coherent reflectors exhibit spectrally discrete signatures due to their velocities and sizes. However, observations show that the frequency of peak reflected power of a satellite always increases with time as it progresses through the radar beam. The reasons for this frequency progression are the following:

1. Doppler shifting of the reflected signal will always mean as the satellite travels towards the radar beam it will go from the highest blue shifted state as it enters the beam to the most red shifted state as it leaves the beam, as can be seen in Figure 4.10.

2. If the radar beam is transmitted at an angle to the vertical (such as magnetic zenith aligned) this will also affect the observed frequency of the object. The extent by which the frequency is altered is dependent on the trajectory of the satellite relative to the angle of transmission. If the trajectory is in the same direction as the angle offset then this change in frequency will be

increased. Alternatively, if in the opposite direction this frequency change will decrease, as can be seen in Figure 4.11.

The line of sight (LOS) velocity of the satellite can be calculated by the perpendicular velocity vector of the satellite to the radar at any given point such that:

$$\mathrm{V_{LOS}} = \mathrm{V_{sat}} \cdot \tan(\theta_{\mathrm{Radar}_\perp}) \tag{4.10}$$

where $\theta_{\mathrm{Radar}_\perp}$ is the radar elevation angle.

The received frequency that changed due to this LOS velocity can be calculated from the transmission frequency by Doppler principles:

$$f_0 + \delta f = (1 + \frac{V_{\mathrm{LOS}}}{c}) \cdot f_0 \tag{4.11}$$

where δf is the frequency change, f_0 the transmission frequency, c the speed of light and $\mathrm{V_{LOS}}$ the line of sight velocity of the satellite in m/s.

As can be seen in Figure 4.11, the direction from which the satellite entered the angled radar beam greatly alters the pattern of the frequency shift over the transit of the satellite. The angle of transmission affects the gradient of frequency shift over time of the transit, and the direction of satellite trajectory determines the initial LOS velocity and frequency shift recorded. Figure 4.11 is an idealized image which shows the problem in only two dimensions.

If the frequency of the received signal is known to a high degree of accuracy, then the trajectory of the satellite can be determined for a radar beam which is offset from the vertical. Unfortunately, this is not possible with ESR data, as the frequency resolution is not high enough to detect accurately these subtle frequency changes in signal over a transit with gates usually of the order of every 100 kHz. However, this change in frequency has been roughly observed with satellite signals changing between adjacent frequency gates throughout a transit. The effects of this gate shifting has been subsequently accounted for in this analysis, and so data from multiple frequency gates were analysed for a single time, or alternatively gates were combined to give an accurate analysis.

4.3 Data Sensitivity and Error Testing

Any discrepancies in radar positions, phase offset values and transmission / reception frequencies will have an adverse effect when attempting ASI analysis. If the antenna positions are given in Cartesian coordinates of x, y, and Z, the most important of these is seen to be errors in antenna height (z) or systematic phase offsets which cause the same effect. The effect that all offsets may

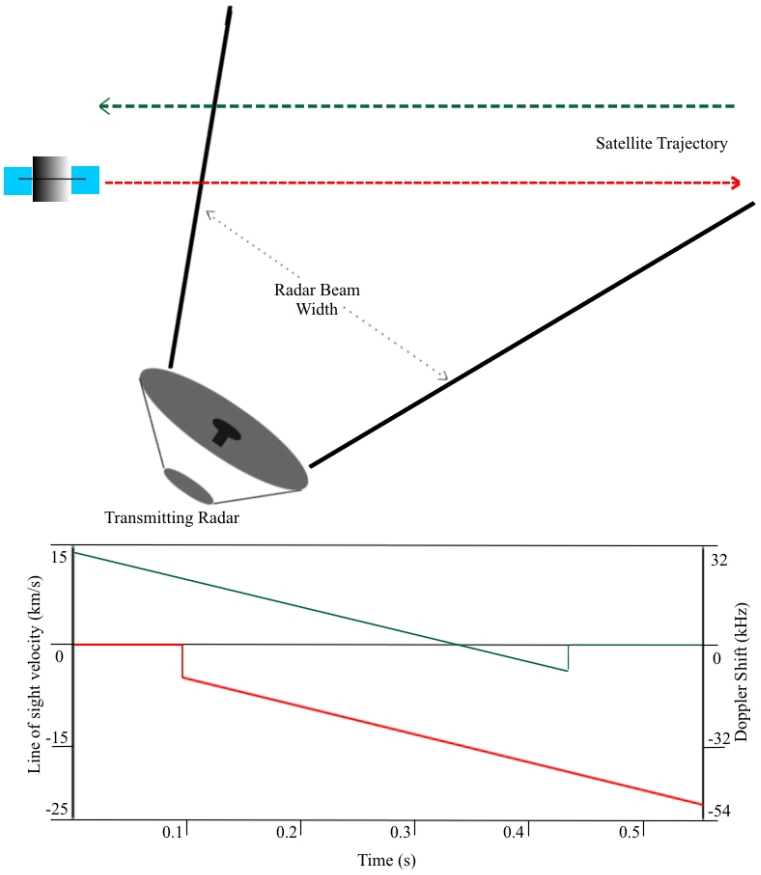

Figure 4.11: Diagram of frequency shift in coherent data for an object passing over radar beam at an angle to the vertical.

have on the results of the EASI system are examined here. This is done by modelling an ideal ASI image, and comparing it to a modelled image after an offset has been applied. The change of intensity in each pixel is calculated as a percentage and the average change over the entire image is produced.

4.3.1 Antenna Position Offset

For this analysis the images from the EASI antennas are modelled and the radar and object positions given in a Cartesian coordinate system of x, y and Z, where Z is the vertical direction or radar range direction (when not vertically aligned). The data are modelled for a single point source reflection at the centre of the imaging area directly above the antennas. The calculated errors are for a single antenna offset only. Therefore, these errors can accumulate for all five antennas, creating an overall large discrepancy in ASI brightness images.

The x direction is on the two-dimensional plane of the ground where the radars are situated. As can be seen in Figure 4.12 which plots image error with increasing offset, the error increases

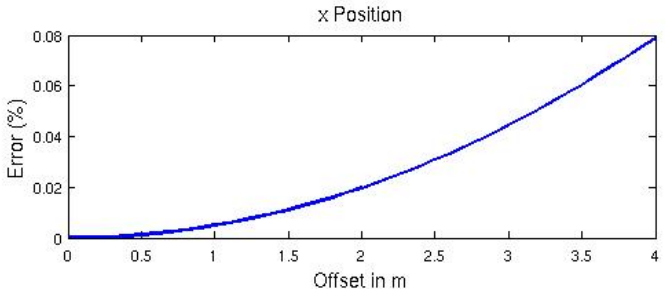

Figure 4.12: Graph error in ASI image with increasing x offset in m of one antenna.

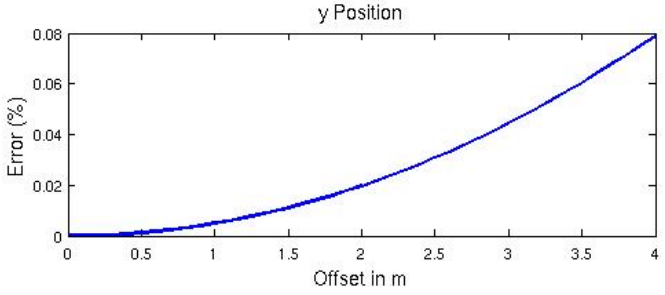

Figure 4.13: Graph error in ASI image with increasing y offset in m of one antenna.

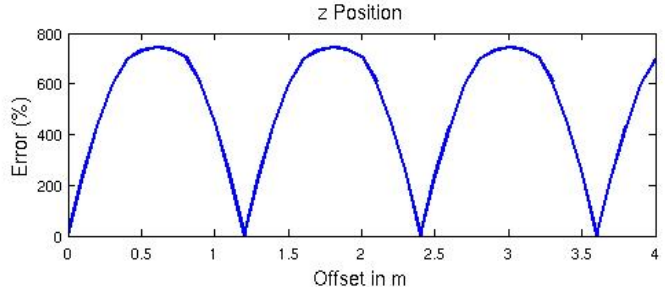

Figure 4.14: Graph error in ASI image with increasing z offset in m of one antenna.

exponentially with increasing offset. Therefore, small offsets in position will have very minor degrading effects on the resultant ASI brightness images, whereas larger offsets will have a much larger effect. However, in general the error caused by even an offset of 1 m is relatively small, with an offset of 4 m causing less than a 0.1% error.

The y direction is also on the two-dimensional plane of the ground where the radars are situated perpendicular to the x direction. As can be seen in Figure 4.13, the error increases in the same manner as in the x direction, doing so exponentially with increasing offset. Therefore, as with the x direction, small offsets in position will have very minor degrading effects on any resultant ASI brightness images, whereas larger offsets will have a much larger effect.

The Z direction is the vertical direction in altitude above the plane of the ground. This is the

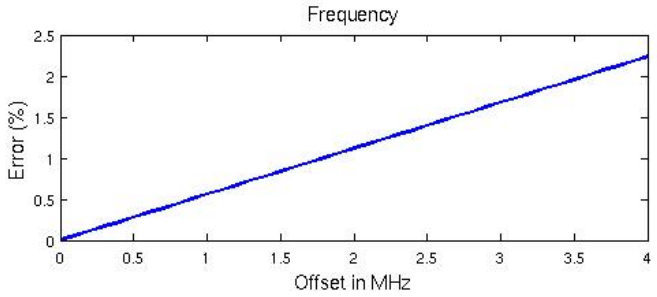

Figure 4.15: Graph error in ASI image with a transmission frequency offset.

same direction that the reflected signal is travelling. Therefore, any offset in this measurement will have a very large effect. An offsets of 2π phase in measurements ($\sim$120 cm for EASI) will produce no increases in error, and the maximum error will occur at π phase offset ($\sim$120 cm). This large Maxwellian error shape with Z offset can be seen in Figure 4.14. Although the error value looks and in some cases can be dramatic, in the majority of situations this offset merely causes a shift in the position of peak brightness in the image.

Inaccuracies in transmission frequencies can also affect the produced ASI images. However, unlike other offsets, this can increase the total error once only, as transmission ideally occurs on a single antenna, whereas positional errors can be possible with all five of the EASI antennas. It can be seen in Figure 4.15 that the error per MHz is approximately 25 times greater than that of an antenna position per m. However, any errors are likely to be of the order of kHz rather than MHz. Therefore, in comparison to position inaccuracies, unless the frequency is incorrect to a large degree (many MHz), this error will also be relatively small.

Inaccurate phase offsets of radar antennas can create large differences in resultant ASI brightness images, and this is by far the most significant factor of errors using this method. The mechanism of calibrating these initial phase offsets is the most important calibration step needed for ASI. Inaccuracies cause differences in the measured path distances between two antennas and therefore have exactly the same effect as a Z direction offset. In this case the error cycles from trough to trough ever 2 π radians, as this is analogous to the 1.2 m offset for the wavelength of the radar system (500 MHz) . Changes and errors in wavelength consistently shifted the position of the PSF in the image by up to 50 km for 1 MHz change at a range of 500 km.

4.4 EASI Calibration

Due to different lengths of cables, discrepancies in the electronic components, or a number of other possible reasons, the phases by the EASI antennas (and most other ASI radars) for an object that exhibits constant phase (such as a satellite) a full wavelengths distance away is not zero. Ideally, for accurate images these phases should be zero for such an object. Systematic

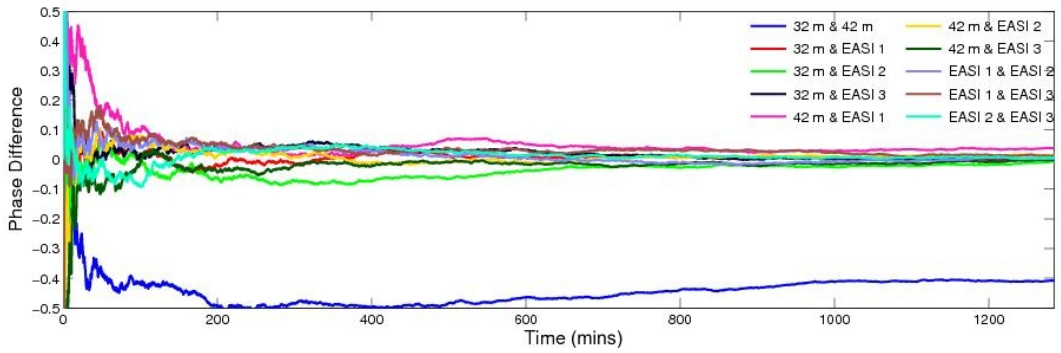

Figure 4.16: EASI phase offset calculation using incoherent backscatter over 20 hours of data.

phase offsets are a widely known problem in the radio astronomy community and a number of different techniques have been developed to calibrate antennas to compensate for them. Phase calibration of EASI is vitally important for this work as systematic phase offsets lower the calculated coherence of structures in antennas, hence giving false estimates of structure sizes and offsetting the calculated position of structure along the baseline being viewed. For ASI to be conducted, very accurate phase calibration needs to be completed. Therefore, the phase offset calibration between all five EASI antennas has been attempted using three different methods.

A new calibration method first suggested by Grydeland and La Hoz [2010] was developed using raw backscatter of the ionosphere during times with no auroral activity. With long enough integration times all scatter phases (which are random in nature) should cancel out to zero. Therefore, any remaining phase values after this integration are due to a constant systematic source. This method was attempted with the current 20 hours of LT4FL data available where no aurora was present. Figure 4.16 shows the calculated average phase values (which should tend towards the offset), for all five EASI antennas, with integrations of up to 20 hours of data. The calculated phase offset calibration values for the ESR 32 m and 42 m antennas started to stabilize at approximately -0.405 radians over the 20 hours of data. However, stable values were not produced for the EASI antennas. This is believed to be due to the much lower receiving powers of the EASI antennas. Therefore, usable phase offsets were not found within the available data integration time and much larger data sets would be needed to complete this analysis, which currently are not available. It is likely that future similar analyses with larger data sets would yield better results.

4.4.1 Satellite Phase Minimization by Total Least Square Error Fitting

Coherent point sources such as satellites should produce constant phases in all antennas when directly above the radars. Differences in side lobes and gain patterns between the antennas can affect this if the area of transmission is large enough. However, as shown in section A.1.0.1

the transmission area of the 42 m antenna as used for the LT4 and Beata experiments is small enough to limit this effect, rendering the above assumptions valid. Due to this small transmission area, the majority of satellite signatures seen in all five of the EASI antennas will be near or passing through the centre of the radar beam. Therefore, most of the satellite transits should appear with constant phase at some point during the transit. A minimum total least square error (MLSE) function of phases was conducted on many satellite transits to calculate relative systematic phase differences between antennas. By entering all five antenna phase offsets as unknowns to be solved, using measured phase values during the transits, a number of systematic offsets should arise with the MLSE method. These calculated values should be the phase offsets for the individual antennas, provided the satellites are near the centre of the radar beam.

Twenty one direct satellite passes over the EASI radar site were recorded between September 2010 and March 2012. Using the recorded phase values for these passes, average phase offsets were calculated. Results with low signal to noise have been omitted. The resulting average phase offsets throughout all passes are given in Table 4.4.1. These fitting results have a standard deviation of 0.1 radians.

Antenna	42m	32m	EASI 1	EASI 2	EASI 3
Average Phase Offset (rads.)	0.8	1.3	1.3	0.9	0.4

4.4.2 Satellite Phase Minimization with Optical Signatures

The process of combining satellite data with optical camera data for the EASI system was undertaken by Schlatter et al. [2012]. In this work the ASK and Odin camera systems were used to pinpoint the satellites' positions accurately at time scales of 20 Hz throughout a transit, similar to the work undertaken by Sullivan [2008]. The Odin instrument was the predecessor of ASK and included a single filtered camera also co-located at the ESR, with a $14.3^\circ \times 10.9^\circ$ FOV. The optically observed satellite positions were entered into a computational program, with the radar data, to give positions where the power peaks of the generated ASI brightness-images should be centred. The phase offsets required to produce these images was then computed in an LSF method. Schlatter et al. [2012] was able to improve the accuracy of calculated phase offsets using this method. An accurate phase offset for the 32 m and 42 m antennas was published as 0.29 radians, and the offset between the 42 m and EASI A antenna as 0.43 radians. The same process is being tested with all five EASI antennas, but accurate phase estimates have not yet been verified or published. This is due to fewer data sets of satellite passes with optical data being available with all five EASI antennas operating, owing to their limited time of operation. Further data sets need to be added to verify and improve the accuracy of these results in future.

Chapter 5

Upper Atmospheric Thermal Losses and 'Weak' NEIAL Studies

During the first two years of this work the EASI radar system was undergoing calibration and troubleshooting and so no NEIAL events were recorded. It was therefore decided to undertake a study of past radar data sets known to contain NEIALs.

Many of the current NEIAL production theories suggest that small ion-line enhancements are possible as well as the well-documented large enhancements, ranging to 5 orders of magnitude in power above thermal ionospheric conditions. Although statistical studies on strong NEIAL events have been done in past literature, such as Ogawa et al. [2011], with some using raw data from from both the 32 and 42 m ESR antennas for interferometry [Grydeland et al., 2005], a study to see if and when low spectral power NEIAL events have occurred has not been undertaken. In these past studies, strict high power definition criteria have always been used so that false positives were eliminated. This means that possible 'weak' NEIALs, which should exist in theory, although possibly present in the data, have not yet been analysed.

This work attempts to find if and when these weak NEIALs may be occurring and study the conditions surrounding them. Due to their inherent weak nature, an enhanced spectrum may be indistinguishable by eye from that of a thermal spectrum under high-energy electron precipitation. Therefore, a method is described in Section 5.1 to calculate atmospheric parameters from these spectra and to distinguish between thermal and non-thermal enhancements. The method focuses on the fact that non-thermal temperature enhancements can abate at a much quicker rate than thermal reactions will allow. Four previously observed NEIAL events along with two events observed with EASI in 2012 are analysed in this section using the new method. However, before this analysis can be undertaken, a complete understanding of what thermal reactions occur throughout the atmosphere is needed to calculate potential thermal loss rates. These atmospheric reactions are summarized below and described in detail in Appendix B.

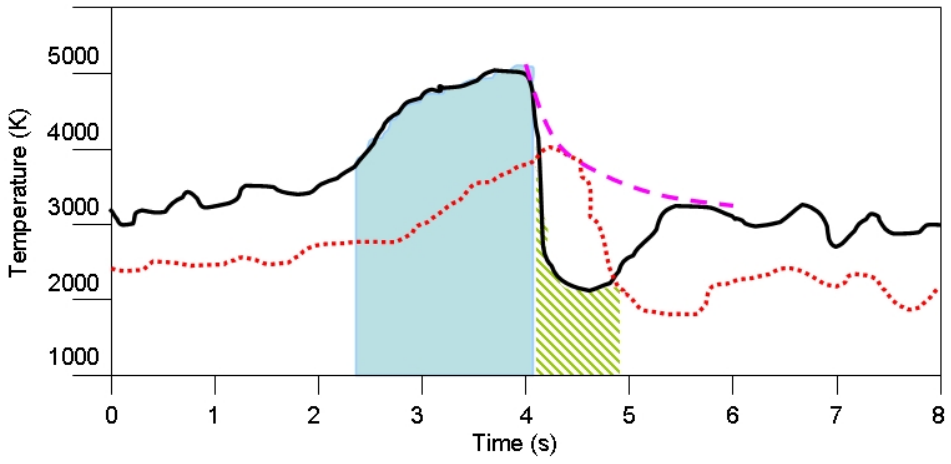

Figure 5.1: Diagram of a non-thermal enhancement and drop in electron temperature, showing recorded temperature (black), temperature value from one second in the past minus the maximum thermal losses (red), and a typical thermal loss rate (magenta). Non-thermal enhancement occurs in the blue region with the detection made in the green striped region.

5.1 NEIAL Classification and Thresholds

By re-examining past raw and processed data known to contain NEIALs, it was theorised by Gustavsson and Goodbody (first documented in this thesis), that times and height bins exhibiting non-thermal but processable temperature changes could be determined, and so find indications of when 'weak' NEIALs exist.

A diagram of this process can be seen in Figure 5.1. Enhancement occurs during the blue region, but it is not currently possible to differentiate between thermal and weak non-thermal enhancements. Therefore, it is only in the temperature loss regions (green striped) that the detection of a non thermal enhancement can be made. In this diagram a typical thermal loss response is shown (magenta dashed line) as well as the temperature values from the previous second minus the maximum loss rate. As can be seen, the temperature drops by a much greater value than these two between 4 and 5 seconds. It is at these time steps that the signature of a weak non thermal enhancements would be detected.

Radar data is not continuous and is integrated into time steps of between 2 and 10 seconds in length. Therefore, successive time steps where changes in electron or ion temperature exceed those expected from thermal losses over the integration time step are taken as the signatures of non-thermal temperature drops such that:

$$\delta \mathrm{T} > \mathrm{L}_{\mathrm{Tmax}} \tag{5.1}$$

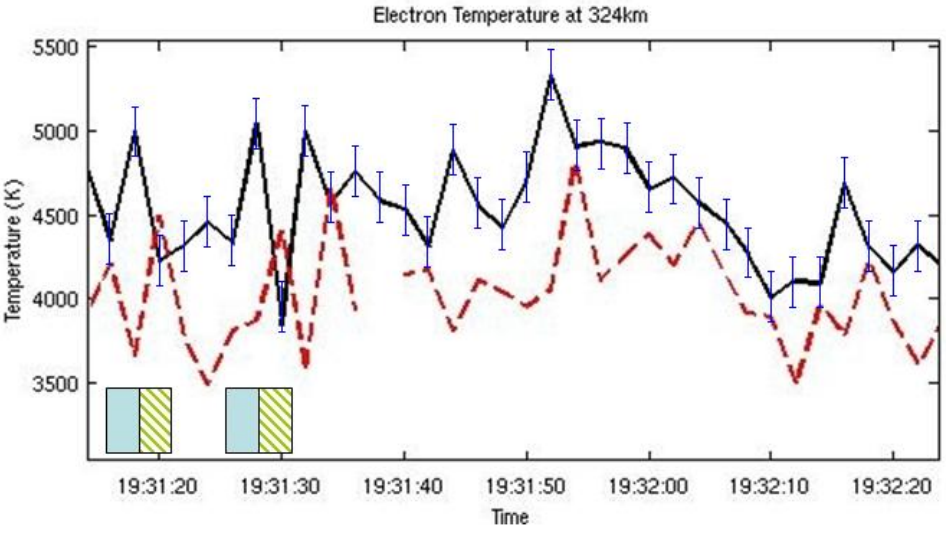

Figure 5.2: Plot of calculated electron temperature (black) and temperature of previous time step with maximum thermal loss (red). Time steps where non-thermal losses are detected are marked with a green dashed box, and time steps with non thermal enhancements marked with a solid blue box.

Date	Time (UT)	Data Format	Source
24/01/1998	06:00	gup0 10 s	Sedgemore-Schultess et al.
26/01/2003	06:56	lt1hl $\leq$0.2 s	Grydeland et al.
22/01/2012	08:30	IPY 6 s	EISCAT
24/01/2012	19:32	lt4fl $\leq$0.2 s	Goodbody et al.
23/02/2012	22:30	Beata 6 s	Tuttle et al.
27/03/2012	10:23	lt4fl $\leq$0.2 s	Belyey et al.

Table 5.1: Table of NEIAL events used in this analysis.

In this case, the previous time step is indicated as being non thermally enhanced. This can been see in Figure 5.2, which shows approximately two minutes of measured electron temperature on 24 January 2012 at 324 km altitude. Changes in temperature that exceed those possible by thermal losses are observed at two points in the data, these are underlined by green dashed boxes. The time steps where weak non thermal enhancement occurred are underlined with blue boxes.

To determine if these non-thermal losses and enhancements occurred during NEIAL events a number of new and past radar data sets were analysed. The dates and experiments from which NEIAL data were re-analysed for the present work can be seen in **??**.

Before the radar data could be analysed, the maximum potential thermal losses were calculated. This process is described in Appendix B. In addition to this step, the atmospheric parameters (such as electron and ion temperature) need to be derived from the raw data spectra. This process is explained below.

5.2 Estimating Ionospheric Parameters from IS Spectra

To examine electron and ion temperature evolution during a NEIAL event using radar spectra (particularly raw data), these parameters are derived by fitting the spectral shape for each height gate and time step in the data. Spectral fitting can be conducted to determine the values of ion/electron temperatures, masses, velocities, densities, collision frequencies, radar central frequencies and partition fractions for the radar signal. For usual EISCAT experiments the spectra are analysed with the Grand Unified Incoherent Scatter Data Analysis Program (GUISDAP), as described by Lehtinen and Asko [1996]. However, the raw data experiments (such as LT4) used in a large portion of this work (see Chapter 6) cannot currently be run by GUISDAP, and so another method had to be used.

A program was developed by the author to analyse the parameters of these raw data experiments in a similar method to GUISDAP (see Section 1.4.3).

As the signal to noise ratio for IS is very low, the data must first be integrated to produce usable spectra. It was chosen to integrate for 2.0 s, as this produces reasonable spectra for a majority of the time, and is the predicted order of lifetime for NEIALs. Due to the low integration time, however, the results will encounter inaccuracies at very low and very high altitudes. Fortunately, NEIALs usually occur within the altitude bands of reliable accuracy.

For normal auroral activity, IS backscatter spectra that are integrated for a long enough time (typically 4 - 10 s) give a shape similar to a symmetrically centred double-Gaussian. An example of this spectrum is seen in Figure 5.3, which shows how the shape varies under different atmospheric conditions. Therefore, plasma parameters in the atmosphere can be calculated by analysing the shape of an observed spectrum, as described in Section 1.4.

NEIALs (especially those with large reflective powers) do not exhibit similar spectral features to thermal excitation and produce abnormal plasma activity. Their spectral signature includes one or both of the ion acoustic shoulders being enhanced. This means that spectral fitting for strong NEIAL events cannot be conducted, as the calculated atmospheric products will be unphysical. In this analysis the data from these periods is ignored so that highly unphysical data points do not affect the weak NEIAL detection method and contaminate the end results. Smaller enhancements, however, may not influence the spectra greatly and produce credible but inaccurate reading. The aim of this analysis is to find times and altitudes where spectra which can be fitted to a model, and which are mildly enhanced, but non thermal behaviour is detected. The process is applied to data sets already analysed for NEIALs.

5.2.0.1 Zero Frequency Shift and Splitting

Due to the lower integration time of the raw radar spectra (2 s compared to 6 s), the spectra may not be centrally aligned. To produce accurate parameters from these low-time integration

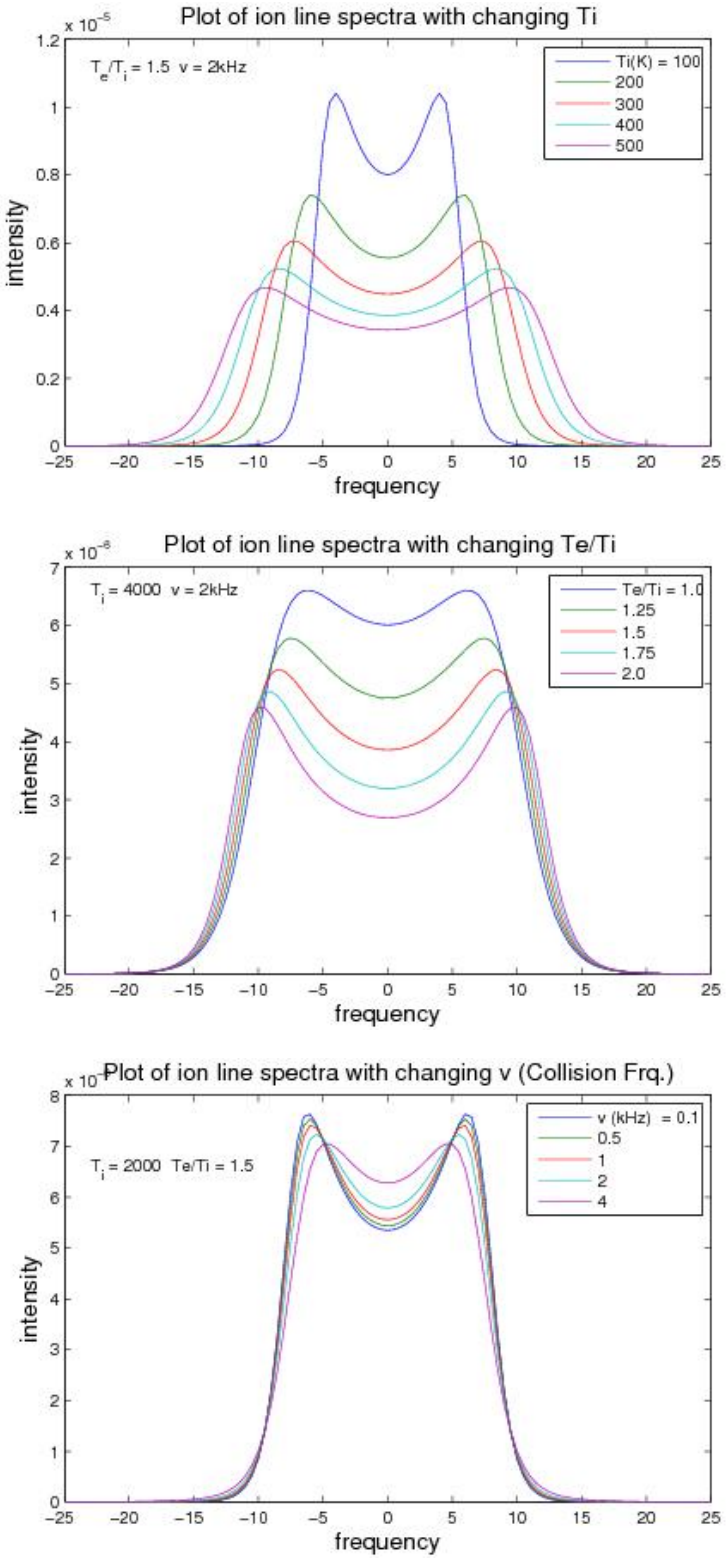

Figure 5.3: Ion acoustic line shape dependence on plasma parameters.

off-centred spectra, each spectrum must first be centred around the transmitting frequency of the radar. This can be done by finding the frequency difference between the two peaks with respect to zero frequency and shifting this entire spectrum by half this difference. This shift is due to Doppler effects caused by plasma velocities in the direction of the radar beam. Therefore, this calculated frequency shift can be used as an approximate velocity of ions in the direction of the radar FOV. For zenith aligned observations this is the ion velocity along the magnetic field line. This measurement can be used to determine whether significant ion outflow events are occuring. The velocity is calculated from the frequency shift, using the equation:

$$\delta\nu = \nu - \nu_0 = 2\frac{\upsilon}{\lambda_0} \tag{5.2}$$

where υ is the velocity in m/s, $\delta\nu$ the frequency offset from centre in Hz and λ_0 the radar frequency.

The spectrum, once centred, can be split into two halves. Each half can be mirrored and combined with this mirror image to create a full double hump spectrum. These two symmetrized spectra can then be analysed separately, and depending on their validity, either one or an average of the two used for the end product for the height gate and time being derived. This can be seen in Figure 5.4 where an uneven spectrum is observed (middle) and fitted. This spectrum is centred, symmetrized and an average of the two split spectra found (top panel).

5.2.0.2 Least Square Error Fitting

Ionospheric parameters are inferred in ratios from the shape of the Gaussian spectra. Any change in one of these parameters can alter the shape of the Gaussian curves in a number of ways (see Figure 5.3). In this work a spectral shape fitting program was used in conjunction with a least squares error fitting program to converge on parameters that fit the observed spectral shapes best. The parameters that are input to the model spectra are: transmission frequency (ω_0) in Hz, Doppler shift (ω) in Hz, electron density (N_e) in m^{-3}, temperature (T_e) in kelvin, ion temperature (T_i) in kelvin, average ion mass (m_i) in atomic mass units, and electron (ν_e) and ion (ν_i) collision frequencies. The spectral shape of the ion acoustic lines can be calculated by the spectral density function as described by Guio et al. [1998] as:

$$\begin{aligned}\mathrm{S}(k,\omega) = &\left|1 + \frac{\mathrm{C}_e(k,\omega)}{\mathrm{D}(k,\omega)}\right|^2 \frac{\mathrm{Im}\mathrm{P}_e(k,\omega) - \nu_e|\mathrm{P}_e(l,\omega)|^2}{\sqrt{\pi}|\mathrm{X}_e(k,\omega)|^2} \\ &+ \sum_j \frac{N_j}{N_e} z_j^2 \left|\frac{\mathrm{C}_e(k,\omega)}{\mathrm{D}(k,\omega)}\right|^2 \cdot \frac{\mathrm{Im}\mathrm{P}_j(k,\omega) - \nu_i|\mathrm{P}_j(k,\omega)|^2}{\sqrt{\pi}|\mathrm{X}_j(k,\omega)|^2}\end{aligned} \tag{5.3}$$

with

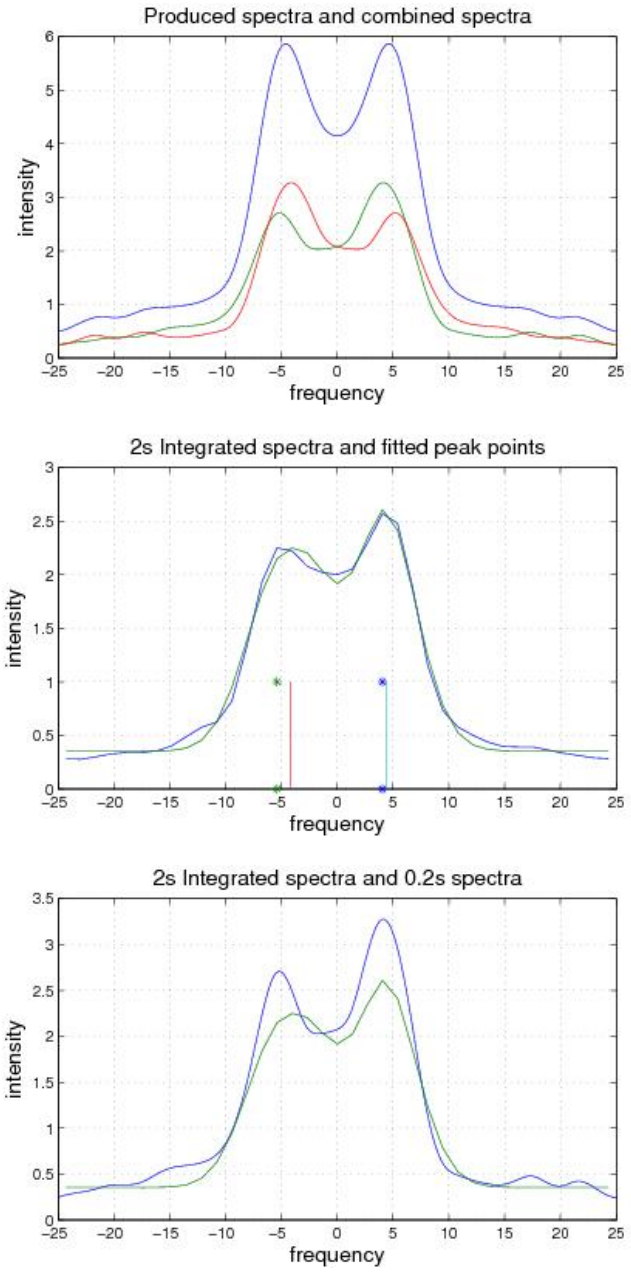

Figure 5.4: Top panel: Resultant spectra (x2) to be fitted (blue) and original and flipped original (red and green). Middle panel: 2 s integrated data spectra (blue), fitted Gaussians (green), initial peak estimates (*) and Gaussian peak (lines). Bottom panel: Fitted Gaussian spectra (green) and 0.2 s spectra centred from peak calculations (blue).

$$\mathrm{D}(k,\omega) = 1 - \sum_{\alpha} \mathrm{C}_{\alpha}(k,\omega) \tag{5.4}$$

$$\mathrm{C}_{\alpha}(k,\omega) = \mathrm{Z}_{\alpha}(k,\omega)/\mathrm{X}_{\alpha}(k,\omega) \tag{5.5}$$

$$\mathrm{X}_{\alpha}(k,\omega) = 1 + i\nu_{\alpha}\mathrm{P}_{\alpha}(k,\omega) \tag{5.6}$$

$$\mathrm{Z}_{\alpha}(k,\omega) = \sum_{k} \mathrm{Z}_{\alpha,k}(k,\omega) \tag{5.7}$$

$$\mathrm{Z}_{\alpha,k}(k,\omega) = \frac{\omega_{\alpha,k}^2}{k^2} \int_{\mathrm{L}} \frac{k \cdot \bigtriangledown_{\upsilon} \hat{f}_{\alpha,k}(\upsilon)}{k \cdot \upsilon - \omega - i\nu_{\alpha}} d^3\upsilon \tag{5.8}$$

$$\mathrm{P}_{\alpha}(k,\omega) = \frac{1}{n_{\alpha}} \sum_{k} n_{\alpha,k} \int_{\mathrm{L}} \frac{f_{\alpha,k}\upsilon}{k \cdot \upsilon - \omega - i\nu_{\alpha}} d^3\upsilon \tag{5.9}$$

where $\hat{f}_{\alpha,k} = f_{\alpha,k}/n_{\alpha,k}$ denotes the velocity probability distribution function for the k^{th} component of the particular species α (e for electrons and j for ions), ν_{α} is the collision frequency of the particular species α, $r_0^2 = e^2/(4\pi\epsilon_0 m_e c^2)$ is the electron radius, n is the unit vector pointing from the scattering volume to the receiving radar, and p is the unit polarization vector of incident radiation; ω is the frequency shift between the transmitted radio wave, ω_0 and the received frequency ω_r, and k is the wave vector shift defined as the difference between the returned wave vector and the transmitted radio-wave vector k_0.

The resultant radio and wave vector can be calculated from the radio and object vectors, by the equations:

$$\omega = \omega_r - \omega_0 \tag{5.10}$$

and

$$k = \frac{\omega_r}{c} n - k_0 \tag{5.11}$$

with the transmitted radio-wave vector k_0 given by:

$$k_0 = \frac{2\pi\omega_0}{c} \tag{5.12}$$

In this work, the process was run with the average ion mass being input for the ionosphere at a given altitude instead of summing contributions from all species separately. This data was extracted from the IRI model and was done to reduce the computing time for each calculation. Although the ion composition of the atmospheres varies with time and altitude, particularly at a local level, this method should remain valid for the large ranges and relatively short timescales (¡10 s) used in this analysis. The program used an inbuilt Matlab error finding algorithm

to iterate values such that the errors produced by the error fitting equation were reduced to minimum. The error value of each estimate was calculated by the equation:

$$\text{Error} = \overrightarrow{\lim}\, 0(\mathrm{F}_{\mathrm{S}(k,\omega)}(\omega, \omega_0, n_e, \mathrm{T}_e, \mathrm{T}_i, m_i, \nu_e, \nu_i) - \mathrm{S})^2 \tag{5.13}$$

where S is the observed ion line spectrum.

If the error is too large then the program has not been able to fit to the data properly and so cannot be used. The causes for this are either that the data spectrum is unphysical due to noise, or a large NEIAL enhancement has occurred at this data point.

5.2.1 Collision Frequency Calculations

Any parameters that are already known will greatly increase the accuracy of the fitting process and greatly reduce the computational complexity of the calculations. Two such parameters are the electron and ion collision frequencies at each height gate.

The collision frequencies for a given species at a specific altitude can be calculated if the atmospheric species density and temperature are known. These parameters were extracted from the MSIS-E-90 and IRI atmospheric models for the times that the events occurred. The MSIS model data extracted provides neutral species densities and temperatures for all height ranges between 90 and 500 km. The IRI model data was extracted to provide ionospheric species densities for the same height range. The temperature of these was assumed to be the same as those of the neutral species. This is due to ion density being much lower than that of neutrals, causing temperatures to become thermal on average due to collisions between the species.

There are two main types of charge loss through collisions, one involving ions and the other involving electrons.

5.2.1.1 Electron Collision Rate

As described in Section 1.2, the electron collision frequencies are caused by collisions with both neutrals and ions. The total electron collision frequency is simply the sum of these two factors. These two types of electron collision are caused by different reactions and so must be calculated separately. Within these two regimes, each species has its own cross section and so collision factor. These must also be calculated separately. The electron neutral collision rates for the main constituents of the ionosphere have been calculated by Kero et al. [2007] as:

$$\nu_{e,\mathrm{N_2}} = 2.33 \times 10^{-17} \cdot n_{\mathrm{N_2}} \cdot (1 - 1.20 \times 10^{-4} \cdot \mathrm{T}_e) \cdot \mathrm{T}_e \quad (5.14)$$

$$\nu_{e,\mathrm{O_2}} = 1.82 \times 10^{-16} \cdot n_{\mathrm{O_2}} \cdot (1 + 3.60 \times 10^{-2} \cdot \sqrt{\mathrm{T}_e}) \cdot \sqrt{\mathrm{T}_e} \quad (5.15)$$

$$\nu_{e,\mathrm{O}} = 8.20 \times 10^{-16} \cdot n_{\mathrm{O}} \cdot (1 + 5.70 \times 10^{-4} \cdot \mathrm{T}_e) \cdot \sqrt{\mathrm{T}_e} \quad (5.16)$$

$$\nu_{e,\mathrm{H}} = 4.50 \times 10^{-15} \cdot n_{\mathrm{H}} \cdot (1 - 1.35 \times 10^{-4} \cdot \mathrm{T}_e) \cdot \sqrt{\mathrm{T}_e} \quad (5.17)$$

$$\nu_{e,\mathrm{He}} = 4.60 \times 10^{-16} \cdot n_{\mathrm{He}} \cdot \sqrt{\mathrm{T}_e} \quad (5.18)$$

where T_e is the electron temperature, and $\mathrm{n_X}$ the density of the neutral species at the required height gate.

The total collision contribution from neutral species is given by the sum of the values from all species. For the upper atmosphere it can be estimated to be the sum of the above parts and so is:

$$\nu_{e,n} = \nu_{e,\mathrm{N_2}} + \nu_{e,\mathrm{O_2}} + \nu_{e,\mathrm{O}} + \nu_{e,\mathrm{H}} + \nu_{e,\mathrm{He}} \quad (5.19)$$

The electron collision contributions due to ions is more complex. These were modelled successfully by Itikawa [1971] The equation for electron ion collisions was given initially by Chapman and Cowling [1952] as:

$$\nu_{e,i} = \frac{4\sqrt{2\pi}}{3} N_i \left(\frac{q_e^2}{k_B \mathrm{T}_e}\right)^2 \left(\frac{k_B \mathrm{T}_e}{m_e}\right) \ln\Lambda \quad (5.20)$$

where N_i is the total ion density given by $n_i = n_{\mathrm{O^+}} + n_{\mathrm{O_2^+}} + n_{\mathrm{H^+}} + n_{\mathrm{He^+}}$ and q_e is the charge of the ions calculated by: $q_e = 1.6 \times 10^{-19}/\sqrt{4\pi\epsilon_0}$. ln Λ is the 'Coulomb logarithm', which was calculated by Itikawa [1963].

As stated above, this electron-ion collision rate has to be added to the electron-neutral rate to produce an overall electron collision rate for a given altitude. Once calculated, the data can be added to the above ion acoustic line spectral fitting program to help produce accurate fits for atmospheric parameters.

5.2.1.2 Ion Collision Rate

Under almost all conditions, ion temperatures are below those of electrons in the upper atmosphere, and so the dominant source of energy loss through collisions for ions is with neutrals, in particular O, $\mathrm{O^+}$ and $\mathrm{N_2}$. Therefore, these are the only sources considered for this region in this work. The formula for calculating the collision rates is shown by Kunitake and Schlegel [1991] as:

$$\nu_{i,n} = 2.44 \times 10^{-16} \cdot n_{\mathrm{O}} + 4.28 \times 10^{-16} \cdot n_{\mathrm{O}_2} + 4.34 \times 10^{-16} \cdot n_{\mathrm{N}_2} \tag{5.21}$$

where n_X is the the density of species X at a given altitude.

This factor can be calculated independently for each height gate and date, providing the correct temperatures and densities are known, and in turn the results were entered into the spectral fitting program to fit parameters to a recorded ion acoustic line spectral shape.

5.3 Data Analysis and Results

Multiple events from past and current data known to contain NEIALs have be analysed to find electron and ion temperatures and their variation through time. Each height gate for every time step for all events has been calculated separately based upon the recorded ion line spectra.

5.3.1 Thermal Loss Comparison

The change in calculated electron and ion temperatures from one time step to the next is examined in detail here. The maximum thermal losses were calculated as described in Appendix B. Data from the MSIS-E-90 and IRI atmospheric models were used as input to calculate the maximum possible thermal losses in temperature for all time steps and altitudes used in the data. For the dates, times, altitudes and locations of events examined in this section, these two models produce the most accurate atmospheric data available. However, it is important to note that the accuracy of these two models is limited by their time and height resolutions. The height resolutions of the two models are greater than that of the measurements and so can be mitigated as a limiting factor in the study.

The most important limitation is in the time resolution of the models. Both models produce outputs averaged over an hour period. However, atmospheric conditions (ion and neutral, but in particular ion parameters such as density) can change greatly over this time, especially during local dawn and dusk hours. In this study, measurements from time integrations as low as 2 seconds are used. A consequence of this may be that a number of the calculated maximum possible temperature losses are underestimated, giving rise to false positive detections. A small variation in a single atmospheric parameter is unlikely to greatly change the loss rate for a set altitude. However, if multiple atmospheric parameters were to change by a large degree, then the loss rates could be changed in a non trivial manor. To counteract this, it was chosen to only use significant drops in temperature that were at least 1.5 times greater than those calculated to be physically possible from the model data, and above a set minimum temperature change. In this analysis a minimum temperature change of 120 K was set, as this value is twice the thermal maximum measured noise value of the ESR 32 m radar (which had the largest noise of the two

radar dishes). By doing this, any false detections caused by noise should be mitigated. This temperature variation is also significant by atmospheric standards and should be greater than any changes in neutral temperature over the period which the data is integrated (2-10 s). Losses that exceed both of these criteria will be larger than all but the most extreme variation in loss rates from the hour average as well as greatly exceed the noise level of the measurement, and so are highly likely to have been caused by non-thermal effects.

An additional factor to consider is that these are both global models produced from a limited number of input measurements and so may not account for local atmospheric variations. That said, the height ranges used in this analysis (3-50 km) are sufficiently large that local neutral temperature variations should not greatly effect the results due to integration over these ranges. Therefore, use of the global models is valid for these datasets.

The calculated electron and ion temperature loss rates were adjusted from per second to the resolution of the radar data of each event to determine the maximum possible loss within the time resolution, such that:

$$\delta \mathrm{T}_{r,\max} = \delta \mathrm{T}_{\mathrm{L}}(\mathrm{s}) \cdot \mathrm{t}_r \tag{5.22}$$

where T is electron/ion temperature in kelvin, and t_r is radar resolution time is s.

The spectrally fitted temperatures at each time step were compared to those of the same altitude at one time step later. If the temperature change was greater than that of the maximum calculated loss over the radar time resolution (δ $\mathrm{T}_{\mathrm{radar,max}}$), then the data set is flagged as being thermally unphysical.

NEIALs have been extensively found to span large altitude ranges. Therefore, any enhancements caused by NEIAL excitation processes should appear in multiple adjacent height bins. The created analysis program determines whether multiple height ranges (5 consecutive) have been flagged for thermally unphysical temperature drops in either ion of electron temperature. If this is the case then these data points are highlighted as weak NEIAL-like signatures. The conditions for this were if five consecutive height bins contain ion or electron temperature drops greater than 1.5 times the maximum temperature loss possible through thermal processes, where this drop in temperature is over 120 K. Although due to its stringency this may eliminate many existing weak NEIAL signatures, it was chosen to reduce any error due to noise and low signal and so ensure only real events are highlighted.

As stated above, extremely enhanced spectra will not be fitted by the spectral fitted program and so data from these times and height gates will be discarded. If multiple height gates cannot be fitted, then it is likely that large NEIALs are the cause, as noise contribution is usually random in nature. For these times it is likely that the NEIAL enhancements will be easily identifiable by eye. Likewise, the program will not be able to fit non-Maxwellian spectra. However, it is likely

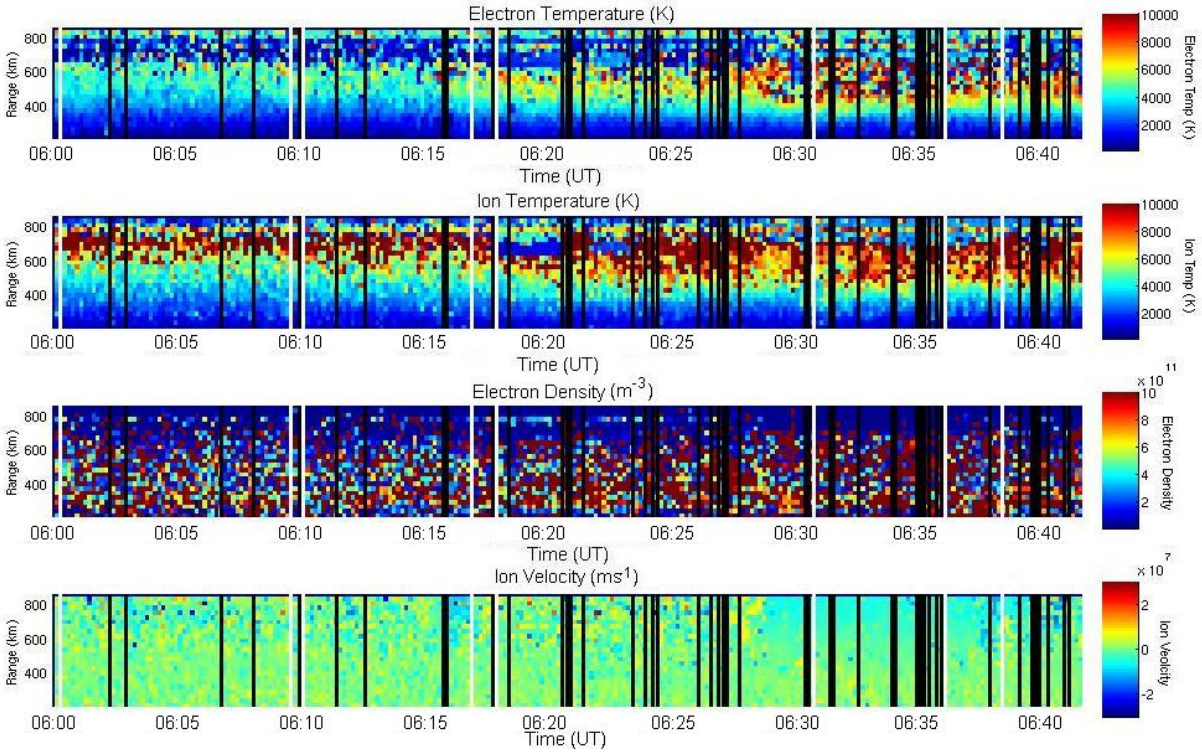

Figure 5.5: Ionospheric parameters plot for 24 January 1998 at 06:00 - 06:50 UT run with the gup0 experiment through time, showing electron density (top), ion temperature (2nd), electron temperature (3rd) and calculated LOS ion velocity (bottom). Times where non-thermal enhancements have been flagged are marked by white lines, and strong NEIAL signatures are marked by black lines.

that altitude ranges consistently exhibiting with these features will be limited (only occur within one height gate) , due to being caused by local conditions, and so should not be identified as NEIALs.

5.3.2 Results

In all the six data sets examined in this work, strong NEIALs are known to have occurred. The electron density (m^{-3}), electtron temperature (K), ion temperatures (K) and ion LOS velocity (where available) have been plotted throughout the duration of these data sets, as can be seen in Figures 5.5, 5.6, 5.7, 5.8, 5.9, 5.10 and 5.11. These all show the calculated electron temperature (top), ion temperature (row 2) and electron density (row3), with data from raw products also showing ion line-of-sight velocity (bottom), from fitting the spectra through time. Auroral activity is usually accompanied by increases in electron and/or ion densities and temperatures. Ion outflow and inflow events within the radar FOV are observed by large line-of-sight ion velocities. If the ionosphere were to be greatly enhanced by a non thermal enhancement then this would likely manifest itself as a sudden large increase in electron and ion temperatures at the

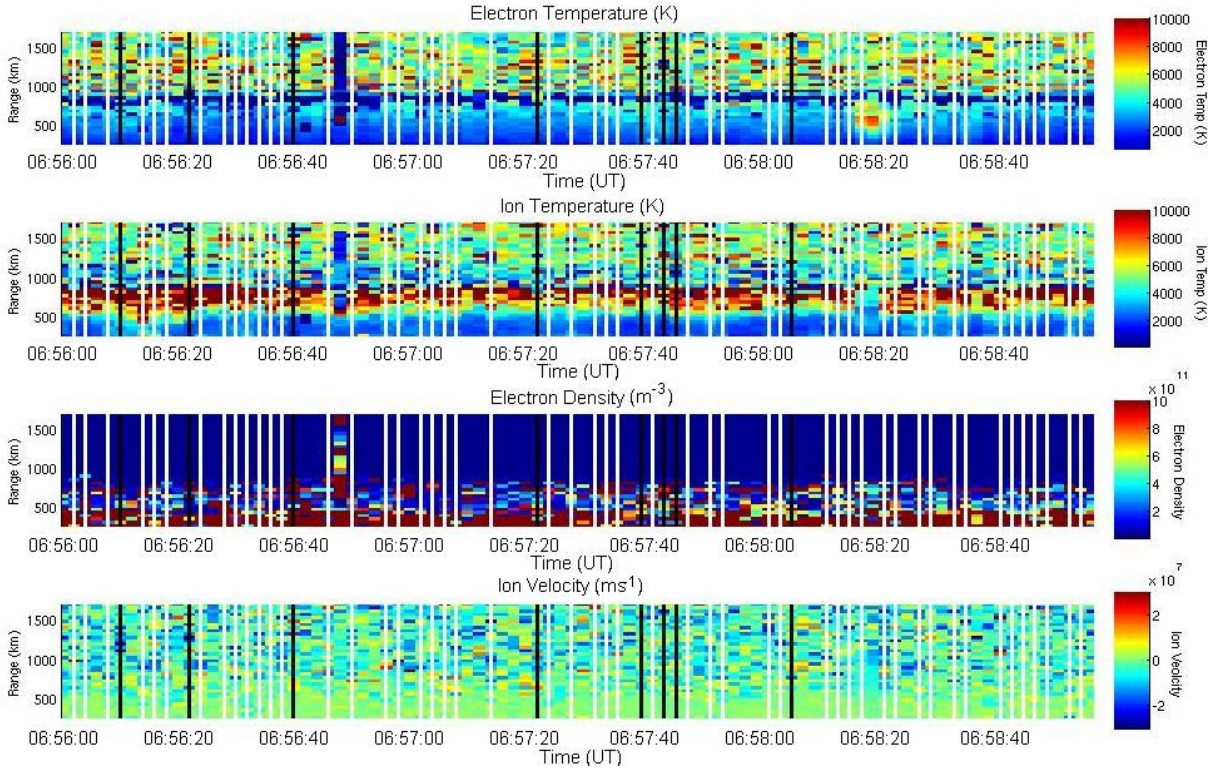

Figure 5.6: Ionospheric parameters plot for 26 January 2003 at 06:56 - 06:59 UT run with the LT1 experiment through time, showing electron density (top), ion temperature (2nd), electron temperature (3rd) and calculated LOS ion velocity (bottom). Times where non-thermal enhancements have been flagged are marked by white lines, and strong NEIAL signatures are marked by black lines.

affected altitudes. NEIALs often occur at altitudes above peak thermal enhancements, meaning that affected altitudes will likely be visible above those caused by thermal enhancements.

The data plots show times of between ∼3 and 60 minutes in length, with the data from the 22/01/2012 event (see Figures 5.7, 5.8) were taken over two hours due to the strong NEIAL event occurring close to the mid point between these two datasets. During all events, times were found where spectra could not be fitted, where there were non-physical measurements over multiple heights. These time steps matched directly with the known observation times of large spectral enhancements (NEIALs) observed by the original authors. These time steps are highlighted with black lines. The analysis also highlighted a number of possible 'weak' NEIAL enhancements surrounding each event, where the spectra received did not appear to be significantly enhanced, but the calculated drop in temperatures from the spectral fitting was much greater than that possible under thermal conditions.

Figure 5.5 shows data taken with the gup0 experiment at 10 s resolution. The results show that over the 45 minutes of the event a large number of strong NEIALs were detected. The majority of these times coincided with enhanced electron and ion temperature and electron density, but

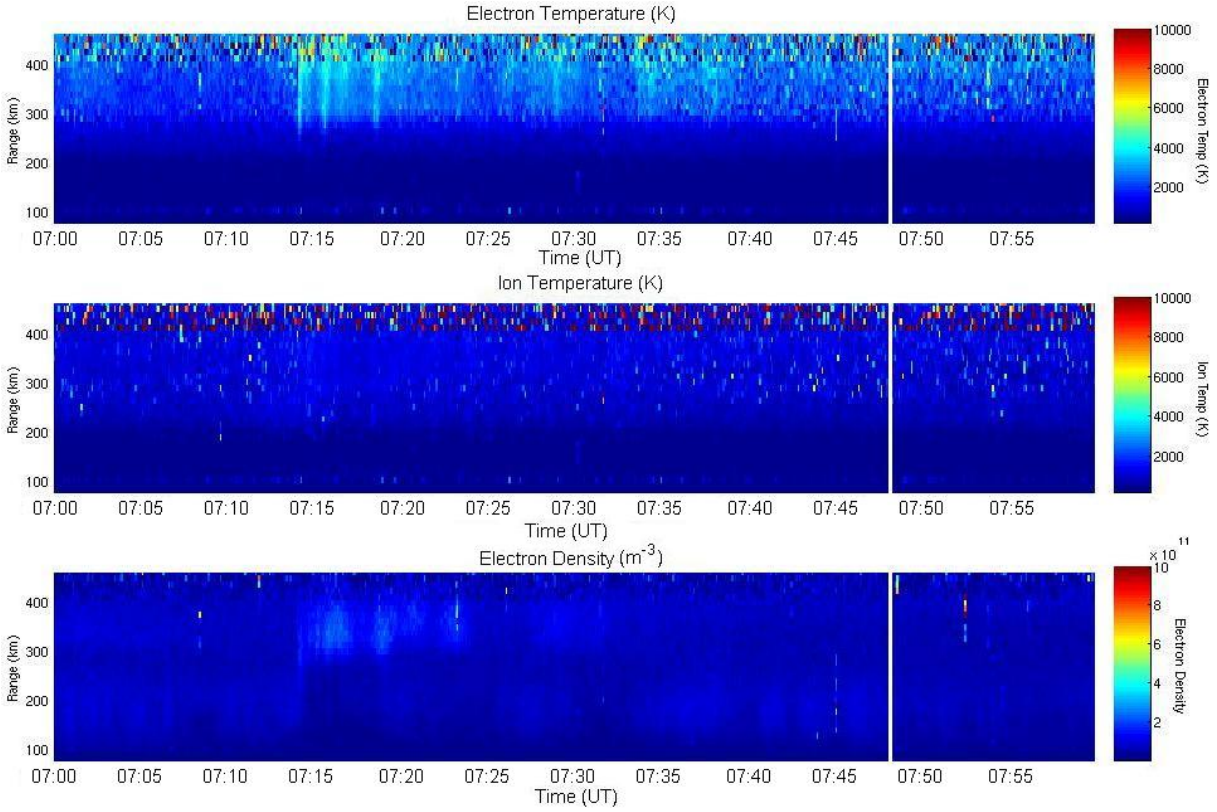

Figure 5.7: Ionospheric parameters plot for 22 January 2012 at 7:00 - 8:00 UT run with the IPY experiment through time, showing electron density (top), ion temperature (middle) and electron temperature (bottom). Times where non-thermal enhancements have been flagged are marked a by white line.

not ion velocity increases. Only three weak NEIAL detections were found in this data set. Figure 5.6 shows data taken with the LT1 experiment at 2 s resolution lasting three minutes. Five time steps containing strong NEIALs were detected within this data set, with 49 weak NEIAL detections made. These weak NEIAL detections matched well with times of enhanced electron temperature. A small number of these time steps also coincided with enhanced ion LOS velocity, but the vast majority did not. Figures 5.7 and 5.8 shows data taken with the IPY experiment at 6 s resolution. No strong NEIAL detections were made before 08:00:00 UT, with a single weak detection made at 07:48:36. There are five separate times where strong NEIALs are detected between 08:00:00 and 09:00:00 UT, with six time steps with weak NEIALs detected during this time. The weak NEIALs appear at times of enhanced electron temperature, with the majority occurring within five minutes of a strong detection. Figure 5.9 shows data taken with the LT4 experiment at 2 s resolution and lasts for three minutes and twenty seconds. Twenty strong NEIALs are detected during this event, alongside four weak NEIAL detections. All detected weak NEIALs lie within 10 s of a strong NEIAL time step. Two of the weak NEIAL time steps show enhanced ion LOS velocities. Figure 5.10 shows data from the Beata experiment over an hour with 6 s resolution. Two strong NEIALs are detected at 22:06 and 22:40, with

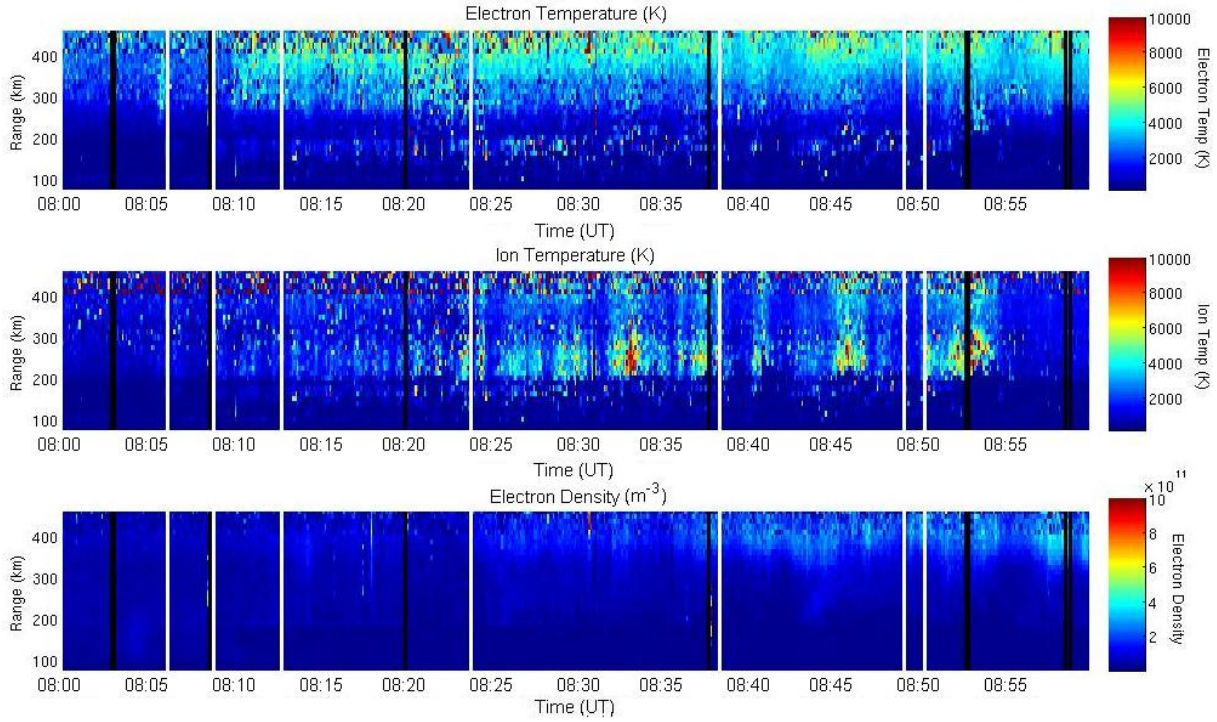

Figure 5.8: Ionospheric parameters plot for 22 January 2012 at 8:00 - 9:00 UT run with the IPY experiment through time, showing electron density (top), ion temperature (middle) and electron temperature (bottom). Times where non-thermal enhancements have been flagged are marked by white lines, and strong NEIAL signatures are marked by black lines.

12 weak NEIAL detections occurring between 22:16 and 22:50. These weak detections occur at times surrounding enhanced electron and ion temperatures. Figure 5.11 shows data from the LT4 experiment at 2 s resolution lasting four minutes and thirty seconds. Three strong NEIALs are detected during this time with 12 weak NEIAL detections. Ion LOS velocity values fluctuate greatly during this event, with the majority of time steps showing height ranges with large velocities.

A clear feature in the results is that the experiments using longer spectral integration times (6 - 10 s), such as Figures 5.5, 5.7, 5.8 and 5.10, found fewer weak NEIAL signatures than those with shorter integration times (2 s in Figures 5.6, 5.9 and 5.11), within the same spans of time. Results using 2 s resolution showed a higher number of weak NEIALs occurring predominantly during times surrounding strong NEIAL events, and sometimes at times when strong events were not detected. Additionally, events of the same time integration during the morning hours (4 to 12 UT) exhibited larger numbers of weak NEIAL detections than those during night-time events (18 to 24 UT). These night-time events, typically exhibited larger numbers of strong NEIAL detections than the during the day time.

Another clear feature is that weak NEIAL time steps regularly occurred at times of increased

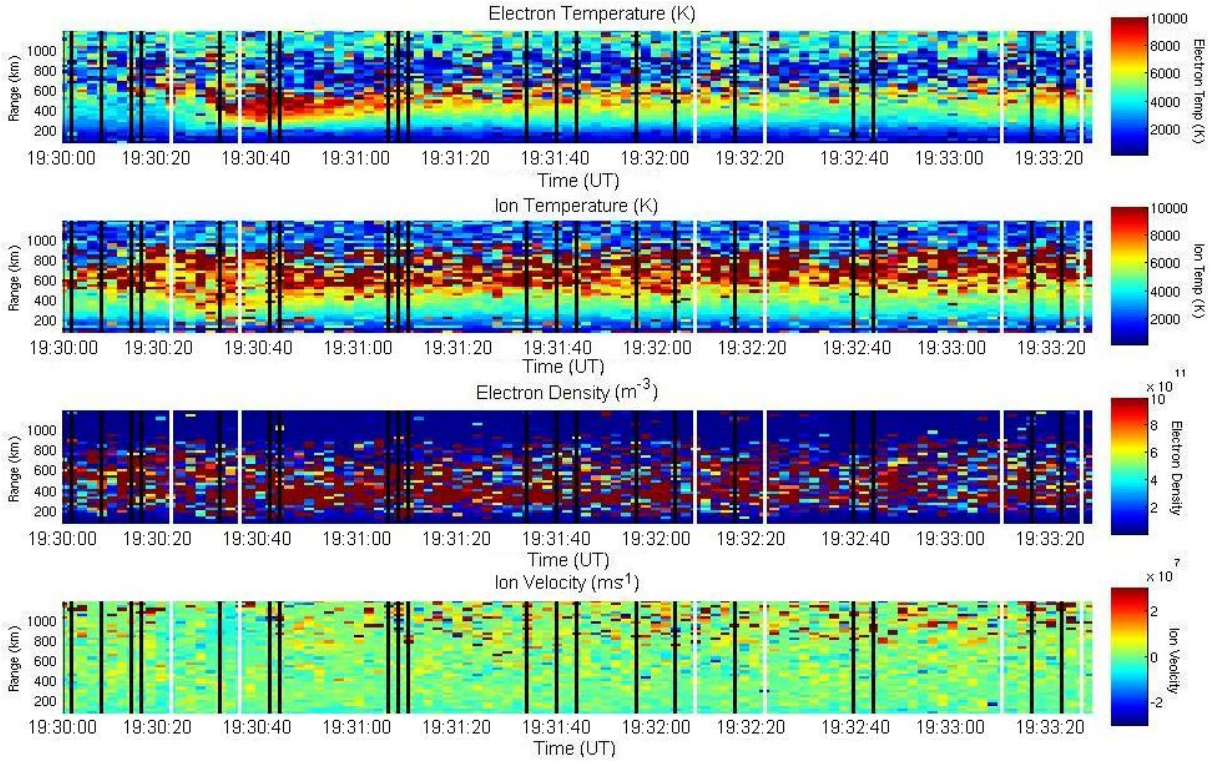

Figure 5.9: Ionospheric parameters plot for 24 January 2012 at 19:30 UT run with the LT4-F experiment through time, showing electron density (top), ion temperature (2nd), electron temperature (3rd) and calculated LOS ion velocity (bottom). Times where non-thermal enhancements have been flagged are marked by white lines, and strong NEIAL signatures are marked by black lines.

ion and/ or electron temperature and / or density throughout all of the events. Of the data at two seconds resolution, the day-side reconnection driven events appeared to show higher numbers of weak NEIAL detections with a lower number of strong NEIAL detections.

5.4 Conclusions

As only six events are analysed here, statistically significant observations cannot be accurately made. However, even with such a limited data set a number of patterns and important trends are evident.

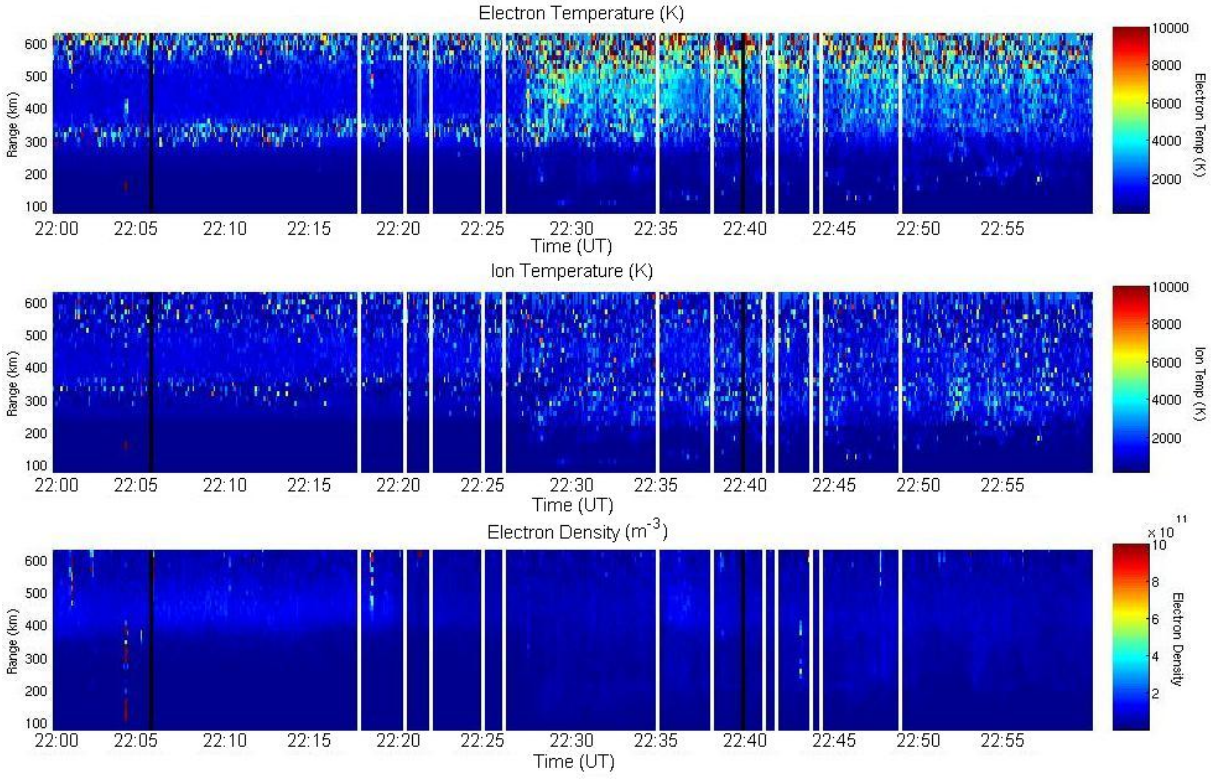

Figure 5.10: Ionospheric parameters plot for 23 February 2012 at 22:30 UT run with the Beata experiment through time, showing electron density (top), ion temperature (middle) and electron temperature (bottom). The time step where non-thermal enhancements have been flagged is marked by a white line, and strong NEIAL signatures are marked by black lines.

Date	Time (UT)	D/N	Resolution	Strong	Weak	Features
24/01/1998	06:00 - 06:48	Day	10 s	46	8	No ion outflow. T_i and T_e enhancements.
26/01/2003	06:56 - 06:59	Day	2 s	8	50	Some ion outflow. T_i enhancements.
22/01/2012	07:00 - 09:00	Day	6 s	9	7	Low N_e. T_i and T_e enhancements.
24/01/2012	19:30 - 19:33	Night	2 s	20	5	Some ion outflow. $T_i > T_e$ enhancement.
23/02/2012	22:00 - 23:00	Night	6 s	2	12	Low N_e. $T_e > T_i$ enhancement.
27/03/2012	10:23 - 10:28	Day	2 s	20	13	No ion outflow. T_i and T_e enhancements.

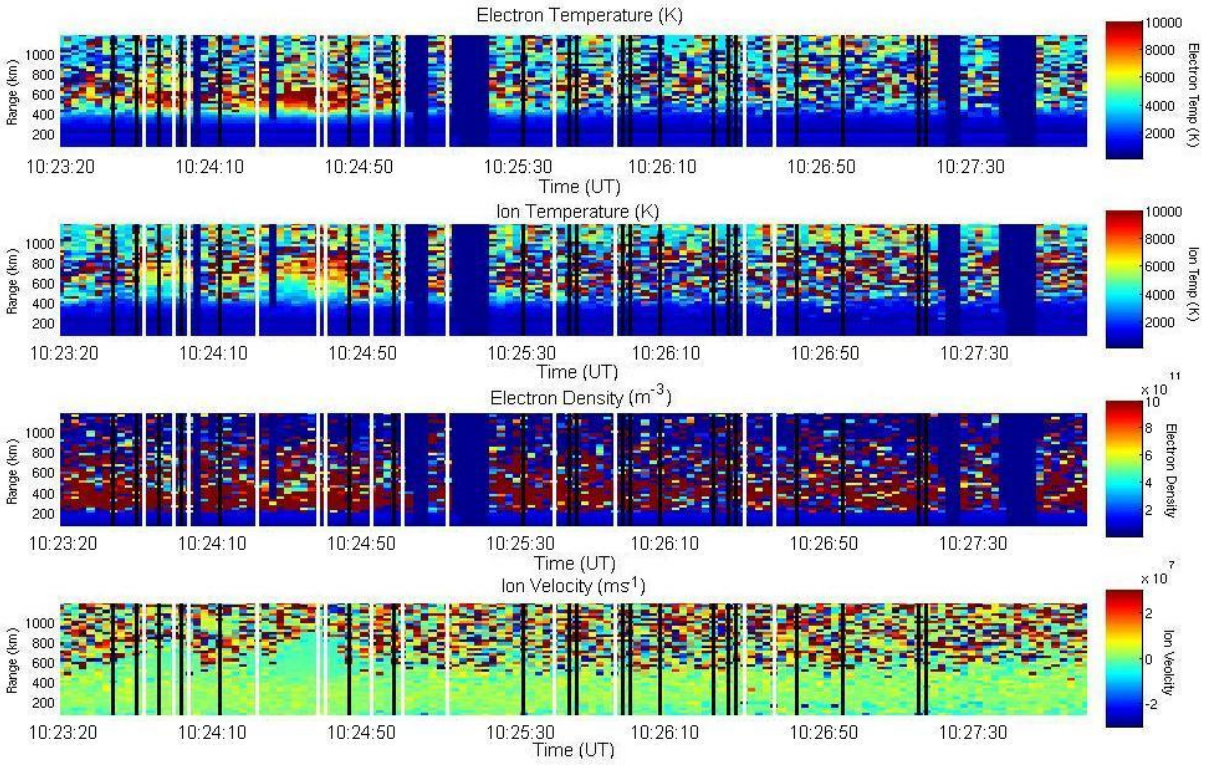

Figure 5.11: Ionospheric parameters plot for 27 March 2012 at 10:00 UT run with the LT4-F experiment through time, showing electron density (top), ion temperature (2nd), electron temperature (3rd) and calculated LOS ion velocity (bottom). Times where non thermal enhancements have been flagged are marked by white lines, and strong NEIAL signatures are marked by black lines.

Naturally Enhanced Ion Acoustic Lines (NEIALs) have been found using analytical techniques to occur at 'weak' levels (not greatly above those caused by thermal processes) surrounding all analysed 'strong' NEIAL events. These enhancements were in addition to the strong enhancements recorded in past literature. These results, which are summarised in Table 5.4 set a new lower limit to the enhancement levels of observed NEIALs. Strong NEIALs were identified by five or more consecutive height gates (excluding the top and bottom five)) with data that was not able to be fit. Possible other reasons that the spectra may not be able to have been fit include non-Maxwellian spectra, satellite echoes and low signal to noise receiving power. However, these phenomena are limited to small height ranges (satellites), or specific altitude at the top (SNR) and bottom (clutter) most range gates ,and so therefore will not be detected as a NEIAL by this method. The table lists the number of weak and strong NEIAL detections for each event and the associated features surrounding them. The fact that fewer both weak and strong NEIALs were observed within data of longer integration times (6 - 10 s compared with 2 s) strongly suggests that both enhancement processes occur at time scales much less than 6 - 10 s integration times and possibly shorter than the 2 second integrations used here. This result adds weight to one of the conclusions of Grydeland et al. [2005], that NEIAL enhancements occur on time scales

shorter than 2 s.

The fact that only a limited number of ion line-of-sight (LOS) velocity increases were detected to coincide with weak NEIAL detections means that the theories of 'type 1 ion-ion two-stream instabilities' [Wahlund et al., 1992] and 'field-aligned currents' [Foster and Aarons, 1988] cannot be the primary driving force behind these events and therefore, are not responsible for the majority of non-thermal enhancements observed.

Large electron temperature increases with no corresponding ion temperature increases have been observed at times of weak NEIALs for a number of events. Therefore, the theory of 'beam-filling solitary waves' [Ekeberg et al., 2010] does not easily fit the data at these times, as it requires enhancement of both. The close temporal correlation between strong and weak NEIAL structures indicates that both enhancements come from similar production processes. During other events, weak NEIALs occur at times where electron and ion temperatures and densities are high. This suggests that the regimes in which they occur agrees well with times and altitudes of auroral precipitation. As all current NEIAL theories suggest high levels of precipitation as a driving factor, these results confirm such conditions. Night-side reconnection events typically involve much higher energy electron precipitation than day-side events. Fewer weak NEIAL and more numerous strong NEIAL detection at night-time reconnection-driven events compared to day-side events would indicate that lower energy precipitation would be the driver for weak NEIALs, with the stronger NEIALs requiring higher fluxes and energies to occur.

Weak NEIALs appear to occur predominantly at times surrounding strong NEIAL occurrences. It is therefore likely that these weak enhancements occur under specific circumstances similar to those of strong NEIALs over short time scales, and so are driven by processes that need to cross a certain energy threshold to occur. This would include the theories of 'beam driven Langmuir waves' [Forme, 1999], 'parallel electric fields' [Rietveld et al., 1991] and 'ion-electron two stream instabilities' [Wahlund et al., 1992] as valid production processes for the above observations. Alternatively, the temperature enhancement limitations ($>$ 120 K) employed in this analysis method may have been too stringent. If this is the case then it is possible that enhancements could occur at even weaker levels than observed here. Unfortunately, it would be extremely difficult to separate these temperature enhancements from those caused by normal thermal processes. Although any temperature enhancement values proven to be non-physical cannot be taken to be fully accurate, the results for the smallest temperature enhancements can be used to approximate what the lower bound energy of enhancements might be during the analysed events. This was set at 1.5 times the maximum thermal losses and a minimum of 120 K, which was twice the error variance of the spectral fitting method.

It is hoped that significantly more NEIALs can be recorded with raw data taking experiments in the future for a more statistical study of these factors.

Chapter 6

NEIAL Positioning Method and Results

Two large Naturally Enhanced Ion Acoustic Line (NEIAL) events were observed with the EASI system on the 24 January (with co-located optical data from the ASK facility) and 27 March 2012. Upon initial analysis of results, it was observed that strong signals did not occur in all antennas for all time steps throughout the events. This meant that the method of ASI as described in Section 1.5 could not be used for these data. A new method of NEIAL positioning was therefore developed to determine the position of the enhancements above the radar system.

6.1 NEIAL Positioning Method

The method involves the EASI radar tracking the phase of the recorded signal for each baseline in altitude. Despite the fact that not all radar baselines received high power, all 10 unique pairs exhibited constant phase gradients over the same altitude ranges and times where NEIALs occurred. An example of such a constant phase observed during the 24 January event can be seen in Figure 6.1. The phase due to normal incoherent scatter is random in nature. Therefore, any coherent phase over a large range must be due to a coherent source, in this case the NEIAL.

6.1.1 Phase Variation Theory

The phase value recorded by a radar pair is dependent upon the position of the coherent scattering object relative to the baseline of the two receiving antennas. The phase value of a cross-correlated set of signals is given by the differences in phase recorded by the individual antennas between $\pm\pi$ radians, caused by the difference in line of sight distance between the source and the individual radars (see Figure 6.2). Any difference greater than $\pm\pi$ becomes the remainder

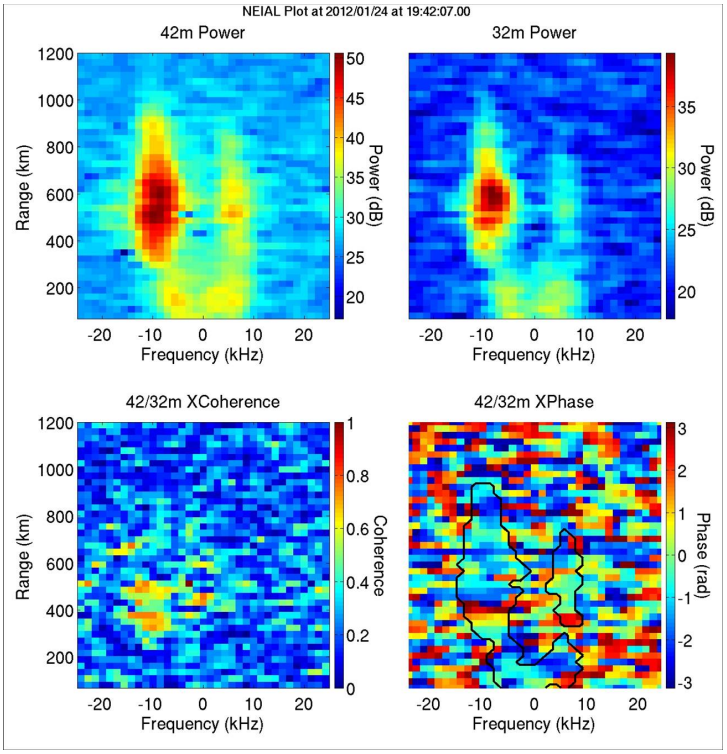

Figure 6.1: NEIAL cross spectra and phase. Top: NEIAL power spectra seen in ESR 32 m and 42 m antennas. Bottom left: Cross coherence between the 32/42 m antennas. Bottom right: Cross phase between the 32/42 m antennas, in which the region of coherent phase is outlined.

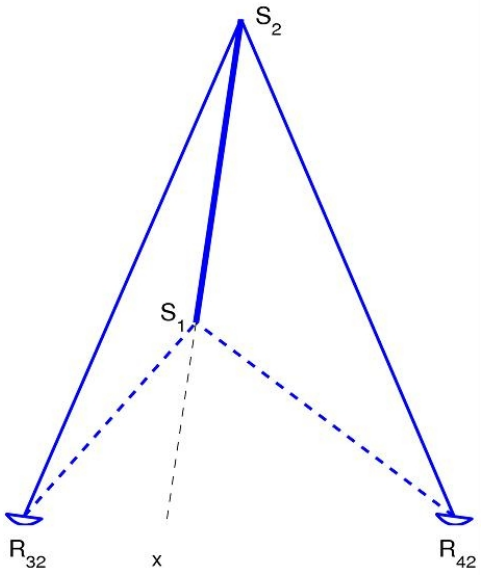

Figure 6.2: Figure of line of sight distance from a source between two radars, and the produced cross-phase values *Courtesy of Bjorn Gustavsson*.

when integers of 2 π are subtracted. However, this phase value can be altered by any systematic offsets in phase from either antenna, or due to line of sight (LOS) velocity created Doppler effects, such that:

$$\phi_{\mathrm{AB}} = \mathrm{mod}2\pi\left(\frac{2\pi \triangle \mathrm{R}}{\lambda}\right) \tag{6.1}$$

$$\phi_{\mathrm{AB}}^{\mathrm{obs}} = \phi_{\mathrm{AB}} + \phi_{\mathrm{A}} - \phi_{\mathrm{B}} \tag{6.2}$$

$$\tag{6.3}$$

where $\phi_{\mathrm{AB}}^{\mathrm{obs}}$, ϕ_{AB} are the systematic phase differences between receivers A and B, ϕ_{A} the phase offset in receiver A, ϕ_{B} is the systematic phase offset in radar B, and $\triangle$ R is the optical path length difference between the two receivers and the target.

It is possible that Doppler contributions can also affect the phase values; this can be calculated by:

$$\phi_{\mathrm{R}} \equiv \frac{\triangle \mathrm{R}_o}{\lambda_{\mathrm{R}}} \pmod{2\pi} \tag{6.4}$$

where ϕ_{R} is the phase for a single receiving radar $d_{\mathrm{R},o}$, the line of site distance between the transmitting radar and the reflecting object, and λ_R the receiving wavelength of the radar.

Alternatively, the phase can be directly determined from combining the real and imaginary components of both received signals such that:

$$\phi_{\mathrm{R}} = \tan(\mathrm{S}) \tag{6.5}$$

where S is the complex cross spectra of the two receivers.

Exact calibration of the EASI system has not been successfully conducted for all EASI antennas. Two antenna offsets (EASI B and C) still need to be accurately determined. Therefore, the above phase results in isolation cannot be used to determine NEIAL positions accurately. However, the gradient of the phase measured with altitude is directly dependent upon the position along the baseline of the observed antennas, and it is unaffected by any systematic phase offsets in the system. Therefore, it was decided this change in phase with altitude could be used to calculate the NEIAL position, using data from all baseline combinations. This proposed method should be ideal for NEIAL observations, due to their altitude-spanning nature. However, with small horizontally spanning objects such as satellites or PMSEs, it would not be possible to use this process to determine their position.

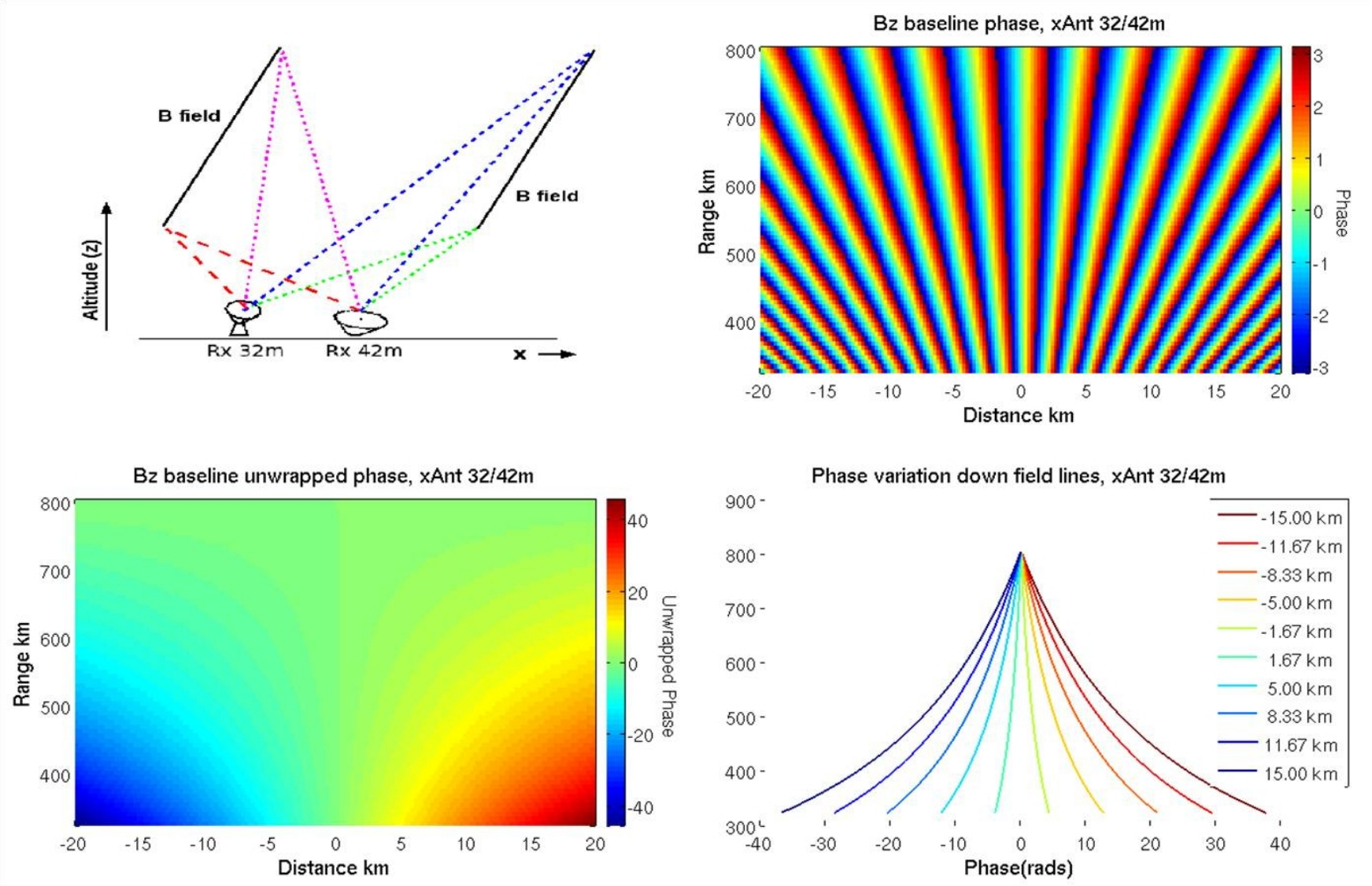

Figure 6.3: Modelled phase variation with altitude. Top left: Diagram of differing line of sight distance and phase for an object extending multiple altitudes. Top right: Model phase variation with altitude along the 32/42 m baseline. Bottom left: Unwrapped model phase variation along the 32/42 m baseline. Bottom right: Model Phase values with altitude for an object extending vertically at specific positions along the 32/42 m baseline.

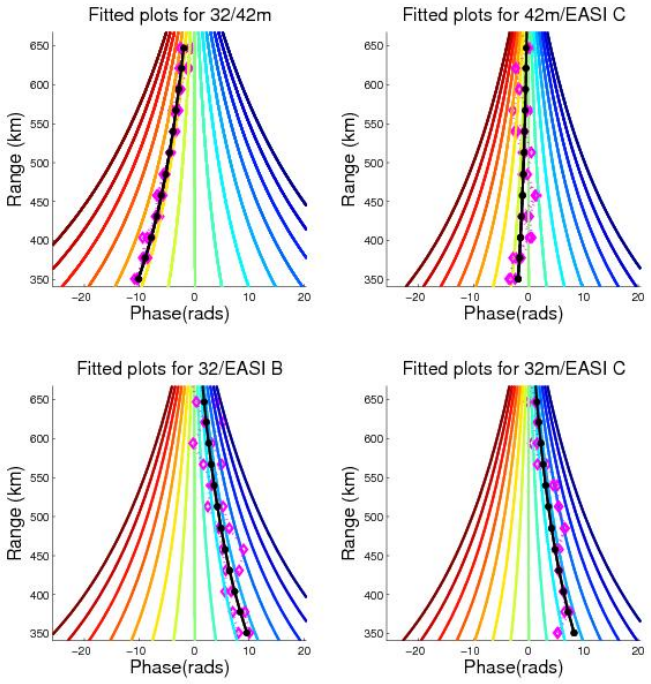

Figure 6.4: Phase variation of down-shifted signal during the NEIAL event on 24 January 2012.

Cross-phase values for given NEIAL positions and altitudes can easily be modelled for each baseline, as the EASI/ESR radar parameters are well known. These values varied only with horizontal position along the baseline being observed and therefore only position along this axis can be determined by one baseline alone. The produced cross-phase pattern alters depending on the distance and orientation of two radars in the baseline, but produces variations similar to that seen in the top right of Figure 6.3.

Due to the 2π modularity of the phase data, ambiguities can arise as to what phase values exactly are recorded. A computational program was used to unwrap the measured phase values to resolve the 2π ambiguities, as can be seen in the bottom left quarter of Figure 6.3. This program assumed a simple linear or quadratic change through results with time, and calculated where phase wraps most likely occurred accordingly. An example of such an unwrapped signal in data can be seen in Figure 6.4.

For all baselines, it can be seen that as the position of the object gets further along the baseline from the centre of the two observing radars, the phase gradient increases for the same range of altitude. Therefore, by tracking the phase variation with altitude, the position where the object must reside along the observed baseline can be determined.

The predicted phase variation of vertically extending objects at specific distances along the baseline has been calculated and plotted in the bottom right hand quarter of Figure 6.3. Using

the baseline position data from all antenna combinations, a two-dimensional foot-point position can be calculated using a 'least square fitting' (LSF) program. The fitting method was used to limit any errors introduced due to noise or low signal.

6.1.1.1 Least Square Fitting

Least Square Fitting (LSF) is a mathematical procedure for finding the best fit for a solution given by a set of points, by minimizing the sum of the squares of the offsets (the 'residuals') of the points from the solution. The sum of the squares of the offsets is used instead of the offset absolute values because this allows the residuals to be treated as a continuous differentiable quantity.

$$\mathrm{E}(x, y) = \frac{1}{2}\Sigma_n(x_n - y_n)^2 \tag{6.6}$$

As squares of the offsets are used, outlying points can have a disproportionate effect on the fit. Therefore, with simple testing, these outlying or high noise values can be quickly identified.

6.1.1.2 Orientation and Size Determination

It has been well documented that NEIAL disturbances flow directly along magnetic field lines. If the observing radars are likewise aligned with the magnetic zenith, the geometry will be such that it is the same as an object extending vertically down a vertically aligned radar baseline. It is for this reason that EASI is aligned and runs aligned with the magnetic zenith 8.4° to the vertical, making the above geometry valid. As the inclination of the magnetic field varies insignificantly over the altitudes examined in this work, the assumption that is constant over this height range should be valid. At higher altitudes, this variation of magnetic field inclination becomes a noticeable factor, which can be solved by orientating the y axis such that is along the magnetic field lines regardless of physical orientation.

Information on NEIAL structure size can be determined from the cross-coherence values from each baseline, as described in Grydeland et al. [2005]. If the exact gain pattern of a radar system is known (such as with the ESR 32 and 42 m antennas), then the size of a structure at a given range can be calculated from the cross-coherence values.

As can be seen in Figure 6.5, the maximum structure size of an object in the length of the baseline is directly proportional to the cross-coherence levels and range of the received signal. Therefore, for each radar time integration a potential estimate of the size of the NEIAL in all baseline directions can be made. However, due to the low power of the EASI antennas and lack of accurate gain pattern knowledge, in this analysis the size estimation is left to only the 42/32 m baseline and this diameter is assumed to be regular in all directions.

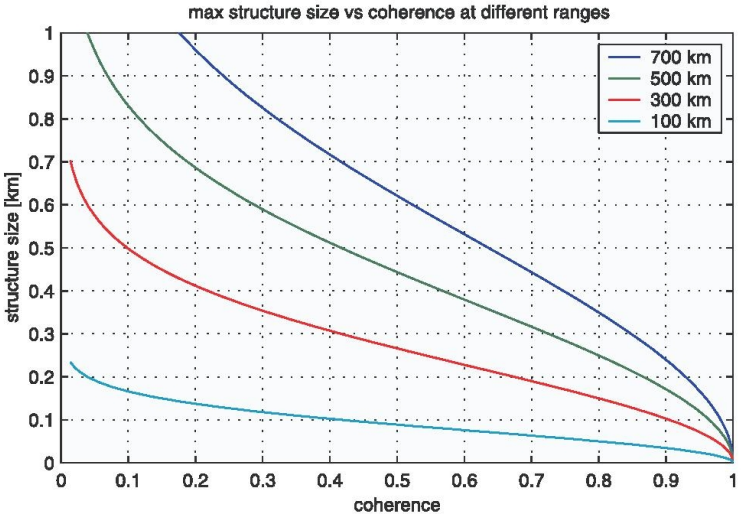

Figure 6.5: Plot of calculated maximum object structure size from ESR 42/32 m cross-coherence values at different ranges. *Courtesy of Grydeland et al. [2005].*

The minimum and maximum scale sizes for each time step (of all used ranges within the time step) were calculated and the error in position for that time was given as the maximum range in either direction.

6.2 Results

Two NEIAL events were observed: the first, on January 24 2012 at 19:41:33 UT, lasted approximately 5 s, the second event was on 27 March 2012 at 10:23:53 and lasted approximately 12 s.

6.2.1 24 January 2012 Event

The 24 January NEIAL observations were taken with both the EASI system and the ASK facility during a substorm event. Using the EASI radar system, the foot-point positions of the observed NEIALs were tracked relative to EASI, and the diameter of these objects estimated from the cross-coherence of the signal, as described by Grydeland et al. [2003].

Enhancements were observed between the ranges of 200 and 800 km, with the highest coherence values being recorded between 200 and 500 km. The positions and recorded ranges (between 200 and 500 km) of coherent NEIAL enhancements computed from EASI data were mapped onto the ASK camera images for the time steps detected.

Figure 6.6 shows the calculated NEIAL foot-point position (row 2 and 3) through time as well as this position overlaid onto ASK camera images (top) throughout the event. The cross-phase

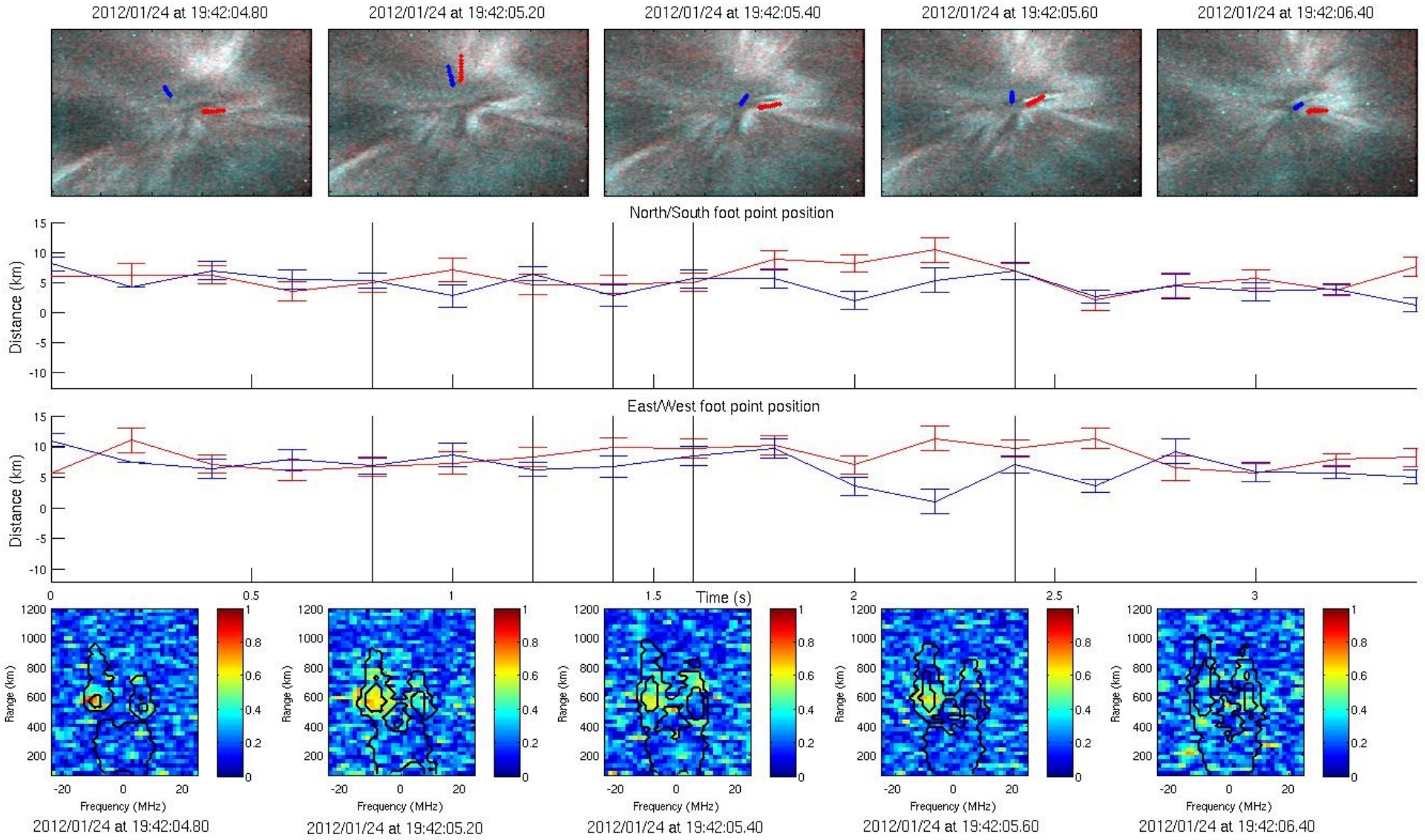

Figure 6.6: NEIAL on 24/01/2012 at 19:42:04 UT. Top: ASK camera images with NEIAL positions overlaid. Row 2: The north/south calculated position of the NEIALs. Row 3: The east/west calculated NEIAL position for the up (blue) and down (red) shifted ion lines with . Bottom: The coherence between the 32 and 42 m antennas, with overlaid 42 m spectral power contours (black). Error bars calculated from the maximum NEIAL scale size as described in Grydeland et al. [2004].

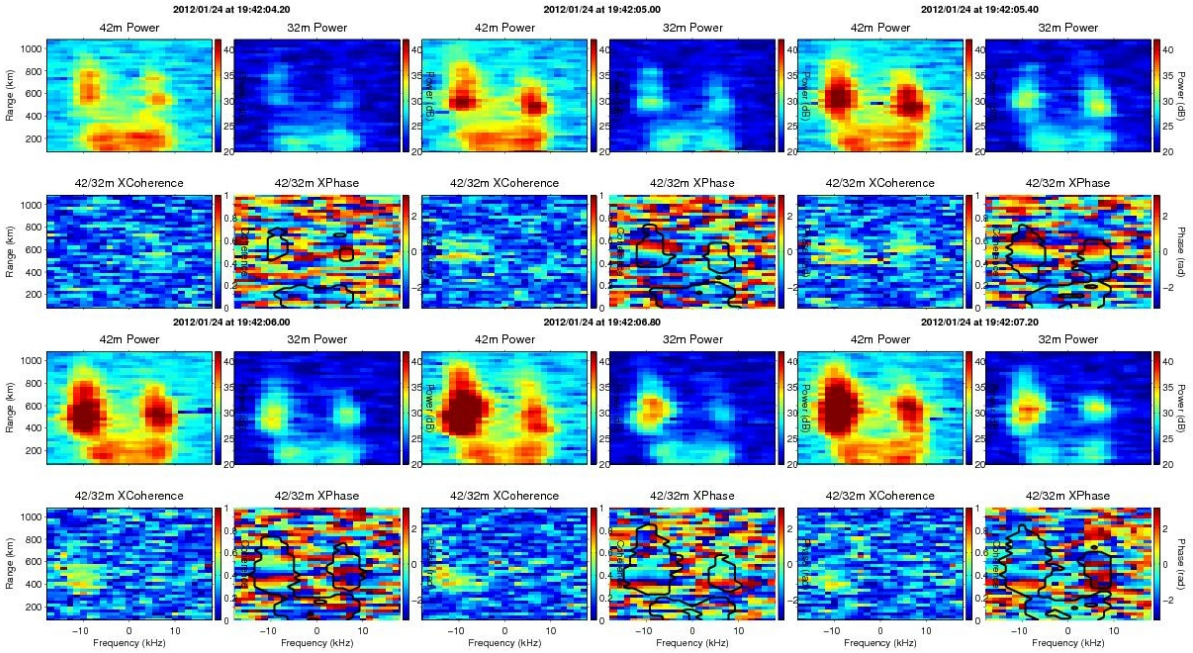

Figure 6.7: Spectra of NEIAL power for the ESR 42 m (top left), 32 m (top right), cross-coherence (bottom left) and cross-phase (bottom right) at six times throughout the 24 January 2012 event.

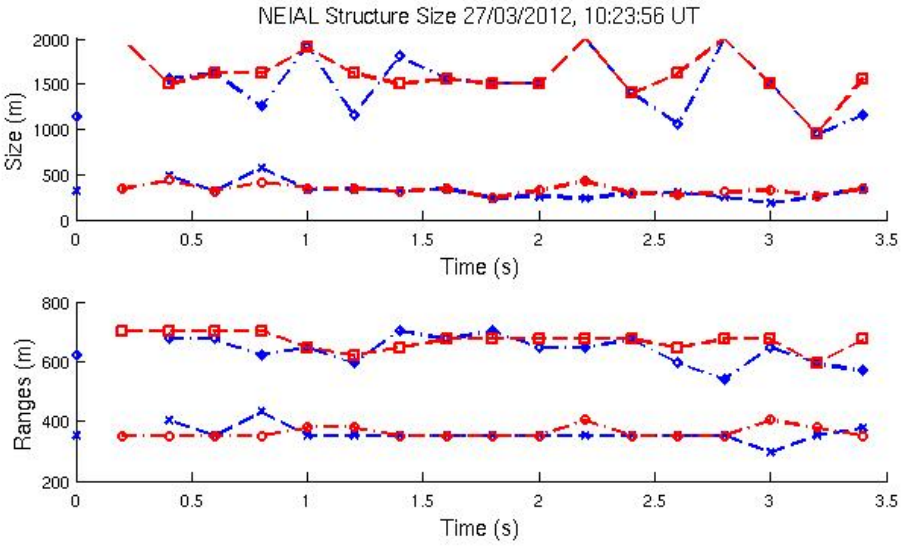

Figure 6.8: Top: Calculated maximum and minimum NEIAL structure sizes for the up (red) and down (blue) shifted ion line shoulders, derived from the cross coherence of the ESR 32 and 42 m antennas. Bottom: Maximum and minimum ranges from which NEIAL position data were used.

values during these images (bottom) is also plotted. It can be seen that the NEIAL positions at the times of strong enhancements match well with the positions of strongly enhanced field aligned auroral rays as observed by ASK.

Figure 6.8 shows the structure sizes (top) and the range extent (bottom) of the NEIALs through time.

The structure sizes associated with the strong cross coherences were calculated at between 117 and 480 m for minimum measured down-shifted sizes (strongest coherence height gate) at each time step, 942 m and 2.0 km for the maximum down-shifted sizes (weakest coherent height gate), 276 and 437 m for the minimum up-shifted sizes, and 942 and 2.0 km for the maximum up-shifted sizes. These large maximum sizes are due to low signal and hence coherence at certain time steps and ranges throughout the event. This is due to the calculated structure size being dependent upon the coherence of the radar signals, which reduce with larger, more diffuse targets. The average minimum down-shifted size was 316 m with the average maximum at 1.47 km, and the minimum up-shifted size being 333 m with the maximum average being 1.61 km. Throughout the event the down-shifted is the clearest and strongest of the two shoulders, which is reflected in the smaller calculated structure sizes. The structures sizes and ranges are seen to follow very closely for the up-shifted and down-shifted shoulders, with the up-shifted shoulders consistently coming from altitudes slightly above that of the down-shifted. The powers and height range of each shoulder throughout the event can be seen in figure 6.7, which plots power against frequency and height gate for the ESR 32 m antenna, 42 m antenna, cross-coherence between them, and the produced cross-phase from this.

The position of the NEIAL remained relatively stable throughout the event between 5 - 10 km north and 5 - 10 km to the east of the EASI system. This indicates that the region where the NEIALs originated from was to the north-east of the ESR facility rather than directly above it, or to the south. Despite the general structure of the substorm progressing southward throughout the event, the minimum sizes of the NEIALs for both ion lines also remained consistent and similar throughout.

For a number of enhancements, the foot-point position of origin appears to be the same for both ion line shoulders. Additionally, the number of time steps where the positions, although not identical, appear within the error bars of each other, is very high, spanning almost half the entire event. This position is consistent with two almost steady high flux auroral rays with a large spread of energies in incoming precipitation, which vary in brightness through the time of the event. The down-shifted ion line in particular (which had the strongest coherence and most constant phase) was consistently aligned with these ray structures throughout the majority of the event, as can be seen in the ASK overlaid images. All optical auroral ray structures emanated from the magnetic zenith during the time of events. At the start of the event the NEIAL positions are aligned with a ray towards the north of the radar, which flares in the first second and then dissipates. The co-located NEIAL positions then switches ray to the east of the radars, which

flares at approximately 1.5 seconds into the event. The co-located positions remain aligned with this ray until the end of the event. The timings of the brightening rays appear linked to that of the strength of the NEIALs, with rays brightening approximately 0.2-0.4 seconds after strong NEIAL signatures are recorded. During times where they are not spatially co-located, the up-shifted shoulder appears to change position to a number of different locations. When these positions are mapped to ASK camera images, they often match the location of different auroral rays. This is possibly due to multiple other enhancement events occurring along other auroral rays but the co-located ray dominating over these event.

During a proportion of time steps where the two ion line shoulders foot points are co-located, they appeared to come from different altitudes. In these cases, the up-shifted origin of coherent spectra was consistently higher in altitude than that of the coherent down-shifted origin. This can be seen clearly in Figure 6.7 where the bulk of the down-shifted coherence comes from lower altitudes than the bulk of the up-shifted shoulder. However, the down-shifted shoulder spans a much larger altitude range, usually stretching up to the same altitudes as the up-shifted peak altitude.

The enhancements varied in power for both the up-shifted and down-shifted shoulders throughout time, with both shoulders dominating at different times throughout the event. In general, the down-shifted shoulder dominated the majority of the time, showing the largest altitude range and power of spectral enhancement. It also constantly exhibited the highest coherence values throughout the event.

6.2.2 27 March 2012 Event

For the NEIAL observations at 10:23:53 UT on 27 March 2012, no optical ASK data were available, due to conditions being too bright to run auroral camera systems.

Figure 6.9 shows the calculated NEIAL foot-point position (row 2 and 3) through time with cross-coherence values (top). These values are overlaid with a contour of the spectral power at these time. In general, the event exhibited stronger power and coherence than that on 24 January 2012, but the strength and frequencies of enhancements changed rapidly. The enhancements occurred concurrently and asymmetrically in both ion line shoulders, varying greatly with time, at some points both being enhanced, at others one shoulder dominating. The coherence values are highest in whichever shoulder dominates at a given time.

Figure 6.10 shows the NEIAL structure sizes and range extent similar to Figure 6.8. It can be seen that the structure sizes were on average smaller than the 24 January event, ranging between 195 and 628 m for minimum up-shifted sizes, 758 m and 1.9 km for the maximum up-shifted sizes, 172 m and 537 m for the minimum down-shifted and 638 m and 2.0 km for the maximum up-shifted scale size throughout the events. The large structure sizes are from time steps and ranges where very low signal was present. The average up-shifted minimum size was 378 m and

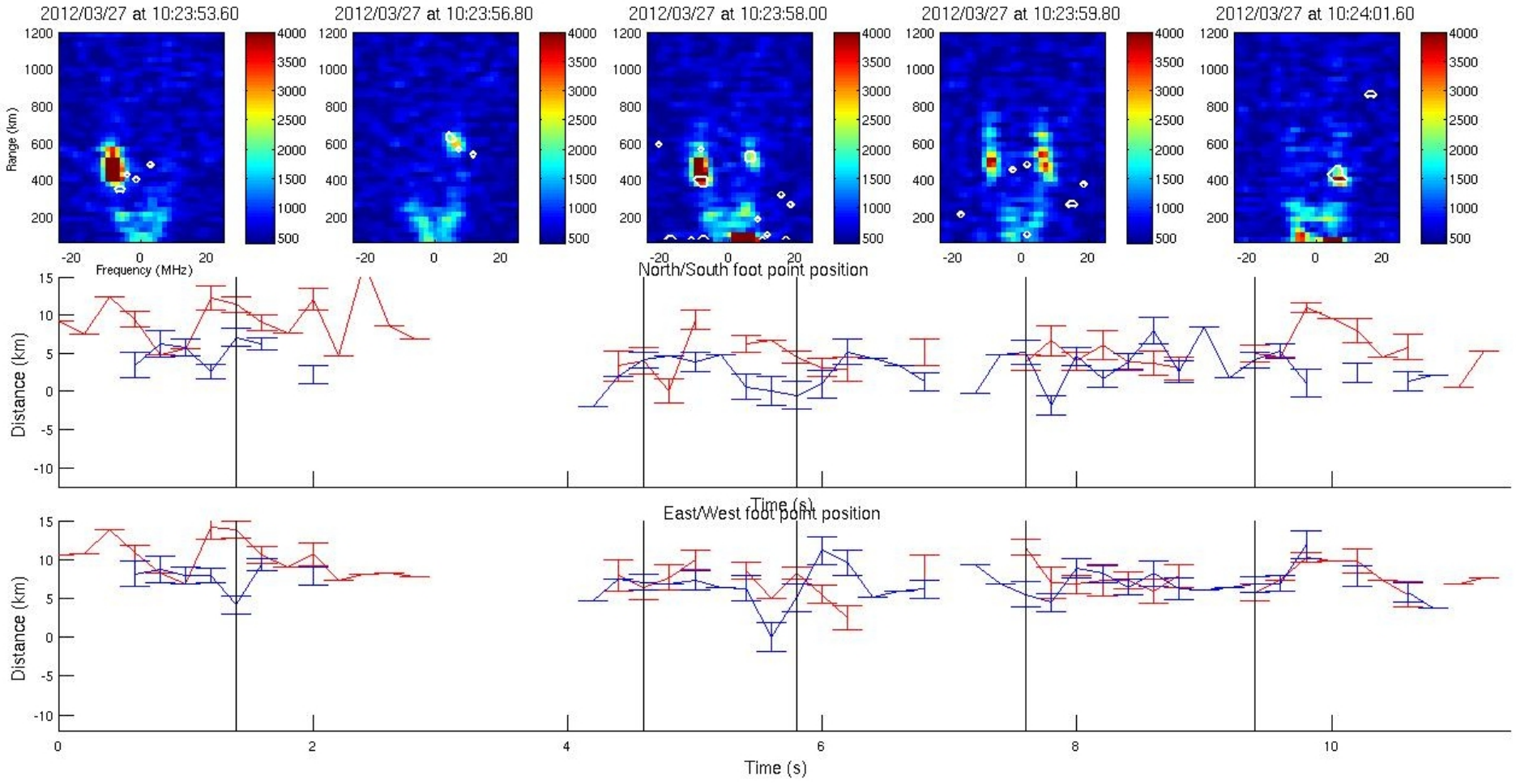

Figure 6.9: NEIAL on 27/03/2012 at 10:23:56 UT. Top: 42 m power profiles. Row 2: Calculated NEIAL foot point position to the north/south. Row 3: Calculated NEIAL position to the east/west for the up (blue) and down (red) shifted ion lines with at specific times during the event. Error bars calculated from the maximum NEIAL scale size as described in Grydeland et al. [2004].

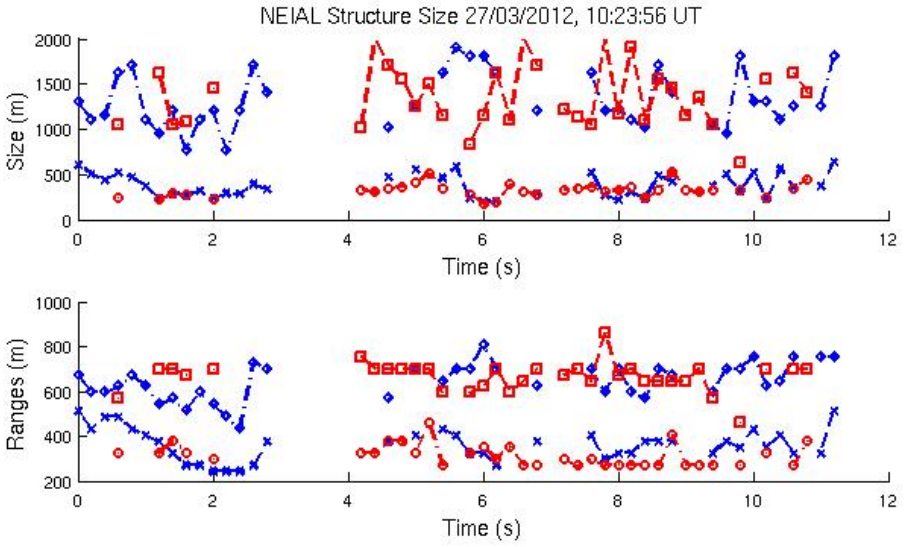

Figure 6.10: Top: Calculated maximum and minimum NEIAL structure sizes for the up (red) and down (blue) shifted ion line shoulders, derived from the cross coherence of the ESR 32 and 42 m antennas. Bottom: Maximum and minimum ranges from which NEIAL position data was used.

the maximum 1.32 km, with the average down-shifted size of 328 m and an average maximum of 1.35 km. These minimum scale sizes are consistently similar through most of the event. It can be seen in Figure 6.10 that during the first two seconds of the event, the up-shifted ion line comes from height ranges higher than the down-shifted shoulder, but this trend is reversed between 7 and 10 s into the event. The altitude ranges of these shoulders varies rapidly throughout.

Times where positions are displayed with no errors are due to either the 32 or 42 m antenna not being able to be used for that calculation, so accurate size estimations could not be made (see Figure 6.9). The sizes of the NEIALs can seen in Figure 6.10. These coherence derived sizes are indicative of NEIALs themselves, as thermally generated incoherent scatter produces zero coherence due to its random nature. The sizes and range results for each shoulder appear to be very similar throughout the entire event. The up-shifted shoulder initially comes from higher altitudes and switches to slightly lower altitudes than the down-shifted NEIALs, about half way through the event.

The calculated positions of the NEIAL structures remained fairly constant with time, particularly for the down-shifted ion line, varying greatest when the signal power dropped. Therefore, this displacement may be due to the noise in the system affecting the results. The position was consistently centred between 5 and 10 km to the east, and 3 and 8 km to the north of the ESR. During a large proportion of the event, up and down-shifted echoes were within the uncertainty of each other for over 60% of the time that both were present. The implication is that echos were from the same field line. This is particularly the case from between 4 and 10 seconds into the event, where the positions appear to differ significantly when the power of one of the shoulders

becomes low, and so sensitive to noise. A more consistent separation in position is observed between 0 and 2 seconds into the event, possibly indicating two different production regions. However, this separation only remains for a single time step and the up-shifted enhancement is of much lower power than the down-shifted during this time.

6.3 Conclusions

The method described in Section 6 of determining the position of NEIALs, and possibly other coherent extended sources, by tracking the variation of phase with altitude has been shown to be successful using the EASI system.

During the 24 January event the NEIAL calculated position and scale size consistently matched that of observed optical auroral enhancements with the low energy 732.0 nm ASK camera throughout the event duration. This indicates that the production source is likely the same for both phenomena. This is backed up by the fact that despite the 24 January event having higher energy and flux of electron precipitation, the 27 March event, which was predominately low-energy electron-precipitation driven, exhibited the highest signal power and coherence and was much more dynamic in nature.

During the 24 January event, coherent up-shifted enhancements appeared consistently to come from higher altitudes and at weaker spectral powers than those of down-shifted enhancements. All high coherence values were taken between 300 and 700 km, all of which agrees well with the statistical findings of Ogawa et al. [2006].

Throughout both events, when both ion line shoulders were strongly enhanced, the calculated scale sizes and positions matched to a high degree, and were well within possible errors of the results. This suggests that these two enhancements are also likely to have come from the same production source during these times.

6.4 NEIAL Background Conditions

To understand the observed NEIAL events in context, the auroral oval conditions were considered. Although decidedly microphysical on the smallest scales in space time, they are inherently connected to solar activity, and the sequence of large scale events. Solar and solar wind data from satellites combines with data a variety of instruments and facilities surrounding the polar region were used to describe the auroral events as they developed.

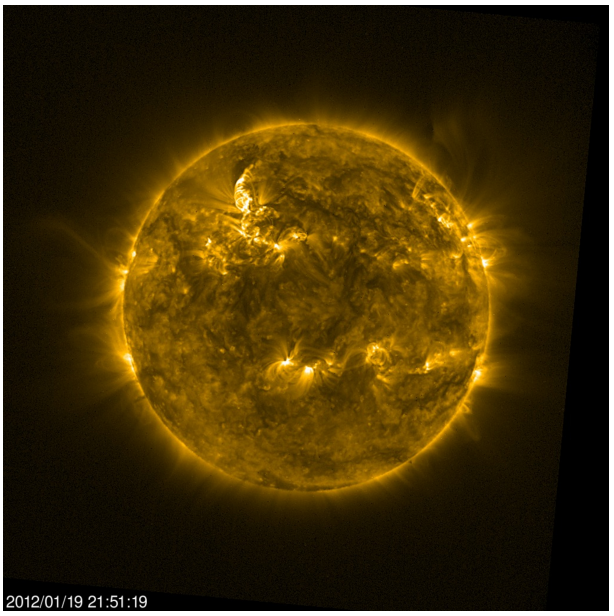

Figure 6.11: SOHO SWAP image at 21:51:19 UT 19/01/2012 showing high solar activity. *Courtesy of NASA*.

6.4.1 24 January 2012 Event

The event at 19:33 UT on 24 January 2012 has been shown by multiple instruments to have been caused by a B_z negative IMF driven reconnection substorm, producing high energy electron precipitation on the night side of the auroral oval. This is supported by all sky camera data showing an abundance of high intensity 557.7 nm OI emissions lines in connection with large disturbances in the H component of ground based magnetometer.

The first indications that a strong auroral event could occur appeared on 19 January 2012, when a number of active regions appeared on the solar surface as viewed in Extreme Ultra Violet (EUV) by the SOHO spacecraft. This can be seen in Figure 6.11, showing activity on the solar surface with the SUMER instrument at this time.

These active regions were connected to solar flares observed in the X-ray spectrum by the GOES satellite, showing powerful eruptions emanating from near the surface of the sun, expelling high energy particles between 19 and 21 January 2012. From these data sets combined with other instruments it was forecast by NASA that the expelled solar particles would cross the path of Earth between 23 and 25 January 2012.

Large IMF disturbances and charged particle density increases in the solar wind due to the CME emissions were detected close to Earth by the ACE spacecraft between 15:00 and 22:00 UT on the 24 January 2012. This can be seen in the top plot of Figure 6.12, which shows the ACE satellite data for solar wind B_z magnetic field orientation (red), and total magnetic strength (black). IMF can be seen to be disturbed by what looks like a shock wave, becoming predominantly IMF

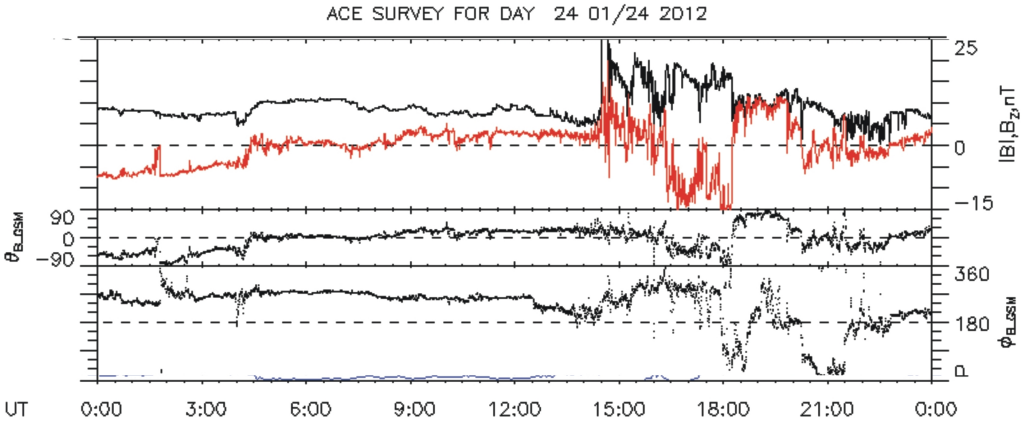

Figure 6.12: ACE spacecraft data from 24 January 2012. *Courtesy of NASA*.

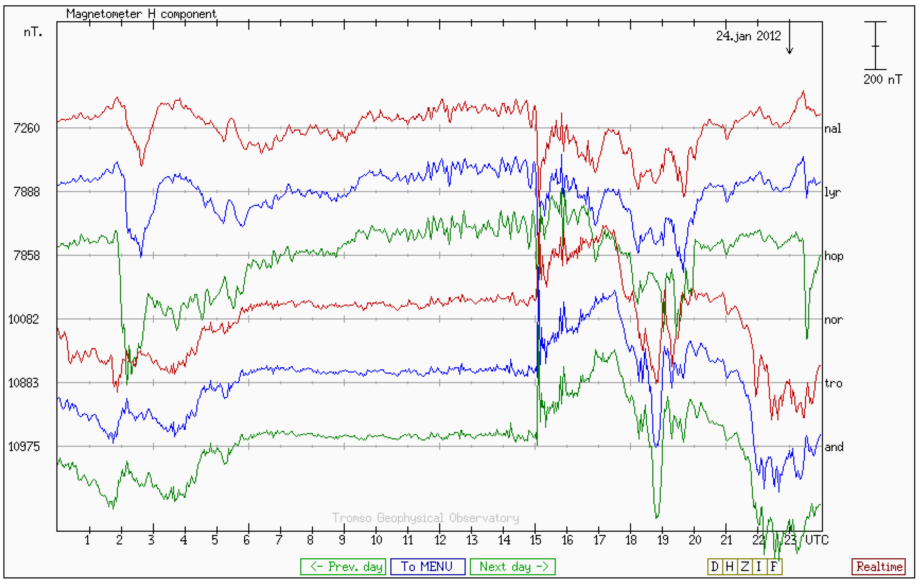

Figure 6.13: IMAGE magnetometer H component (B_H) readings from 24 January 2012. *Courtesy of FMI*.

B_z negative conditions by ∼16:30 UT. These large changes in IMF indicate that reconnection is likely to occur (see Chapter 1), therefore, auroral activity resulting from B_z negative reconnection was expected to occur on the night-side of the Earth at times surrounding 19:00 UT after the day-side reconnected field lines from the southward turning of B_z have been swept into the magnetospheric tail and reconnected there.

Data from ground based Arctic magnetometer stations matched well with satellite IMF observations, showing abrupt changes in horizontal magnetic field readings in all stations at 15:00 UT, which then vary greatly between positive and negative B_H indicating large scale currents in the auroral ionosphere. Figure: 6.13 shows B_H horizontal magnetic field readings from multiple magnetometer stations at decreasing latitudes, at times surrounding the event. A sharp change

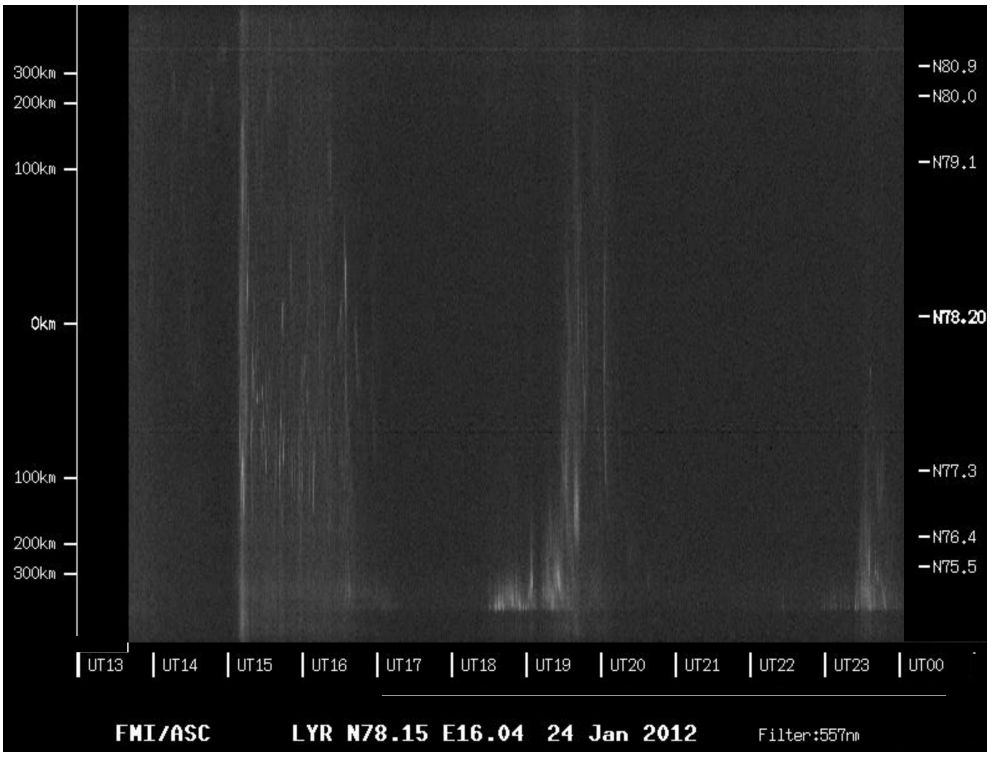

Figure 6.14: All sky 557 nm camera keogram data from the Longyearbyen camera from the MIRACLE network on 24 January 2012. *Courtesy of FMI*.

in magnetic field was clearly seen in the four northern-most stations including Longyearbyen at ∼19:30 UT, when the NEIAL events were observed.

All sky camera data from Longyearbyen showed a large band of auroral activity starting at latitudes above Svalbard. This is seen in Figure 6.14 which plots a brightness keogram of the oxygen 557.7 nm green line, spanning 300 km either side of Longyearbyen. The emission bands are observed to start to the south and expand and spread northward through time, passing over the Longyearbyen station. During the NEIAL events the activity appeared centred over the ESR facility, while spreading over a wide area, spanning over 100 km to the north and south. The emissions slowly dimmed in intensity and disappeared approximately an hour after the original onset, indicating that the break up phase of the substorm occurred ∼ 20 minutes after the NEIAL event was observed.

Accurate SuperDARN data were not available over this region during the NEIAL event, due to maintenance work being carried out on one or a number of the stations at this time. However, a general two cell convection cycle could be ascertained and observed over the pole by modelling data from other stations at times surrounding the event.

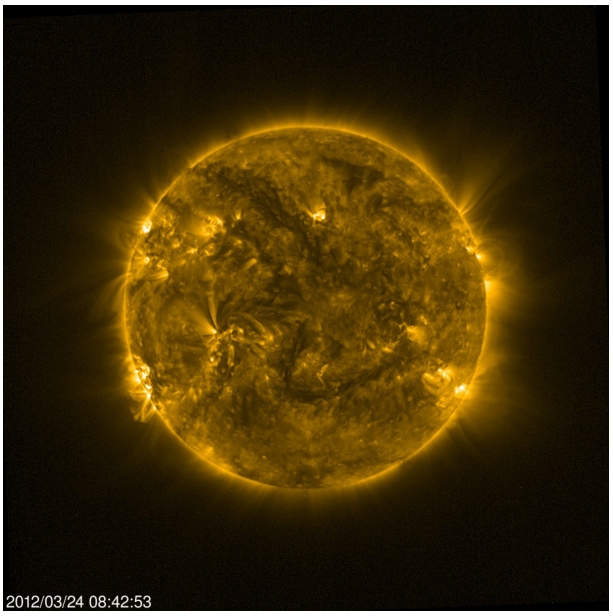

Figure 6.15: SOHO SWAP image at 08:42:53 UT 24/03/2012 showing a large Earth facing CME event. *Courtesy of NASA*.

6.4.2 27 March 2012 Event

The second NEIAL event was observed at 10:28:53 UT on 27 March 2012. SOHO, ACE and magnetometer clearly shows the event was caused by B_z negative reconnection, driving low energy electron precipitation down to the day-side of the poles, with CME driven enhanced solar wind as follows:

Active regions and CME activity were observed by SOHO EUV and LASCO coronagraph instruments on 24 March 2012 (see Figure 6.15). At the same time, high power X ray emissions connected to solar eruptions were recorded by the GOES satellite. These in conjunction with other instruments were predicted by NASA to produce ionospheric disturbances from 18:00 UT onwards on 27 March. However, due to the very limited nature of data sets available, the activity had 24 hours margin of error.

ACE satellite data showed a relatively steady IMF throughout the 27 March 2012. Between 06:00 UT and 15:30 UT the IMF B_z was negative indicating that reconnection could occur.

6.4.2.1 Ground Based Instruments

Ground based magnetometer data showed a mild horizontal B_H negative movement at Svalbard latitudes at approximately 10:00 UT, seen in Figure 6.17. This indicates that electrical currents were occurring in the ionosphere. Such currents are often created on the day-side when there

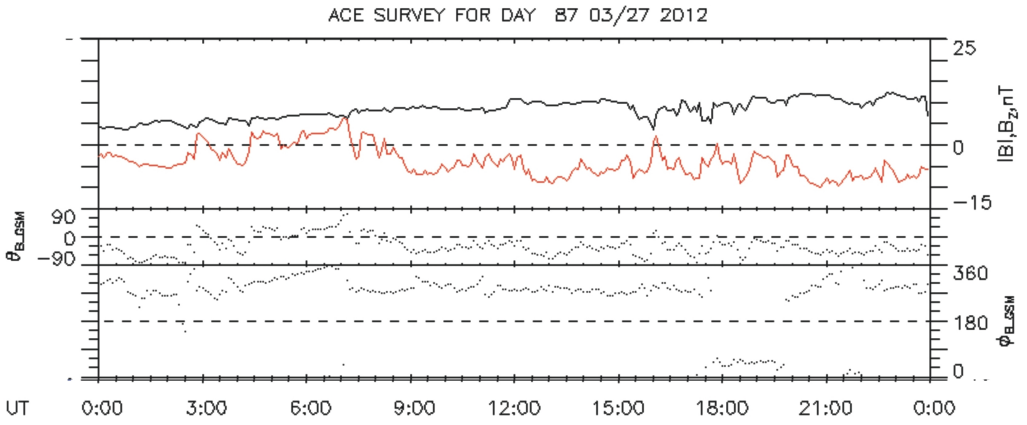

Figure 6.16: ACE spacecraft data from 24 January 2012. *Courtesy of NASA*.

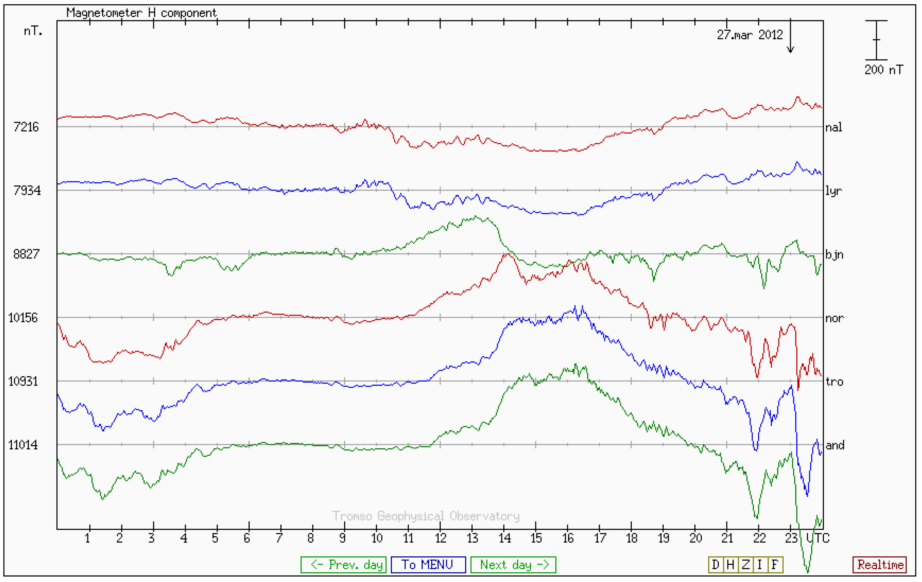

Figure 6.17: IMAGE magnetometer H component (B_H) readings from from 27 March 2012. Small B_H negative movement is observed between 10:00 and 12:00 UT in the two north most magnetometers. *Courtesy of FMI*.

is reconnection between the solar wind and magnetosphere, causing precipitation from the solar wind directly into the dayside cusp.

No auroral optical measurements, were available due to the light conditions being too bright on this date.

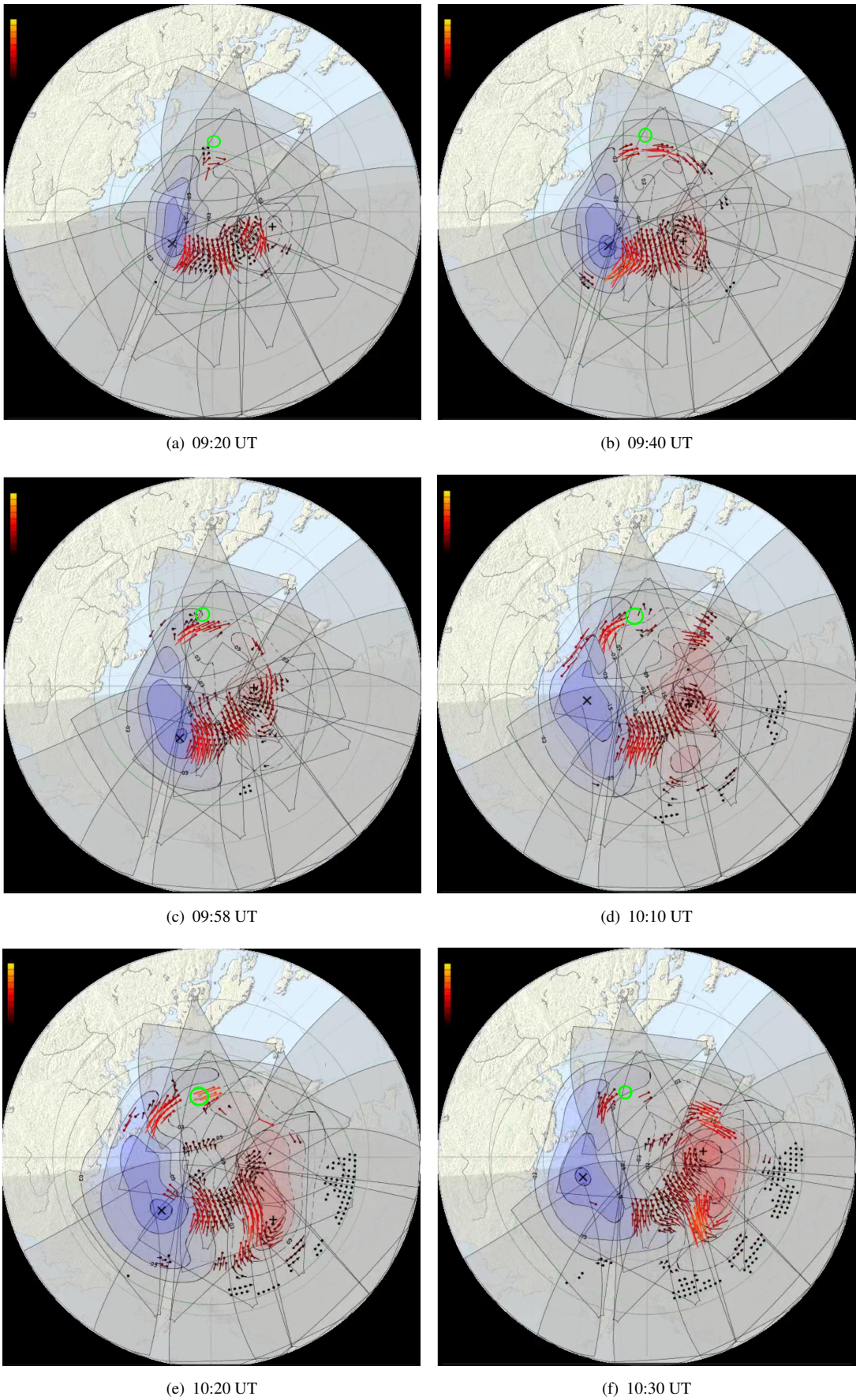

(a) 09:20 UT (b) 09:40 UT

(c) 09:58 UT (d) 10:10 UT

(e) 10:20 UT (f) 10:30 UT

Figure 6.18: SuperDARN convection plot images from 09:20 UT - 10:30 UT on 27 March 2007. Consistent two cell convection pattern with the polar cap close to Svalbard (green circle), with increasing ion drift velocities through time. *Courtesy of SuperDARN*

6.4.2.2 SuperDARN

The SuperDARN data is shown in Figure 6.18. It consists of a modelled polar convection plot of charged particles, calculated by combining with data from multiple stations. A two cell convection pattern is clearly observed throughout the entire time surrounding the NEIAL observation. This indicated that B_z negative reconnection activity was occurring and dominated throughout the entire time surrounding the event. As time progressed until and after 10:00 UT, the velocity of the ion drifts increased, showing increased electric fields and magnetospheric activity. Svalbard was located at the edge of one convection cell on the day-side, close to the polar cap, throughout the NEIAL event. At this position both large eastward and poleward drifts were measured in SuperDARN data, indicating open magnetic field lines and strong electric fields. These conditions usually occur during high levels of auroral activity.

Chapter 7

Conclusions and Future Work

This work has examined two NEIAL events from the 24 January and 27 March 2012, combining optical data where available with a new method of radar positioning provided by the EASI system (see Chapter 6). A statistical study of radar data parameters for these and four other times of auroral activity know to contain NEIALs was undertaken (see Section 5.1), which found strong evidence of previously missed 'weak' NEIAL enhancement. These were found by observing times of non-thermal enhancements in atmospheric temperatures and densities, which are important conditions for the production of NEIALs. ASI techniques were shown to work well with the EASI system for very strong coherent sources such as satellites, and the system was calibrated to a high level of accuracy (see Section 4.4) .

7.1 Conclusions and Discussion

The two NEIAL events observed on 24 January and 27 March 2012 occurred under very different surrounding conditions.

The 24 January event occurred under strong B_z negative reconnection. The event was preceded by observed coronal mass ejections viewed by the SOHO spacecraft. Energetic solar wind parameters were tracked via a number of spacecraft, and magnetic reconnection events preceded by large shock waves observed between 15:00 and 20:00 UT. This precipitation and reconnection created a two-cell polar convection cycle, and a substorm was seen to evolve and expand rapidly at 19:20 UT. At this time, the expanded night-side oval was centred above Svalbard with a diameter of over 200 km in latitude.

High energy electron precipitation was observed as intense brightness observations from the high energy ASK 673.0 nm camera. These high energies were also accompanied by either co-incident or secondary reaction lower energy electrons, as observed by the increased brightness of emission in the co-located 732.0 nm and 777.4 nm ASK cameras. The observed auroral

features were highly dynamic rayed structures, surrounding the magnetic zenith during the time period when NEIALs were observed, indicating that a wide spectrum of precipitating energies and large current densities were involved. Further work has been conducted by Gustavsson et al.(awaiting publication) to model the energy varying along the ray as it flared using the ASK observations, but is not included here. However, the work is an important component in fully understanding the energy spectrum of precipitating electrons during this event.

The 27 March event was preceded by a period of negative IMF, and possible dayside reconnection, producing precipitation over Svalbard under the cusp observed to occur at approximately 10:00 UT. Small magnetometer perturbations were recorded during the time of the NEIAL observations, and a detailed four-cell convection cycle was observed by the SuperDARN global convection maps, suggesting high latitude reconnection was occurring.

7.1.1 Threshold Analysis

Small non-thermal temperature enhancements were observed at a number of times during all six analysed NEIAL events, at a range of time resolutions. These previously unanalysed small enhancements predominantly occurred at times close to large NEIAL observations, and were observed more frequently at shorter time integrations. This relationship suggests that these small enhancements occurred at time scales of 2 s or less, and were caused by conditions similar to those of larger enhancements. Events under the day-side oval appeared to have a higher proportion of weak detections to strong ones compared to night-side observations, which had a greater concentration of strong NEIAL enhancements.

Increases in both ion and electron temperatures and occasionally densities were observed during the majority of flagged 'weak' NEIAL events, with the T_e / T_i also increasing at these times. Although increased ion velocity was observed to coincide with a number of both strong and weak NEIALs during some events, this is not consistently the case, which contradicts the findings of other studies such as Wahlund et al. [1992].

Despite only occurring under specific conditions, the non-thermal temperature enhancements were observed at the lowest observable increases of 120 K in both electron and ion temperatures, over time steps down to 2 s. Enhanstmets of less than 120 K were ignored as they would be within the maximum level of error due to noise. This suggests that although a specific threshold must be met to produce these weak NEIALs conditions, the energies needed to produce them could be relatively small, unless at very short time scales ($<$2 s).

7.1.2 Detailed Observations

Neither of the two NEIAL observations (24/01/2012 and 27/03/2012) at 0.2 s resolutions exhibited consistent equal enhancements of both ion line shoulders. Additionally, the NEIAL

enhancements during both events were seen to vary in power and frequency at time scales of approximately 2 s or less.

All NEIAL structures observed in this work appeared to be volume-extending and show large enhancements, exhibiting consistent phase over a range of altitudes. The position of enhancements during the observed NEIAL event on 24 January 2012 appeared to be directly aligned with a broad energy spectrum of precipitation, as observed by the co-located ASK facility. Additionally, the up-shifted ion line consistently came from altitudes above the down-shifted shoulder. This was true only for the first two seconds of the 27 March event, after which they came from similar heights, or the down-shifted enhancements came from higher altitudes. The constant positioning through time, particularly for the 24 January down-shifted shoulder, suggests a consistent strong stationary production source for the enhancements. The times of highest coherence occurred when both ion line shoulders were enhanced simultaneously. The positions of both up and down-shifted ion line enhancements during both detailed events were relatively consistent towards the north-east of the ESR station, varying most from this when signal power dropped. Therefore, it is possible that a number of the observed position changes were due to increased noise. However, during the 24 January event, non concurrent up-shifted shoulder positions also aligned well with the other prominent optical auroral rays, suggesting other enhancements could be occurring along other field lines, which would negatively affect coherence results. Approximately half of all of the observed NEIALs showed up and down-shifted shoulder line positions that were within the errors bars of each other. The result implies that more than a single enhancement was being produced by increased activity. This is particularly true of the 27 March event, with powers and ranges of enhancements changing rapidly at sub-second time scales.

Both events were predicted to occur within regions containing electric currents. However, in this analysis the 27 March 2012 event, was observed to have the largest enhancements and strongest coherence. The strong correlation between low energy electron precipitation in ASK and NEIAL observation, both temporally and spatially (having a minimum scale size on average at $\sim$380 m), and the fact that the largest enhancements were observed at times where large levels of low energy precipitation existed (particularly in the case of the March 27 event) suggested that the production sources for these two phenomena were linked.

All enhancements occurred consistently centred around a peak frequency for both the up and down-shifted ion line shoulders.

7.1.3 Implication for Current Theories

As neither detailed study showed consistent, static, equal enhancements throughout each event (spectra changed on the order of 0.2 s), and as large measured increases in electron temperatures coincided with the majority of weak NEIALs during all observed events, the theory of 'beam-filling solitary waves' proposed by Ekeberg et al. [2010] appears to be invalid for all events

observed in this work. Additionally, the range-extending, constant-phase enhancements observed in both events contradict those expected by the theory of 'parallel electric field currents' as proposed by Rietveld et al. [1991].

The fact that both up and down-shifted ion line enhancements appear to come from the same source at a large number of time steps during both observations would further exclude the theories of 'field aligned currents' as initially proposed by Foster and Aarons [1988] and 'ion-electron two-stream instabilities' as theorized by Rietveld et al. [1991]. Both of the theories produce an enhancement in only one ion line shoulder and need two separated sources to explain simultaneous enhancements, which is not the case in our observations. Furthermore, the consistent centred frequency observation in the detailed analysis cannot be explained by either of the 'two-stream instability' theories suggested by Wahlund et al. [1992] and Rietveld et al. [1991].

Ion velocity increases were measured to coincide with a number of 'weak' NEIAL events. However, the lack of consistent ion velocity increases during all events indicates these are a possible but not necessary outcome of the observed NEIAL production. This would seem to exclude the theory of 'type 1 ion-ion two stream instabilities' [Wahlund et al., 1992], as well as that of 'field aligned currents' [Foster and Aarons, 1988] as the prime production processes for the observed non-thermal enhancements. The fact that weak NEIAL events were often accompanied by increases in electron and or ion temperature and electron densities would further exclude these two theories. The continued co-location of low energy electron precipitation during NEIALs suggests that these energies may be an integral part of the production process. The processes of 'beam-driven Langmuir waves' suggested by Forme et al. [1995] is the only currently accepted theory connected with low energy precipitation. This theory is backed up by the fact that up-shifted enhancements were regularly observed at higher altitudes than the down-shifted enhancements, indicating a process in which the k mode, and so wave frequency emitted, is reduced with altitude. This is only possible with the 'non-resonant' regime, which loses energy and so undergoes k mode change rapidly with altitude. Simultaneous enhancement observations of both ion lines, at the same altitudes, during the 27 March event, can conversely be described best by the 'resonant' coupling regime of 'Langmuir wave turbulence'.

7.1.4 Solitary Kinetic Alfvén Wave-driven Langmuir Turbulence Hypothesis

In addition to currently published NEIAL production theories, an alternative previously unpublished theory was discussed between Gustavsson and the author in 2011. The theory builds upon a set of research letters from Wahlund et al. [1994b]. They suggest that 'Solitary Kinetic Alfvén Waves' (SKAW) were observed by the Freja and ICB-1300 satellites [Dubinin et al., 1988], and recorded at heights of 1700 km and 900 km respectively. The Freja satellite has recorded SKAW structures of amplitudes up to 150 mV/m at time scales of 0.02 - 0.2 s. The horizontal scale of these structures was successfully derived from the electric signature of the

SKAWs, and was observed to be ∼250 - 300 m in size. As these SKAW structures transition to more electrostatic-like structures, they are observed to reach approximate sizes of 0.2 - 1.0 km. Associated electron/ion density fluctuations caused by these SKAWs were recorded to be up to 50% [Wahlund et al., 1994a]. The sizes and time scale of SKAWs match very closely to the sizes and time scales of NEIALs observed by Grydeland et al. [2003] and Grydeland et al. [2005]. More conclusive observations of NEIALs with both ground and space-based instruments must be conducted at short time scales to test this hypothesis.

Previous modelling [Wahlund et al., 1994b] has shown that these SKAWs can decay effectively and transfer much of their Poynting flux into kinetic energy. It is suggested that these decaying SKAWs could be the process behind a number of the observed NEIAL enhancements. SKAWs start as Alfv́en waves, which are plasma waves that travel down magnetic field lines and are caused by ion density disturbances within a plasma, such as a large influx of high energy electrons caused by reconnection. Under specific conditions, due to velocity drifts between electrons and ions in the plasma caused by Alfv́en wave disruption, a charge separation can occur, leading to kinetic Alfv́en waves forming. In addition to decaying from Alfvénic wave structures, kinetic Alfvén waves can be generated from resonant mode coupling between Alfvén waves and large-scale surface waves, as described by Hasegawa [1976]. Temperature irregularities in a plasma can cause a divergence between two regimes of kinetic Afvén waves, and so cause large perpendicular electric fields to arise, creating electron speed and densities to increase over a small area quickly [Hasegawa, 1976]. Resonant coupling of this process with surface waves in the plasma can further increase amplification of these kinetic Afvén waves and produce electron density enhancements. This density enhancement in turn would produce observed power enhancements seen in incoherent scatter radar data.

As well as directly inducing NEIAL signatures, interactions with SKAWs can force low energy electron beams to be produced, causing pumped Langmuir turbulence to occur. It is theorised that electron beams can be produced by creating an electron shock wave in front of the Alfvén wave, angled down the magnetic zenith [Wu et al., 2008]. When the Alfvén wave velocity decreases due to increased atmospheric density as it propagates through the atmosphere, the electron shock would continue at its previous velocity, and so produce a broadband electron beam. This is most likely to cause the non-resonant regime of Langmuir turbulence. Another process by which this can occur is by resonant coupling with auroral whistler waves as described by Voitenko et al. [2003], with the reaction being modulated by low frequency electromagnetic decay as described by Chian et al. [1994]. Due to this resonance effect, this would likely produce the resonant regime of Langmuir turbulence.

Due to small scale variation in the ionosphere, it is likely that different regimes of these above reactions could occur within a small separation of each other, or that a region could change regime quickly with time. Therefore, this theory predicts that a combination of purely SKAW driven and 'beam driven Langmuir wave' enhancements is likely to be observed over a small area during reconnection events.

7.1.5 Final Conclusions

Over the events observed in this work, the theory of 'beam driven Langmuir waves' first suggested by Groves [1991], furthered by Forme [1993], Kuo and Lee [2005] and others, and that of 'solitary kinetic Alfvén waves' (SKAW) outlined above (see Section 7.1.4), appear to be the only two current theories that can explain all recorded enhancements.

The 27 March 2012 event can only be explained by these theories, and seems to be predominantly due to 'beam-driven Langmuir waves', owing to the purely low-energy precipitation source, caused by day-side reconnection, and simultaneous enhancement coming from similar altitudes and positions. For the other individual events, the majority of other theories have been eliminated independently. However, the beam driven nature of this reaction would imply that of a very defined singular position. However, the fact that the up-shifted shoulder changed positions multiple times throughout the event suggests that multiple enhanced field lines over a large area existed, or that the enhancement regime under which the particular field line was under changed during this time. This observation would seemingly back up the theory that these 'beam-driven Langmuir waves' could be driven by and contained within a larger area under SKAW enhancement. Neither Langmuir wave theory can explain the down-shifted enhancements coming from higher altitudes than up-shifted between 7 and 10 seconds into the event. These events can however be explained via certain SKAW interactions that could block particular observed frequencies.

Enhancements during the majority of the 24 January 2012 event can only be explained by the theory of 'solitary kinetic Alfvén waves', and the 'non-resonant' regime of 'beam-driven Langmuir waves'. At a small number of time steps, where both enhancements simultaneously appear at the same altitude, the 'resonant' regime of this theory explains observations best. Due to the presence of high energy electron precipitation and large electric currents, it is not possible to dismiss other production sources, in particular 'current driven' theories, at a very limited number of times. That said, the consistent nature of the down-shifted foot-point position would seem to indicate a consistent production mechanism throughout the event, for which these are not possible. Under such dynamic high energy conditions, it is difficult to imagine how low energy electron beams would occur without being produced by SKAW or other wave interaction processes.

The observations above would appear to agree with the hypothesis of Sullivan [2008], that the day and night-side B_z negative reconnection-driven enhancement events may be caused by, if not different mechanisms, then different regimes of the same mechanism. Again, only the SKAW driven explanation can describe all of the features and positions observed during this event.

7.2 Future Studies

Before definitive conclusions can be made on NEIAL production, a more statistically significant number of NEIAL enhancement observations need to be made. A number of enhancement events observed over the winter 2012 / 2013 season could contribute to this process. For accurate threshold analysis time integrations of at least 2 seconds, if not shorter, are needed. Therefore, raw data sets will need to be used.

Further phase calibration of the EASI B and C antennas is required to obtain truly accurate ASI images. It is hoped that NEIAL events of high enough spectral power can be observed, and ASI methods can be used for positioning, as well as the 'phase variation' employed in this work.

In situ current, magnetic field, and electric current measurements from satellites at observed latitudes, such as those now possible using multiple 'CubeSats', could greatly increase our understanding of NEIAL production processes. By observing if solitary kinetic Alfvén waves do indeed produce electron beams in ionospheric latitudes, the theory could be more thoroughly examined. Additionally, by monitoring the energy of electron precipitation at these altitudes directly, the criteria for Langmuir wave turbulence to occur can be examined throughout an observed event. The monitoring of strong electric currents and charged particle flows would be able to prove if theories that cite these as production mechanisms do take place during NEIAL enhancements.

With the design study of the 'EISCAT 3D' project now complete, it is hoped that construction of the proposed radar system can begin. The proposed new radar facility will incorporate many thousands of individual antennas in a phased-array, software-driven design. It has a proposed capability of 10 MW in transmitting power, with a physical collecting area of many hundreds of meters, with the signal from antennas being combined in user-defined groups. Therefore, the potential for ASI imaging with this system is enormous, with the possibility of hundreds of baselines available. It would allow for far more detailed positioning of multiple enhancement regions to be made, and production of high resolution ASI brightness images in three dimensions. It is hoped that some of the lessons and methods learned during this work can be used to further improve the potential of the proposed system.

Appendix A

EASI Interferometric Imaging

A.1 Interferometric Aperture Synthesis Imaging

In this work, radar results were taken with the EASI system, which contains three different array types: a static 42 m parabolic dish, a steerable 32 m parabolic dish and three arrays of 4×4 panel antennas. This difference in antennas affects the resulting measurements.

For two different antennas with gain patterns of G_{tx} and G_{rx}, the spatial part of the electric field incident on the scattering volume is given by:

$$E_{inc} = \frac{E_0 R_0}{R} G_{tx}(x/z, y/z) \exp(-2\pi i R) \tag{A.1}$$

where R= $\sqrt{x^2 + y^2 + z^2}$ is the distance from transmitting antenna and E_0 the field at R_0.

The scattering source term is found by multiplying this expression with a factor proportional to the electron density fluctuations $n(x, y, z)$. Scattered field can be calculated by integrating this source term modified by the return distance over the scattered volume. To limit the scattering volume at Z_0 where $Z_0 \gg 1$, (x, y), a function $g(z)$ centred at zero is introduced, to replace z and R with Z_0 when phase is not involved.

The fluctuations can then be defined as:

$$n_k(x, y; Z_0) = \iiint g(z - Z_0\, n(x, y, z) w^{-4\pi i z} dz \tag{A.2}$$

The triple integration over scattered volume can be reduced to a double integral over transverse directions by using this definition if receivers and transmitters are sepparated by a small distance in comparison to the backscattered distance [Sulzer, 1989].

If this field is integrated over the antenna aperture, the received signals for the transmitting and receiving antennas can be given as:

$$\mathrm{f_{tx}} = \frac{\mathrm{C}}{\mathrm{Z_0^2}} \iint n_k(x, y; \mathrm{Z_0}) \mathrm{G_{tx}^2} e^{-2\pi i(x^2+y^2)/\mathrm{Z_0}} dxdy \tag{A.3}$$

$$\mathrm{f_{rx}} = \frac{\mathrm{C}}{\mathrm{Z_0^2}} \iint n_k(x, y; \mathrm{Z_0}) \mathrm{G_{tx}} \mathrm{G_{rx}} e^{-2\pi i(x^2+y^2-\mathrm{A}x)/\mathrm{Z_0}} dxdy \tag{A.4}$$

where the displacement distance (x,y) = (A,0) and the constant phase offset factor $e^{-\pi i \mathrm{A}^2/\mathrm{Z_0}}$ has been discarded.

The complex spatial cross-correlation of the scatter in the two antennas can be calculated as:

$$\begin{aligned} \langle \mathrm{f_{tx}} \mathrm{f_{rx}^*} \rangle &= \frac{\mathrm{C}^2}{\mathrm{Z_0^2}} \int \int \langle |\Delta n|^2 (\theta_x, \theta_y) \rangle e^{-2\pi i A \theta_x} \\ &\times \mathrm{G_{tx}}(\theta_x, \theta_y)^3 \mathrm{G_{rx}}(\theta_x, \theta_y) d\theta_x d\theta_y \end{aligned} \tag{A.5}$$

A.1.0.1 Cross Correlation and Interferometric Autocorrelation

The autocorrelation of a radar signal is how well data from a height gate from one pulse correlates with signal from the same radar at the same height from the following or adjacent pulses.

This combined signal, or cross correlation, can then be autocorrelated with time. The level at which the cross correlated signals autocorrelate for a given integration is known as the coherence between the two received signals.

The coherence is a measure of how well two signals received by the two antennas correlate. If both radars received signal from the same small highly reflective object, then the coherence should be large, and so close to one. Signals from from differing or diffuse low power objects give a coherence close to zero. The coherence can be calculated by normalizing the cross-correlations by geometrical means of the auto-correlations in a frequency by frequency basis, which can then be compared to the computer coherence spectrum. The coherence is given by Sulzer [1989] as :

$$\rho = \frac{\langle \mathrm{f_{tx}} \mathrm{f_{rx}^*} \rangle}{\sqrt{\langle |\mathrm{f_{tx}}|^2 \rangle \langle |\mathrm{f_{rx}}|^2 \rangle}} \tag{A.6}$$

The coherence calculated here should not change as structure of a given size moves across the radar field of view. Only objects which scatter with similar phase differences from each pulse

will be able to be resolved from the noise after integration. Coherence calculations only work when the scattering object is much smaller than the size of the radar beam width.

Grydeland et al. [2004] computed that comparison with ESR 32 m and 42 m radars showed that difference in coherence was negligible for small structures, and not generally insignificant for larger structures. They observed that a small drop in coherence was seen for larger structures [Grydeland et al., 2004].

A.1.1 Implication of EASI Radar Differences

The equations above show the effects of using radars with different gain patterns to view different spatial objects. In this work three different radar systems were used to probe NEIAL structures of small spatial widths of between 200 and 500 m. The fact that NEIAL structures occur in areas much smaller than the beam of the antennas is of great benefit in this case. For much narrower scatterers $\sum_{ij} \gg \sigma_x, \sigma_y$, such that $\sum_{i,j,x} \sim \Sigma_x$ and $\sum_{i,j,y} \sim \Sigma_y$ and so the above coherence equations can be simplified to:

$$\gamma i,j = e^{2\pi i \mathrm{D}_{i,j} \Theta_0} \exp\left[-\frac{(2\pi)^2}{2}(\mathrm{A}_{ij}^2\sigma_x^2 + \mathrm{B}_{ij}^2\sigma_y^2)\right] \tag{A.7}$$

which ends up similar to the equation for antennas of identical size and gain pattern. Therefore, for our purposes despite using different radars we were able to produce reasonably accurate aperture synthesis images. The cross-coherence can be used to estimate the size of the reflective structure along the observed baseline. This is looked into more detail in section 6.1.1.2.

A.1.2 Aperture Synthesis Imaging Technique

Aperture Synthesis Imaging (ASI) produces images by combining sets of coherence and cross spectral data. The accuracy of these images depends on the gain power, position and number of antennas in the installation. To produce a perfect image of the brightness, ideally every baseline of the frequency used would be covered by the radar installation. In reality usually only a small number of desired baselines are covered, depending on the use of the installation. This results in the production of a dirty brightness image of the probed object, as not all baseline structures are present.

To calculate ASI for ionospheric targets, the source can be assumed to behave in a thin sheet, to be spatially incoherent, quasi-monochromatic and that the Huygens Principle is valid. In this case, the cross-correlation between radars at points r_1 and r_2 can be given to a good approximation as:

$$\mathrm{V}_{\omega}(r_1, r_2) = \int \mathrm{B}_{\omega}(s)\exp[-i\omega s(r_1 - r_2)/c]d\Omega \tag{A.8}$$

where B_{ω} is the angular brightness Fourier transform in r_1,m,n in the direction of the unit vector s = (l,m,n), where l,m,n are the directional cosines of vector s, integrated over a unit sphere.

The baselines (spatial separation at a particular orientation) between all antenna pairs can be expressed in wavelengths $\lambda = 2\pi c/\omega, r_1 - r_2 = \lambda(u, \nu, \omega)$, which becomes $r_1 - r_2 = \lambda(u, \nu, 0)$ when expressed in the measurement plane $\omega = 0$. In this coordinate system, the components of vector s are $(l, m, \sqrt{1 - l^2 - m^2})$ and the angle from this $d\Omega = dl\ dm/\sqrt{1 - l^2 - m^2}$ resulting in:

$$\mathrm{V}_{\omega}(u, \nu) = \int\int \frac{\mathrm{B}_{\omega}(l, m)}{\sqrt{1 - l^2 - m^2}} e^{-2\pi i(ul + \upsilon m)} dl\ dm \tag{A.9}$$

This integral has the form of a 2-D Fourier transform. If the target only occupies a narrow angular region, then this visibility image can be inverse-transformed into a brightness function as described in Grydeland and La Hoz [2010].

Due to the Fourier transform, the above calculation creates a brightness image, which is called the 'dirty image'. This dirty image is usually very distorted, and it is primarily used as an initial input for more effective restoration or inverse algorithms later in analysis. This is due to the noise of the machine being included into the signal and usually a non full set of baselines, leaving gaps in the Fourier spectrum. To restore this image two main operations need to be done; these are the deconvolution and Fourier transform. Using the convolution theorem we obtain:

$$\mathrm{D}^{\mathrm{D}}_{\omega}(l, m) = \mathrm{B}_{\omega} \star \mathrm{G} \tag{A.10}$$

where the D(l, m) is the convolution, B the brightness image, G the point spread function, and $\star$ is the Fourier transform of the sampling function, such that:

$$\mathrm{G}(l, m) = \int\int \mathrm{S}(u, \nu)\mathrm{e}^{2\pi i(ul + \nu m)} du\ d\nu \tag{A.11}$$

There are two other effects that can distort measured brightness: the finite width of the antenna beam elements and the finite bandwidth of the receivers. The first of these can be corrected reasonably simply, and the second can be made negligible by using sufficiently narrow bandwidth, which for EASI is 50 kHz.

Problems arise when trying to deconvolve the above equations to obtain the clean brightness from this dirty brightness. In almost all cases the true visibility cannot be reproduced, as the problem is highly singular: $\mathrm{V}_{\omega} = \mathrm{V}^{\mathrm{D}}_{\omega}/\mathrm{S}$ where $\mathrm{V}^{\mathrm{D}}_{\omega}$ is the measured visibility. The sampling

function (S) is full of blind spots over large regions of the $u\mu$ plane where no measurements are made. Therefore, the above relation is undefined as S in these regions. As a result exact visibility and brightness are unrecoverable.

However, if it is known what produced images should appear like, using regions that are accurately measured, an image can be artificially restored using certain algorithms, which amounts invariably to extrapolation.

A.1.2.1 EASI Limitations

Image no	Radar 1	Radar 2	Gradient
1	42 m Real	42 m Real	N
2	42 m Real	32 m Real	Y
3	42 m Real	EASI A Real	Y
4	42 m Real	EASI B Real	Y
5	42 m Real	EASI C Real	Y
6	32 m Real	32 m Real	N
7	32 m Real	EASI A Real	Y
8	32 m Real	EASI B Real	Y
9	32 m Real	EASI C Real	Y
10	EASI A Real	EASI A Real	N
11	EASI A Real	EASI B Real	Y
12	EASI A Real	EASI C Real	Y
13	EASI B Real	EASI B Real	N
14	EASI B Real	EASI C Real	Y
15	EASI C Real	EASI C Real	N
16	42 m Im	42 m Im	N
17	42 m Im	32 m Im	Y
18	42 m Im	EASI A Im	Y
19	42 m Im	EASI B Im	Y
20	42 m Im	EASI C Im	Y
21	32 m Im	32 m Im	N
22	32 m Im	EASI A Im	Y
23	32 m Im	EASI B Im	Y
24	32 m Im	EASI C Im	Y
25	EASI A Im	EASI A Im	N
26	EASI A Im	EASI B Im	Y
27	EASI A Im	EASI C Im	Y
28	EASI B Im	EASI B Im	N
29	EASI B Im	EASI C Im	Y
30	EASI C Im	EASI C Im	N

Full list of possible EASI baselines.

For the EASI system we have five antennas. When combined this produces a total of 30 baselines as seen in the table above. This is comprises of 10 raw power values (real and imaginary parts of radar i combined with radar i), and 20 physical baselines (real and imaginary combinations of radar i and j). As only a very small number of possible baselines are covered, the images produced are by no means perfectly representative of the brightness of objects observed. However, the accuracy of the system is such as to be able to distinguish accurately between multiple objects separated in the order of 1 km spatially, with a time resolution of $\sim$0.1 s. This is accurate enough to conduct new scientific observation of NEIALs. By combining data products from different heights and integrating time steps, this accuracy can be improved with the trade off of either height or time resolution.

Appendix B

Thermal Loss Processes

The temperature of given atmospheric species, in particular electrons and ions, varies greatly throughout the Earth's atmosphere, especially so between different regions of the ionosphere. For this work it is important to understand how quickly temperature can dissipate at specific altitudes. The process of how this is calculated is presented below.

Thermal loss rates for different altitudes and species have been a subject of great discussion in the scientific community over the last 40 years. In the last decade, recent developments in the field such as the study of Nicolls et al. [2006], have provided theoretical thermal interaction to an unprecidented degree of accuracy.

As described in Section 1.2, the Earth's upper atmosphere varies greatly with altitude from the surface. Therefore, at different regions in altitude different species and reactions dominate. Historical observations show that large NEIAL events occur in the F1 and F2 regions and rarely extend down to the D region. Therefore, the D region will be largely ignored in this analysis and F1 and F2 regions concentrated upon.

B.1 Electron Energy Exchange with Neutrals

The prime source of temperature or kinetic energy loss of electrons is through collisions (quenching) with neutral atmospheric species.

Owing to their smaller mass, it can be assumed (and has also been observed) that the average electron temperature is higher than that of ions, which are themselves at a higher temperature than neutral species, such that:

$$\mathrm{T}_e > \mathrm{T}_i > \mathrm{T}_n \tag{B.1}$$

Therefore, when an electron collides with a neutral species some of its kinetic energy is transferred, and so the temperature decreases.

B.1.1 Elastic Collisions

The generalized formula for energy transfer from particle 1 at T_1 in an elastic collision with particle 2 at T_2 as described in Schunk et al. [1978] and Banks and Kockarts [1973], is given by:

$$\mathrm{L}_{1,2} = -2n_1 \frac{m_1}{m_1 + m_2} \upsilon_{1,2} \frac{3}{2} k(\mathrm{T}_1 - \mathrm{T}_2) \tag{B.2}$$

where $\upsilon_{1,2}$ is the momentum transfer collision frequency defined as:

$$\upsilon_{1,2} = \frac{16}{3} \frac{n_2}{m_1} \mathrm{M}_R \Omega^{1,1}_{1,2} \tag{B.3}$$

The collision frequency requires prior knowledge of the collision cross section which is dependent on the particles involved. The collision cross section is a proxy for the likelihood that the two particular particles involved will collide. Electrons due to being much smaller than ions and neutrals produce much smaller collisional cross sections than combinations involving other species. The equation for calculating the collisional cross section of two particles can be given by:

$$\begin{aligned} \Omega^{1,1}_{1,2} &= \frac{2k}{2\pi^{1/2}} \left(\frac{\mathrm{T}_1}{m_1} + \frac{\mathrm{T}_2}{m_2} \right)^{5/2} \\ &\times \int_0^\infty \upsilon^5 \exp\left(-2k\upsilon^2 \left(\frac{\mathrm{T}_1}{m_1} + \frac{\mathrm{T}_2}{m_2} \right) \right) \phi^{(1)}_{1,2}(\upsilon) d\upsilon \end{aligned} \tag{B.4}$$

where $\Omega_{1,2}$ is the collisional cross section, T the temperatures of the particles and m the masses of the particles.

Once the collisional cross-section of the particles has been calculated, the energy transferred between the particles due to the elastic collision can be calculated. For a collision involving electrons and neutral particles, this energy transfer or loss can be given as:

$$\mathrm{L}_{\mathrm{elastic}}(e, n) = -16 n_e n_n \frac{m_e}{m_n} \Omega^{1,1}_{e,n} k \mathrm{T}_e - \mathrm{T}_n \tag{B.5}$$

where L is the energy loss. As stated above, this means that $m_e \ll m_n$.

The value of this energy loss as can be seen in Equation B.5 depends upon the particle it is colliding with, and so varies for each species. As described by Rees and Lummerzheim [1989], the elastic collisional energy losses for electrons with each of the main atmospheric species can be simplified down to:

$$\begin{aligned}
\mathrm{L}_e(e,\mathrm{N}_2) = &\quad 1.77\times10^{-19} n_e n(\mathrm{N}_2) T_e (1 - 1.21\times10^{-4}\mathrm{T}_e)(\mathrm{T}_e - \mathrm{T}_n) && \mathrm{eV\ cm^{-3}s^{-1}}\\
\mathrm{L}_e(e,\mathrm{O}_2) = &\quad 1.21\times10^{-18} n_e n(\mathrm{O}_2) \mathrm{T}_e^{1/2}(1.0 + 3.6\times10^{-2}\mathrm{T}_e^{1/2})(\mathrm{T}_e - \mathrm{T}_n) && \mathrm{eV\ cm^{-3}s^{-1}}\\
\mathrm{L}_e(e,\mathrm{O}) = &\quad 3.74\times10^{-18} n_e n(\mathrm{O}) \mathrm{T}_e^{1/2}(\mathrm{T}_e - \mathrm{T}_n) && \mathrm{eV\ cm^{-3}s^{-1}}\\
\mathrm{L}_e(e,\mathrm{H}) = &\quad 9.63\times10^{-16} n_e n(\mathrm{H})(1 - 1.35\times10^{-4}\mathrm{T}_e) \mathrm{T}_e^{1/2}(\mathrm{T}_e - \mathrm{T}_n) && \mathrm{eV\ cm^{-3}s^{-1}}\\
\mathrm{L}_e(e,\mathrm{He}) = &\quad 2.46\times10^{-17} n_e n(\mathrm{He}) \mathrm{T}_e^{1/2}(\mathrm{T}_e - \mathrm{T}_n) && \mathrm{eV\ cm^{-3}s^{-1}}
\end{aligned} \tag{B.7}$$

(B.7)

B.1.2 Inelastic Collisions - Kinetic Energy Transfer

Not all collisions between particles are elastic. A large number of interactions dissipate or lose kinetic energy in a variety of ways. Inelastic collisions can occur due to many factors and so therefore the equation describing them includes these possible interactions. In general the equation for an electron inelastically colliding with neutrals can be described as in Rees and Lummerzheim [1989] by:

$$\begin{aligned}
\mathrm{L}_{\mathrm{inelastic}}(e,n) &= 2\pi \left(\frac{1}{\pi k \mathrm{T}_e}\right)^{3/2} \left(\frac{2}{m_e}\right)^{1/2} \frac{n_e n_n}{\sum_{\mathrm{j}} \varpi_{\mathrm{j}} \mathrm{exp}(-\mathrm{Ej}/k\mathrm{T}_n)} \\
&\times \sum_{i=0}^{m-1} \sum_{\mathrm{j}=i=1}^{m} \varpi_{\mathrm{j}} (\mathrm{E}_{\mathrm{j}} - \mathrm{E}_i) \mathrm{exp}(-\mathrm{E}_i/k\mathrm{T}_n) \\
&\times \left\{ \mathrm{exp}\left[\frac{\mathrm{E}_{\mathrm{j}} - \mathrm{E}i}{k\mathrm{T}_e\mathrm{T}_n} (\mathrm{T}_e - \mathrm{T}_n) \right] - 1 \right\} \\
&\times \int_{\mathrm{E}_{\mathrm{j}} - \mathrm{E}_i}^{\infty} \mathrm{E}'(i \rightarrow \mathrm{j}, \mathrm{E}') \mathrm{exp}\left(-\frac{\mathrm{E}'}{k\mathrm{T}_e} \right) d\mathrm{E}'
\end{aligned} \tag{B.8}$$

where ϖ_{j} is the statistical weight of the jth state needed to calculated the partition function:

$$\sum_{\mathrm{j}} \varpi_{\mathrm{j}} \mathrm{exp}(-\mathrm{E}_{\mathrm{j}}/k\mathrm{T}_n) \tag{B.9}$$

where $\mathrm{E_j}$ and E_u are the energies in the ith and j th states such that $\mathrm{E_j}-\mathrm{E}_i > 0$. The above equation (B.8) can be applied for both excitation and de-excitation of an electron and a particle depending on the initial energies involved.

In the case of excitation, for low energy electrons, rotational excitation is entirely due to long-range interactions. The leading term in the long-range interaction potential is due to coupling between the electron and molecular charge distribution:

$$V(r) = -qe/r^3 \tag{B.10}$$

where the quadrupole moment is:

$$q = q_0 e a_0^2 \tag{B.11}$$

with q_0 being experimentally determined and a_0 is the Bohr radius.

Using the Born approximation, the rotational excitation cross-sections for the electron interaction can be calculated. The angular dependence of quadra-pole interaction potential leads to the selection rule $\acute{\mathrm{J}} = \mathrm{J} \pm 2$ for transitions between rotational levels. The cross section for these transitions is given by:

$$\begin{aligned}\sigma_{\mathrm{rot}}(\mathrm{J}\pm 2;\mathrm{J}) &= \frac{\acute{K}}{15K}\pi a_0^2 \\ &\times \left[8q_0^2 + \frac{\pi q_0(\alpha_\parallel - \alpha_\perp)}{3}\left(\frac{3K^2+\acute{K}^2}{K}\right) + \frac{\pi^2(\alpha_\parallel-\alpha_\perp)^2}{32}(K^2+\acute{K}^2)\right] \\ &\times \frac{(\mathrm{J}+1\pm 1)(\mathrm{J}\pm 1)}{(2\mathrm{J}+1)(2\mathrm{J}+1\pm 1)}\end{aligned} \tag{B.12}$$

with

$$q_0 = q/ea_0^2, \quad K = (2\mathrm{M_R E})^{1/2}/\acute{h} \tag{B.13}$$

where K and $\acute{K}$ are the initial and final wave numbers of the scattered electrons, πa_0^2 is the atomic cross-section and $\alpha_\parallel$ and $\alpha_\perp$ are the longitudinal and transverse polarizabilities of the molecules involved.

From these derivations and equations the rate of energy loss of electrons through excitation and de-excitation has been summarized by Henry and McElroy [1969] and can be calculated by the following equation:

$$\begin{aligned} \mathrm{L_{rot}}(e,n) &= N_e \upsilon \sum_{\mathrm{j}} n_{\mathrm{j}} [\sigma(\mathrm{J} \rightarrow \mathrm{J}+2)(\mathrm{E_{J+2}} - \mathrm{E_J}) \\ &- \sigma(\mathrm{J} \rightarrow \mathrm{J}-2)(\mathrm{E_J} - \mathrm{E_{J-2}})] \end{aligned} \tag{B.14}$$

where υ is the electron velocity, n_{j} is the concentration of molecules in the J th rotational level and $\mathrm{E_J}$ the rotational energy of the J th level,

$$\mathrm{E_J} = \mathrm{BJ(J+1)} \tag{B.15}$$

and the rotational constant is:

$$\mathrm{B} = h^2/8\pi^2\mathrm{I} \tag{B.16}$$

where I is the moment of inertia of the molecule about the axis through the centre of mass and orthogonal to the internuclear axis.

This derivation can be taken further and constrained toward real values by making assumptions about the neutral particles being collided with. By assuming a neutral gas has a Maxwellian distribution (as is the case in the unexcited ionosphere), its rotational population for a given temperature T_n can be given by:

$$n_n(\mathrm{J}) = n_n \frac{(2\mathrm{J}+1)\exp(-\mathrm{E_J}/k\mathrm{T}_n)}{\sum_{\mathrm{j}}(2\mathrm{J}+1)\exp(-\mathrm{E_J}/k\mathrm{T}_n)} \tag{B.17}$$

With this addition the initial energy loss equation becomes:

$$\begin{aligned} \mathrm{L_{rot}}(e,n) &= \left(\frac{2E}{m_e}\right)^{1/2} n_e n_n \sum_{\mathrm{j}} \frac{(2\mathrm{J}+1)\exp(-\mathrm{E_J}/k\mathrm{T}_n)}{\sum_{\mathrm{J}}(2\mathrm{J}+1)\exp(-\mathrm{E_J}/k\mathrm{T}_n)} \\ &\times [\sigma(\mathrm{J}+2;\mathrm{J})(\mathrm{E_{J+2}} - \mathrm{E_J}) - \sigma(\mathrm{J}-2;\mathrm{J})(\mathrm{E_J} - \mathrm{E_{J-2}})] \end{aligned} \tag{B.18}$$

where E is the electron energy and n_n the neutral molecular gas density.

Another refinement of this equation can be made if it is also assumed that the electron gas also has a Maxwellian temperature distribution at T_e (which again is true under unperturbed ionospheric conditions). In this case the average loss rate can be refined to:

$$\begin{aligned} \mathrm{L_{rot}}(e,n) &= 2\pi\left(\frac{1}{\pi k \mathrm{T}_e}\right)^{3/2}\left(\frac{2}{m_e}\right)^{1/2}\frac{n_e n_n}{\sum_{\mathrm{j}}(2\mathrm{J}+1)\exp(-\mathrm{E_J}/k\mathrm{T}_n)} \\ &\times \int_0^\infty \mathrm{E}\exp\left(-\frac{\mathrm{E}}{k\mathrm{T}_e}\right)\sum_{\mathrm{J}}(2\mathrm{J}+1)\exp\left(-\frac{\mathrm{E_J}}{k\mathrm{T}_n}\right) \\ &\times [\sigma(\mathrm{J}+2,\mathrm{J})(\mathrm{E_{J+2}}-\mathrm{E_J})\sigma(\mathrm{J}-2;\mathrm{J})(\mathrm{E_J}-\mathrm{E_{J-2}})]d\mathrm{E} \end{aligned} \tag{B.19}$$

If only a small range of T_e and T_n are evaluated or possible, such as present in thermosphere, this equation can be further simplified and approximated in terms of the temperature difference ($\mathrm{T}_e - \mathrm{T}_n$) to become:

$$\mathrm{L_{rot}}(e,n) = n(e)n(n)(G\bar{\nu}_{\mathrm{rot}}k(\mathrm{T}_e - \mathrm{T}_n)) \tag{B.20}$$

Using this simplified equation, on the above stated assumption, known rotational cross-sections such as those from laboratory experiments [Lummerzheim and Lilensten, 1994] of molecules can now been entered and the energy loss rates for each species can be determined. However, rotational cross section data from some collisions, such as slow electrons with O_2 molecules, are not as well established as others, even through laboratory methods.

Collision loss measurements are further complicated as not all inelastic collisions lose energy through kinetic energy transfer as described above. Energy transfer can produce excitation of particles and cause the excited particle to vibrate. This energy transfer due to vibration is highly dependent on the cross-sections and resonance frequencies, which were calculated by Prasad and Furman [1973] and summarized in Rees and Lummerzheim [1989], such that:

$$\mathrm{E}_{n\upsilon} = \mathrm{E}_n + (\upsilon + 1/2)h\nu_{\mathrm{vib}} \tag{B.21}$$

where E_n is the energy of the electronic state of the molecular ion and υ is the vibrational quantum number. The vibrational energy is $\mathrm{h}\nu_{vib}$.

This equation is analogous to the equation for rotational kinetic energy loss, but does not include de-excitation collisions. Vibrational levels can only be excited through collision, and energy cannot be lost this way. However, as $\mathrm{T}_e > \mathrm{T}_n$ it is the current view that this process will occur most often, if at all, in the atmosphere. Therefore, collisions of electrons with neutrals causes cooling and not vice versa. Applied to the rotational kinetic energy temperatures above, by assuming electrons and neutrals have a Maxwellian energy distribution at temperatures T_e and T_n, a simplified loss rate expression can be calculated with an analytic expression [Rees and Lummerzheim, 1989].

One of the most important particles for electron energy loss in the upper atmosphere is atomic oxygen, particularly in its ground state $O(^3P_{2,1,0})$. This particle is particularly dominant in low energy regimes where inelastic collisions become less frequent. This reaction for $O(^3P_{2,1,0})$ is:

$$e + O(^3P_J) \rightarrow e + O(^3P_{J'}) \tag{B.22}$$

where the cross section for the transition from level J to J' is:

$$\sigma(J \rightarrow J'; E) = \frac{\pi a_0^2}{\tilde{\omega}_J} \Omega(J, J') \frac{13.604}{E} \tag{B.23}$$

where πa_0^2 is the area of the first Bohr orbit, $\tilde{\omega}$ is the statistical weight (2J+1), the energy of 1 Rydberg is 13.604 eV, E is in eV and $\Omega(J, J')$ is the collision strength for the transition ^3P_J to $^3P_{J'}$.

If the electron gas is assumed to have a Maxwellian distribution at temperature T_e the energy loss rate becomes:

$$\begin{aligned} L_{FS}(e, O) &= 2\pi \left(\frac{1}{\pi k T_e}\right)^{3/2} \left(\frac{2}{m_e}\right)^{1/2} n_e n_J(O) \int_0^\infty E \exp\left(-\frac{E}{k T_e}\right) \\ &\times \sum_{J' \neq J} (E_J - E_{J'}) \sigma(J \rightarrow J'; E) dE \end{aligned} \tag{B.24}$$

B.2 Electron Energy Loss with Ions

Another process by which electrons exchange energy is through collision with ion species. Under most conditions T_e is greater than T_n, and so collisions will produce a net loss in electron energy, as described in Schunk and Nagy [2000]. However, when this is not the case it may cause an increase in electron energy and a decrease in ion energy.

Using the generalized formula for the collision cross-section of an electron and ion, the energy transfer (loss) rates between the two particles can now be calculated as above, described in detail by Bates [2002], such that:

$$L_{elastic}(e, i) = \frac{4(2\pi m_e)^{1/2}}{m_i} n_e n_i e^4 \frac{\ln\Lambda}{(k T_e)^{3/2}} K(T_e - T_i) \tag{B.25}$$

B.3 Ion and Neutral Energy Exchange

As ion species in the ionosphere are on average at a higher temperature than neutral species, collisions between these two will also result in a net loss of energy for ions, as first explained by Banks [1966].

There are two main energy exchange mechanisms between ion and neutral species, these are summarized in Rees and Lummerzheim [1989]. The first is produced by non-resonant electric collisions between species. This process is dominant at low temperatures and usually induces a dipole or polarizing interaction. By solving polarizability of species analytically a solution for this energy transfer can be calculated independently of temperature.

The second process that can occur is that of symmetrical resonant charge transfer. This process involves collisions between ions and their parent neutral species., for example:

$$O^+ + O \rightarrow O + O^+ \tag{B.26}$$

$$\text{or } N_2^+ + N_2 \rightarrow N_2 + N_2^+ \tag{B.27}$$

In these cases although a charge transfer occurs in the collisions, each particle usually retains its original kinetic energy. Therefore, as in the process the ion becomes a neutral and the cross-section for this reaction is large, this process effectively transfers kinetic energy from ions to neutrals with little or no energy loss. The collision cross sections have been calculated by Rees and Lummerzheim [1989] and others in subsequent literature through both observations and laboratory experiments.

By assuming that the transfer from the collisions is elastic, as well as having Maxwellian velocity distributions, an effective momentum transfer cross-section can be defined by averaging the differential cross-sections of the ion and neutral species.

The loss rates can be calculated from this average cross-section such that:

$$L_{SCT}(i,n) = -\frac{3}{2} \cdot 10^{-7} n_i \nu_{SCT} k(T_i - T_n) \quad (\text{J cm}^{-3}\text{s}^{-1}) \tag{B.28}$$

where ν_{SCT} is the average collision frequency for the charge exchange.

At low temperatures (T_i+T_n <300 K) the non-resonant electric collision process is dominant, but reduces with increasing temperature. The charge exchange process increases with temperature and becomes dominant over the non-resonant electric collision process at high temperatures (T_i+T_n >2000 K).

B.4 Neutral Gas Energy Loss

As $T_n < T_i$ and T_e, all collisions with other (charged) particles should cause a net increase in energy. However, energy can be lost from neutral species via radiation. Excited neutral gases can drop back down into ground state energy levels through the release of electromagnetic radiation, which if not reabsorbed produces a loss in the neutral species energy. Produced emissions usually have long natural lifetimes, but can be prompted by collisions with other neutral particles and species. Alternatively, collisions can cause a long lifetime emitting neutral to transfer energy or react to give energy to a shorter lifetime emitting particle. This phenomenon is widely observed in the atmosphere and is commonly know as airglow. One such example of an airglow-producing reaction could be when there is a collision between an excited N particle and an O_2 molecule, described in Meinel [2002] as:

$$N(^4S,^2D,^2P) + O_2 \rightarrow NO(\upsilon > 0) + O \tag{B.29}$$

References

S-I. Akasofu. The Development of the Auroral Substorm. Planetary Space Science, 12:273, April 1964.

S-I. Akasofu. The relationship between the magnetosphere and magnetospheric / auroral substorms. Annales Geophysicae, 31(3):387–394, 2013.

S-I. Akasofu, A.T.Y. Lui, and C-I. Meng. Importance of auroral features in the search for substorm onset processes. Journal of Geophysical Research, 115(A8):A08218, 2010.

T. Andersen. The servo system of the eiscat svalbard antenna. In Proc. SPIE, volume 2479, pages 301–312, 1995.

W.I. Axford. Magnetic field reconnection. Geophysical Monograph Series, 30:1–8, 1984.

P.M. Banks. Collision frequencies and energy transfer ions. Planetary and Space Science, 14 (11):1105–1122, 1966.

P.M. Banks and G. Kockarts. Aeronomy. A, Academic, San Diego, California, 1, 1973.

R.H. Barker. Group synchronizing of binary digital systems. Communication theory, pages 273–287, 1953.

J. Bartels and G. Fanselau. Der erdmagnetische Sturm vom 16. April 1938. Naturwissenschaften, 26(19):296–298, 1938.

D.R. Bates. The temperature of the upper atmosphere. Proceedings of the Physical Society. Section B, 64(9):805, 2002.

E.M. Blixt, T. Grydeland, N. Ivchenko, T. Hagfors, C. La Hoz, B.S. Lanchester, U.P. Lovhaug, and T.S. Trondsen. Dynamic rayed aurora and enhanced ion-acoustic radar echoes. Annales Geophysicae, 23(1):3–11, 2005. 11th Biannual EISCAT International Workshop, Menlo Pk, CA, AUG, 2003.

M.H. Boehm, C.W. Carlson, J.P. McFadden, J.H. Clemmons, and F.S. Mozer. High-Resolution Sounding Rocket Observations of Large-Amplitude Alfven Waves. Journal of Geophysical Research - Space Physics, 95(A8):12157–12171, August 1990. doi: {10.1029/JA095iA08p12157}.

S. Cabrit. Models of molecular outflows. Astrophysics and Space Science, 233(1-2):81–96, November 1995.

S. Chakrabarti, D. Pallamraju, J. Baumgardner, and J. Vaillancourt. HiTIES: A high throughput imaging echelle spectrogragh for ground-based visible airglow and auroral studies. Journal of Geophysical Research-Space Physics, 106(A12):30337–30348, December 2001.

S Chapman and T.G Cowling. The mathematical theory of non-uniform gases. Cambridge Univ. Press, London, 1952.

A.C-L. Chian, S.R. Lopes, and M.V. Alves. Nonlinear excitation of Langmuir and Alfven waves by auroral whistler waves in the planetary magnetosphere. Astronomy and Astrophysics, 288:981–984, August 1994.

P.N. Collis, I. Haggstrom, K. Kaila, and M.T. Rietveld. EISCAT Radar Observations of Enhanced Incoherent-Scatter Spectra - Their Relation to Red Aurora and Field-Aligned Currents. Geophysical Research Letters, 18(6):1031–1034, June 1991. doi: {10.1029/91GL00848}.

H. Dahlgren, N. Ivchenko, J. Sullivan, B.S. Lanchester, G. Marklund, and D. Whiter. Morphology and dynamics of aurora at fine scale: first results from the ASK instrument. Annales Geophysicae, 26(5):1041–1048, 2008. 32nd Annual European Meeting on Atmospheric Studies by Optical Methods, Kiruna, SWEDEN, AUG 28-SEP 01, 2006.

H. Dahlgren, J.L. Semeter, K. Hosokawa, M.J. Nicolls, T.W. Butler, M.G. Johnsen, K. Shiokawa, and C. Heinselman. Direct three-dimensional imaging of polar ionospheric structures with the Resolute Bay Incoherent Scatter Radar. Geophysical Research Letters, 39, March 2012. doi: {10.1029/2012GL050895}.

V. Domingo, B. Fleck, and A.I. Poland. Soho: the solar and heliospheric observatory. Space Science Reviews, 72(1-2):81–84, 1995.

E. Donovan, J., L. Cogger, and T. Trondsen. Norstar: An array of digital all-sky imagers in the canadian north. 1998.

C. Doppler. Uber das farbige licht der doppelsterne und einiger anderer gestirne des himmels. Abhandlungen der Knigliche Bhmischen Gesellschaft der Wissenschaften, Series V(Vol. II), 1906.

E.M. Dubinin, A.S. Volokitin, P.L. Israelevich, and N.S. Nikolaeva. Auroral Electromagnetic Disturbances at Altitudes of 900 km - Aflven-Wave Turbulence. Planetary and Space Science, 36(10):949–962, October 1988. doi: {10.1016/0032-0633(88)90033-5}.

J. Ekeberg, G. Wannberg, L. Eliasson, and K. Stasiewicz. Ion-acoustic solitary waves and spectrally uniform scattering cross section enhancements. Annales Geophysicae, 28(6):1299–1306, 2010. doi: {10.5194/angeo-28-1299-2010}.

D.T. Farley. A theory of incoherent scattering of radio waves by a plasma 4. the effect of unequal ion and electron temperatures. Journal of Geophysical Research, 71(17):4191–4098, 1966.

F.R.E. Forme. A new interpretation on the origin of enhanced ion acoustic fluctuations in the upper ionosphere. Geophysical Research Letters, 20(21):2347–2350, 1993.

F.R.E. Forme. Parametric decay of beam-driven Langmuir wave and enhanced ion-acoustic fluctuations in the ionosphere: a weak turbulence approach. Annales Geophysicae - Atmospheres Hydrospheres and Space Sciences, 17(9):1172–1181, September 1999.

F.R.E. Forme, D. Fontaine, and J.E. Wahlund. 2 Different Types of Enhanced Ion-Acoustic Fluctuations Observed in the Upper Ionosphere. Journal of Geophysical Research-Space Physics, 100(A8):14625–14636, August 1995. doi: {10.1029/94JA01093}.

J.C. Foster and J. Aarons. Enhanced anti-sunward convection and F-region scintillations at mid-latitudes during storm onset. Journal of Geophysical Research-Space Physics, 93(A10): 11537–11542, October 1988.

M.L. Goldstein, W.H. Matthaeus, and J.J. Ambrosiano. Acceleration of charged particles in magnetic reconnection: Solar flares, the magnetosphere, and solar wind. Geophysical Research Letters, 13(3):205–208, 1986.

W.E. Gordon. Incoherent scattering of radio waves by free electrons with applications to space exploration by radar. Proceedings of the IRE, 46(11):1824–1829, 1958.

R.A. Greenwald, K.B. Baker, J.R. Dudeney, M. Pinnock, T.B. Jones, E.C. Thomas, J.-P. Villain, J.-C. Cerisier, C. Senior, C. Hanuise, et al. Darn/superdarn. Space Science Reviews, 71(1-4): 761–796, 1995.

K.M. Groves. Nonlinear Ionospheric Propagation Effects on UHF and VLF Radio Signals. PhD thesis, Massachusetts Inst of Tech - Cambridge Plasma Fusion Center, 1991.

J.L. Grydeland, T .and Chau, C. La Hoz, and A. Brekke. An imaging interferometry capability for the EISCAT Svalbard Radar. Annales Geophysicae, 23(1):221–230, 2005. 11th Biannual EISCAT International Workshop, Menlo Pk, CA, AUG, 2003.

T. Grydeland and C. La Hoz. Phase calibration of a radar interferometer by means of incoherent scattering. Radio Science, 45, July 2010. doi: {10.1029/2009RS004249}.

T. Grydeland, C. La Hoz, T. Hagfors, E.M. Blixt, S. Saito, A. Strømme, and A. Brekke. Interferometric observations of filamentary structures associated with plasma instability in the auroral ionosphere. Geophysical Research Letters, 30(6):1338, 2003.

T. Grydeland, E.M. Blixt, U.P. Lovhaug, T. Hagfors, C. La Hoz, and T.S. Trondsen. Interferometric radar observations of filamented structures due to plasma instabilities and their relation to dynamic auroral rays. Annales Geophysicae, 22(4):1115–1132, 2004.

P. Guio and F. Forme. Zakharov simulations of Langmuir turbulence: Effects on the ion-acoustic waves in incoherent scattering. Physics of Plasmas, 13(12), December 2006. doi: {10.1063/1.2402145}.

P. Guio, J. Lilensten, W. Kofman, and N. Bjørnå. Electron velocity distribution function in a plasma with temperature gradient and in the presence of suprathermal electrons: application to incoherent-scatter plasma lines. Annales Geophysicae, 16(10):1226–1240, 1998.

B. Gustavsson and T. Grydeland. Orthogonal-polarization alternating codes. Radio Science, 44 (6):RS6005, 2009.

A. Hasegawa. Particle Acceleration by MHD Surface-Wave and Formation of Aurora. Journal of Geophysical Research-Space Physics, 81(28):5083–5090, 1976. doi: {10.1029/JA081i028p05083}.

A.E. Hedin. Extension of the MSIS Thermosphere Model into the Middle and Lower Atmosphere. Journal of Geophysical Research, 96:1159, 1991.

R.J.W. Henry and M.B. McElroy. The absorption of extreme ultraviolet solar radiation by Jupiter's upper atmosphere (Absorption of EUV sunlight by Jupiter upper atmosphere, discussing photoelectron energy loss, thermal equilibrium and heating efficiencies). Journal of the Atmospheric Sciences, 26:912–917, 1969.

Y. Itikawa. Transport coefficients of plasmas: applications of the unified theory. Journal of the Physical Society of Japan, 18(10):1499–1507, 1963.

Y. Itikawa. Effective Collision Frequency of Electrons in Atmospheric Gases. Planetary and Space Science, 19(8):993–&, 1971. doi: {10.1016/0032-0633(71)90149-8}.

J.R. Kan, W. Baumjohann, F.V. Coroniti, J. Birn, V.M. Vasyliunas, C.F. Kennel, A.T.Y. Lui, L.R. Lyons, Y. Kamide, and D.N. Baker. Substorm research moves toward a unifying framework. Eos, Transactions American Geophysical Union, 79(28):329–331, 1998.

A Kero, C.-F Enell, Th Ulich, E Turunen, M T Rietveld, and F. H. Honary. Statistical signature of active D-region HF heating in IRIS riometer data from 1994-2004. Annales Geophysicae, 25(2):407–415, 2007.

J.M. Kindel and C.F. Kennel. Topside current instabilities. Journal of Geophysical Research, 76 (13):3055–3078, 1971.

M. Kunitake and K. Schlegel. Neutral Winds in the Lower Thermosphere at High Latitudes from 5 years of EISCAT Data. Annales Geophysicae, 9(2):143–155, February 1991.

S.P. Kuo and M.C. Lee. Cascade spectrum of HF enhanced plasma lines generated in HF heating experiments. Journal of Geophysical Research-Space Physics, 110(A1), January 2005. doi: {10.1029/2004JA010674}.

B.S. Lanchester and B.J. Gustavsson. Imaging of aurora to estimate the energy and flux of electron precipitation. Geophysical Monograph Series, 197:171–182, 2012.

M.S. Lehtinen and H. Asko. General incoherent scatter analysis and GUISDAP. Journal of Atmospheric and Terrestrial Physics, 58(1-4):435 – 452, 1996. doi: {DOI:10.1016/0021-9169(95)00047-X}. Selected papers from the sixth international Eiscat Workshop.

M.S. Lehtinen, A. Huuskonen, and M. Markkanen. Randomization of alternating codes: Improving incoherent scatter measurements by reducing correlations of gated autocorrelation function estimates. Radio Science, 32:2271, 1997. doi: 10.1029/97RS02556.

D. Lummerzheim and J. Lilensten. Electron transport and energy degradation in the ionosphere: Evaluation of the numerical solution, comparison with laboratory experiments and auroral observations. Annales Geophysicae, 12(10):1039–1051, 1994.

L. Mankiewicz. Gloria-the global robotic telescopes intelligent array for e-science. EAS Publications Series, 61:483–486, 2013.

N.C. Maynard, D.S. Evans, and J. Troim. Electric field observations of time constants related to charging and charge neutralization processes in the ionosphere. In Artificial particle beams in space plasma studies, volume 1, pages 627–644, 1982.

A.B. Meinel. The spectrum of the airglow and the aurora. Reports on Progress in Physics, 14 (1):121, 2002.

NASA. Comprehensive solar wind laboratory for long-term solar wind measurements, 1994. URL http://wind.nasa.gov/.

M.J. Nicolls, N. Aponte, S.A. Gonzalez, M.P. Sulzer, and W.L. Oliver. Daytime F region ion energy balance at Arecibo for moderate to high solar flux conditions. Journal of Geophysical Research-Space Physics, 111(A10), October 2006. doi: {10.1029/2006JA011664}.

E. Nielsen and K. Schlegel. Coherent radar doppler measurements and their relationship to the ionospheric electron drift velocity. Journal of Geophysical Research: Space Physics (1978–2012), 90(A4):3498–3504, 1985.

Y. Ogawa, S.C. Buchert, I. Häggström, M.T. Rietveld, R. Fujii, S. Nozawa, and H. Miyaoka. On the statistical relation between ion upflow and naturally enhanced ion-acoustic lines observed with the eiscat svalbard radar. Journal of Geophysical Research, 116(A3):A03313, 2011.

Y. Ogawa, S.C. Buchert, R. Fujii, S. Nozawa, and F. Forrne. Naturally enhanced ion-acoustic lines at high altitudes. Annales Geophysicae, 24(12):3351–3364, 2006.

K. Papadopoulos. A review of anomalous resistivity for the ionosphere. Reviews of Geophysics and Space Physics, 15:113–127, 1977.

S.S. Prasad and D.R. Furman. Electron cooling by molecular oxygen. Journal of Geophysical Research, 78(28):6701–6707, 1973.

K. Rawer and D. Bilitza. International reference ionosphere Plasma densities: Status 1988. Advances in Space Research, 10(8):5–14, 1990.

M.H. Rees. Auroral ionization and excitation by incident energetic electrons. Planetary and Space Science, 11(10):1209–1218, 1963.

M.H. Rees and D. Lummerzheim. Characteristics of Auroral Electron-Precipitation Derived from Optical Spectroscopy. Journal of Geophysical Research-Space Physics, 94(A6):6799–6815, June 1989.

M.T. Rietveld, P.N. Collis, and J.P. Stmaurice. Naturally Enhanced ion-acoustic-waves in the auroral ionosphere observed with the EISCAT 933-MHz Radar. Journal of Geophysical Research-Space Physics, 96(A11):19291–19305, November 1991.

N.M. Schlatter, T. Grydeland, N. Ivchenko, V. Belyey, J. Sullivan, C. La Hoz, and M. Blixt. Radar interferometer calibration of the EISCAT Svalbard Radar and an additional receiver station. Journal of Atmospheric and Solar-Terrestrial Physics, 2012.

R.W. Schunk and A.F. Nagy. Ionospheres atmospheric and space science series. Cambridge: Cambridge University Press, 2000.

R.W. Schunk, W.J. Raitt, and A.F. Nagy. Effect of diffusion-thermal processes on the high-latitude topside ionosphere. Planetary and Space Science, 26(2):189–191, 1978.

F. Sedgemore-Schulthess and J.P. St-Maurice. Naturally enhanced ion-acoustic spectra and their interpretation. Surveys in Geophysics, 22(1):55–92, 2001. doi: {10.1023/A:1010691026863}.

K.J.F Sedgemore-Schulthess, M. Lockwood, T.S. Trondsen, B.S. Lanchester, M.H Rees, D.A. Lorentzen, and J. Moen. Coherent EISCAT Svalbard Radar spectra from the dayside cusp/cleft and their implications for transient field-aligned currents. Journal of Geophysical Research-Space Physics, 104(A11):24613–24624, November 1999. doi: {10.1029/1999JA900276}.

J.J. Sparks, D. Janches, M.J. Nicolls, and C. Heinselman. Determination of physical and radiant meteor properties using PFISR interferometry measurements of head echoes. Journal of Atmospheric and Solar-Terrestrial Physics, 72(16):1221–1230, October 2010. doi: {10.1016/j.jastp.2010.08.004}.

E.C. Stone, A.M. Frandsen, R.A. Mewaldt, E.R. Christian, D. Margolies, J.F. Ormes, and F. Snow. The advanced composition explorer. In The Advanced Composition Explorer Mission, pages 1–22. Springer, 1998.

A. Stromme, V. Belyey, T. Grydeland, C. La Hoz, U.P. Lovhaug, and B. Isham. Evidence of naturally occurring wave-wave interactions in the polar ionosphere and its relation to naturally enhanced ion acoustic lines. Geophysical Research Letters, 32(5), March 2005. doi: {10.1029/2004GL020239}.

J.M. Sullivan. Spectral studies of small-scale auroral structure and plasma instability in the high-latitude ionosphere. PhD thesis, University of Southampton, 2008.

J.M. Sullivan, N. Ivchenko, M. Lockwood, T. Grydeland, E.M. Blixt, and B.S. Lanchester. Phase calibration of the EISCAT Svalbard Radar interferometer using optical satellite signatures. Annales Geophysicae, 24(9, Sp. Iss. SI):2419–2427, 2006. 12th Biannual EISCAT International Workshop, Kiruna, SWEDEN, AUG 29-SEP 02, 2005.

M.P. Sulzer. Recent incoherent scatter techniques. Advances in Space Research, 9(5):153–162, 1989.

J.J. Thomson. Electric deflection of rays. Nobel Prize Address, 1906.

A. Viljanen and L. Häkkinen. Image magnetometer network. In Satellite-ground based coordination sourcebook, volume 1198, page 111, 1997.

I.I. Virtanen, J. Vierinen, and M.S. Lehtinen. Phase-coded pulse aperiodic transmitter coding. Annales Geophysical, 27(7):2799–2811, 2009.

I.I. Virtanen, M.S. Lehtinen, T. Nygren, M. Orispaa, and J. Vierinen. Lag profile inversion method for EISCAT data analysis. Annales Geophysicae, 26(3):571–581, 2008.

Y. Voitenko, M. Goossens, O. Sirenko, and A.C-L. Chian. Nonlinear excitation of kinetic Alfvén waves and whistler waves by electron beam-driven Langmuir waves in the solar corona. A&A, 409(1):331–345, 2003. doi: 10.1051/0004-6361:20031104.

J.E. Wahlund, H.J. Opgenoorth, I. Haggstrom, K.J. Winser, and G.O.L Jones. Eiscat observations of topside ionospheric ion outflows during auroral activity- revisited. Journal of Geophysical Research, 97:3019–3037, 1992.

J.E. Wahlund, F.R.E. Forme, H.J. Opegnoorth, M.A.L. Persson, E.V. Mishin, and A.S. Volokitin. Scattering if Electromagnetic-Waves from a Plasma - Enhanced Ion-Acoustic Fluctuations Due to Ion-Ion 2-Stream Instabilities. Geophysical Research Letters, 19(19):1919–1922, October 1992. doi: {10.1029/92GL02101}.

J.E. Wahlund, H.J. Opgenoorth, F.R.E. Forme, M.A.L. Persson, I. Haggstrom, and J. Lilensten. Electron Energization in the Topside Auroral Ionosphere - on the Importance of Ion-Acoustic Turbulence. Journal of Atmospheric and Terrestrial Physics, 55(4-5):623–645, April 1993. doi: {10.1016/0021-9169(93)90010-V}.

J.E. Wahlund, P. Louran, T. Chust, H. Deferaudy, A. Roux, B. Holback, B. Cabrit, A.I. Eriksson, P.M. Kintner, M.C. Kelly, J. Bonnell, and S. Chesney. Observations of ion-acoustic fluctuations in the auroral topside ionosphere by the FREJA S/C. Geophysical Research Letters, 21 (17):1835–1838, August 1994a. doi: {10.1029/94GL01290}.

J.E. Wahlund, P. Louran, T. Chust, H. Deferaudy, A. Roux, B. Holback, P.O. Dovner, and G. Holmgren. On ion-acoustic turbulance and the nonlinear evolution of kinetic alfven waves in aurora. Geophysical Research Letters, 21(17):1831–1834, August 1994b. doi: {10.1029/94GL01289}.

D. Whiter and N. Partamies. Long-term optical studies of the aurora using the miracle cameras.

J.D. Winningham, F Yasuhara, S.-I. Akasofu, and W.K Heikkila. The latitudinal morphology of 10-eV to 10-keV electron fluxes during magnetically quiet and disturbed times in the 2100-0300 MTL sector. Journal of Geophysical Research, 80(22):3148–3171, 1975.

R.F. Woodman. Inclination of the geomagnetic field measured by an incoherent scatter technique. Journal of Geophysical Research, 76(1):178–184, 1971.

D.J. Wu, J. Huang, J.F. Tang, and Y.H. Yan. Solar Microwave Drifting Spikes and Solitary Kinetic Alfvén Waves. The Astrophysical Journal Letters, 665(2):L171, 2008.

C.J. Zamlutti. Atmospheric wave observations at arecibo. Solar-Terrestrial Physics, 3:417–439, 1974.